TRANSPORT PROPERTIES AND REACTION RATES OF HYDROGEN AND DEUTERIUM IONS IN HYDROGEN AND DEUTERIUM GASES

A THESIS

Presented to

The Faculty of the Division of Graduate

Studies and Research

by

Edward Graham IV

In Partial Fulfillment

of the Requirements for the Degree

Doctor of Philosophy

in the School of Physics

Georgia Institute of Technology

March, 1974

TRANSPORT PROPERTIES AND REACTION RATES

OF

HYDROGEN AND DEUTERIUM IONS

IN

HYDROGEN AND DEUTERIUM GASES

Approved:

Earl W. McDaniel, Chairman

R. F. Borkman

R. Fox

Date approved by Chairman March 15, 1974

This thesis is dedicated
to my parents, my wife Dee,
and my daughter Debbie.

ACKNOWLEDGMENTS

It is with pleasure that acknowledgment is made of the interest and assistance of those who have contributed to the work described in this thesis. The author wishes to acknowledge the guidance, encouragement, and teaching of his thesis advisor, Dr. Earl McDaniel, throughout this research. The help, comments, and instruction of Dr. Ian Gatland, who made many helpful suggestions through this research, were appreciated. The comments of Dr. Ron Fox and Dr. Ray Borkman, who served on the thesis reading committee, were valued.

The assistance of Mr. Randy James, who aided the author in obtaining the data presented here and with whom many fruitful discussions were held, is greatly appreciated. The contributions of those who preceded the author in this laboratory, Dr. Dan Albritton, Dr. Tom Miller, Dr. John Moseley, Dr. Bob Snuggs, and Dr. John Schummers, are acknowledged.

A special acknowledgment is made of the contribution of Dr. Ian Gatland to the analysis presented in Chapter III.

The research reported here was sponsored by the Office of Naval Research. The author was the recipient of a NDEA Fellowship for three years.

TABLE OF CONTENTS

TABLE OF CONTENTS (Concluded)

LIST OF TABLES

LIST OF TABLES (Continued)

LIST OF ILLUSTRATIONS

LIST OF ILLUSTRATIONS (Continued)

SUMMARY

The drift velocities, mobilities, and longitudinal diffusion coefficients of H^+, H_3^+, and H^- ions in H_2 gas and D^+, D_3^+, and D^- ions in D_2 gas have been measured as a function of E/N, where E is the electric field intensity and N is the gas number density. These measurements were made at a gas temperature of 300°K and at various pressures between 100 and 750 microns. The rates of the ion molecule reactions

$$H^+ + 2H_2 \rightarrow H_3^+ + H_2$$

and

$$D^+ + 2D_2 \rightarrow D_3^+ + D_2$$

have been measured at pressures between 300 and 500 microns and over an intermediate range of E/N.

The measurements were made using a drift tube mass spectrometer of ultra-high vacuum construction. The measurements were made by a time-of-flight method, using a pulsed electron-impact ion source combined with an electric shutter to create, repetitively, bursts of ions of accurately known initial spatial extent and temporal duration. Potassium ions can be produced by a thermionic emitter. The ion swarm migrates down the drift tube under the influence of a weak uniform electric field. During this migration the swarm spreads due to diffusion, and may undergo ion-molecule reactions with the neutral gas. The ion population is sampled on the axis at the end of the drift tube by a small exit aperture and

mass-selected by an rf quadrupole spectrometer. The ions are individually detected. The time of arrival of an ion at the detector is recorded by a 256-channel time analyzer. By repetitive pulsing of the ion source, a histogram of arrival times can be built up. From such time profiles, the drift velocities, longitudinal diffusion coefficients, and ion-molecule reaction rates were obtained.

Transport equations describing the drift, diffusion, and reaction of two ion swarms were solved and these solutions used in the quantitative studies made. The drift velocity values were obtained basically from the mean arrival times of the profiles. The longitudinal diffusion coefficients were determined from the shape (basically the width) of the profiles. The reaction rate coefficients were obtained from the detailed shape of the reaction-influenced profiles.

The mobility and longitudinal diffusion coefficients of H^+ in H_2 were measured over an E/N range from 4 to 100 Td. The zero-field reduced mobility was determined to be 16.0 $cm^2/V \cdot sec$ from values measured at an E/N below 10 Td. The measured ND_L agreed with the Einstein value in the low-field region and showed good agreement with the Whealton-Mason relation over the entire range of E/N.

The mobility and longitudinal diffusion coefficients of H_3^+ in H_2 were measured over an E/N range from 4.5 to 85 Td. The zero-field reduced mobility was determined to be 11.3 $cm^2/V \cdot sec$ from values measured at an E/N below 25 Td. The measured ND_L showed excellent agreement with the Einstein value in the low-field region. The measured ND_L showed fair agreement with the Whealton-Mason relation. The difference between the

measured values of ND_L and those predicted by the Whealton-Mason relation is attributed to proton exchange between H_3^+ and H_2.

The mobility and longitudinal diffusion coefficients of H^- in H_2 were measured over an E/N range from 2.5 to 70 Td. The zero-field reduced mobility was determined to be 43.0 $cm^2/V \cdot sec$ from values measured below an E/N at 15 Td. The measured values of ND_L showed poor agreement with theory except for those values between an E/N of 10 and 30 Td. This poor agreement is attributed to the effects of initial diffusion.

The mobility and longitudinal diffusion coefficients of D^+ in D_2 were measured over an E/N range from 6 to 50 Td. The zero-field reduced mobility was determined to be 11.7 $cm^2/V \cdot sec$ from values measured below an E/N of 20 Td.

The mobility and longitudinal diffusion coefficients of D_3^+ in D_2 were measured over an E/N range from 5 to 50 Td. The zero-field reduced mobility was determined to be 8.07 $cm^2/V \cdot sec$ from values measured below an E/N of 20 Td.

The mobility and longitudinal diffusion coefficients of D^- in D_2 were measured over an E/N range from 7.5 to 15 Td. The zero-field reduced mobility was determined to be 30.1 $cm^2/V \cdot sec$ from values measured below 15 Td.

The rate coefficient for the reaction $H^+ + 2H_2 \rightarrow H_3^+ + H_2$ was measured over an E/N range from 20 to 50 Td. The rate coefficient was found to be constant over this range of E/N and equal to $(3.05 \pm 0.15) \times 10^{-29}$ cm^6/sec. The data clearly indicate that this reaction is three-body. The rate coefficient for the reaction $D^+ + 2D_2 \rightarrow D_3^+ + D_2$ was also measured and found to be the same as for H^+ in H_2.

CHAPTER I

INTRODUCTION

This report deals primarily with the measurement of the transport properties and reaction rates of hydrogen and deuterium ions in hydrogen and deuterium gases. The subject matter of Chapters I, II, and III has, for the most part, been previously reported [1,2]. Chapter I describes the general behavior of ions in a gas under the influence of a uniform electric field. The physical parameters which influence the motion of these ions is described and the goals of the present research are outlined. The drift tube mass spectrometer used in the present research is described in Chapter II. The general apparatus has been previously described in detail, and only the modifications in the apparatus incorporated for the present research and areas not sufficiently covered previously are reported here. In Chapter III the solution of the transport equation describing the drift motion of ions is outlined. The solution of the transport equation has evolved over the past several years. This analysis has been developed by Ian Gatland and the individual evolutionary steps have been reported as they were made. It is attempted here to bring all these individual steps together in a logical manner so that a complete derivation is contained in one place.

Chapters IV, V, and VI contain the experimental results of the present research. These results are described and compared with

existing theory. In Chapter IV the measured mobilities are discussed and, where they exist, are compared with values measured by other experimenters. The mobilities of H^- in H_2 and D^- in D_2 have not been previously measured. In Chapter V the measured longitudinal diffusion coefficients are presented and discussed. These are the first measurements of longitudinal diffusion coefficients reported for the hydrogen ions in hydrogen gas. The curve-fitting procedure used to measure reaction rates is described in Chapter VI.

General Considerations

Ions in a gas subjected to a uniform electric field are accelerated and collide with the gas molecules. The ions gain energy from the electric field between collisions and in general lose energy during collisions. Under appropriate conditions of electric field intensity E and gas number density N the motion of the ions becomes steady state. This happens when the velocity distribution of the ions is independent of time. The motion of the ions in a steady state condition is a function of E and N only through the ratio E/N. The value E/N will be expressed throughout this thesis in units of the Townsend (Td), where 1 Td = 10^{-17} V·cm^2. The average energy the ions have gained from the electric field is called the field energy and is a function of E/N. The total energy of an ion is thus the sum of the thermal and field energies.

We restrict our attention to ions in a gas in steady state motion in a uniform electric field and at ion densities low enough to ignore ion-ion interactions. Also, for the moment, we shall assume

that only a single species of ions is present. Under these conditions the net motion of the ions is along the electric field lines with a characteristic velocity v_d, called the drift velocity. The drift velocity is dependent upon the particular ion-gas combination and the parameter E/N. The mobility K is defined as the ratio of the drift velocity to the electric field intensity

$$K = v_d/E \tag{1-1}$$

and is usually expressed in units of $cm^2/V \cdot sec$. For a constant number density N, K is relatively insensitive to small changes (a few degrees Kelvin) in temperature. The mobility is a measure of the transparency of the gas to a specific ionic species and is inversely proportional to the gas number density. For a fixed number density, K approaches a constant value in the limit of $E \rightarrow 0$ called the zero-field mobility, K(0). To facilitate the comparison of data taken at different number densities the reduced mobility K_o is defined as

$$K_o = K \left(\frac{P}{760} \right) \left(\frac{273.16}{T} \right) \tag{1-2}$$

where P is the pressure in Torr and T is the temperature in °K at which the mobility was measured. This equation normalizes the mobility to that which would be measured at a number density of $2.687 \times 10^{19}\ cm^{-3}$, the number density of an ideal gas at 760 Torr and 0°C. It must be emphasized that equation (1-2) merely provides a normalization with respect to N; the temperature to which K_o actually refers is the

temperature of the gas during the measurement. As E/N is decreased toward zero, K_o approaches a constant value, $K_o(0)$, known as the zero-field reduced mobility. In practice the reduced mobility is constant for values of E/N below about 10 Td. The region over which K_o is constant and equal to $K_o(0)$ is called the low field region and depends upon both the ionic and gas species. In the low field region the thermal energy of the ions is dominant over the field energy and the ion velocity distribution is approximately Maxwellian. However, as the ratio E/N is increased above the low field region, the ionic velocity distribution becomes non-Maxwellian and is in general unknown. The region in which the field energy is dominant over the thermal energy is called the high-field region.

In addition to the net drift along the electric field lines the ions diffuse due to collisions with the gas molecules. In the limit $E/N \rightarrow 0$, the ionic diffusion current density, $\vec{j}$, in a gas is given by Fick's law of diffusion

$$\vec{j} = -D\ \vec{\nabla} n \tag{1-3}$$

where D is the scalar diffusion coefficient and n is the ionic number density. When an electric field is present, $\vec{E}$ defines a unique direction, and the rate of diffusion will in general be different along the electric field and perpendicular to the electric field. The total ionic current density is then given by

$$\vec{j} = \vec{v}_d\ n(\vec{r},t) - \vec{\vec{D}} \cdot \vec{\nabla}_r\ n(\vec{r},t) \tag{1-4}$$

where $n(\vec{r},t)$ is the ion number density and $\overleftrightarrow{D}$ is the diffusion tensor. The first term on the right of equation (1-4) is the current density of the drift motion of the ions and the second term is the current density due to diffusion. If the electric field $\vec{E}$ defines the z-direction, $\overleftrightarrow{D}$ has the form

$$\overleftrightarrow{D} = \begin{pmatrix} D_T & 0 & 0 \\ 0 & D_T & 0 \\ 0 & 0 & D_L \end{pmatrix} \tag{1-5}$$

where D_T and D_L are the scalar transverse and longitudinal diffusion coefficients, respectively. In the limit of $E/N \rightarrow 0$ the ionic field energy goes to zero and the ions are in thermal equilibrium with the gas. Under these conditions D_T and D_L are equal and diffusion may be characterized by the scalar diffusion coefficient D. K and D are related in the limit of vanishing electric field and ion concentration by the Einstein (or Nernst-Townsend) relation

$$K = \frac{e}{kT} D \tag{1-6}$$

where e is the ionic charge and k is the Boltzmann constant. This equation is exact and independent of the actual form of the interaction between the ions and the gas. This is a direct consequence of the ions being in thermal equilibrium with the gas and thus having a Maxwellian velocity distribution. Above the low-field limit the ions gain energy from the field and the velocity distribution is no longer known. Under

these conditions there is no simple expression such as equation (1-6) relating K and D_L or D_T. At E/N above the low-field limit it is still, however, strictly true that K, D_L, and D_T are proportional to 1/N for a specific value of E/N. Thus v_d, K_o, ND_L, and ND_T are functions of E and N only through the ratio E/N.

The relation between the mobility and electric field intensity can be derived using the Langevin equation

$$m \frac{dv}{dt} = - \alpha v + \mathfrak{F}(t) + \tilde{F}(t) \tag{1-7}$$

Here m and v are the mass and velocity of the ion, respectively, $- \alpha v$ is a damping term, $\mathfrak{F}(t)$ is an external force on the ion, and $\tilde{F}(t)$ is the random force exerted on the ion due to collisions with the gas molecules. When the ion is in a uniform electric field, the external force is $\mathfrak{F}(t) = eE$. Taking the ensemble average of equation (1-7) and considering the steady state case where $\langle \frac{dv}{dt} \rangle = \frac{d}{dt} \langle v \rangle = 0$ we have:

$$0 = - \alpha \langle v \rangle + eE + \langle \tilde{F}(t) \rangle. \tag{1-8}$$

When the average velocity $\langle v \rangle$ is small compared with the velocity of random motion, $\langle \tilde{F}(t) \rangle = 0$. However, when the external electric field becomes large, $\langle v \rangle$ also becomes large and $\langle \tilde{F}(t) \rangle$ will no longer vanish. For small electric fields we have $\langle \tilde{F}(t) \rangle = 0$ and

$$\alpha \langle v \rangle = \alpha v_d = eE \tag{1-9}$$

or

$$v_d/E = e/\alpha = K(0)e \tag{1-10}$$

The zero-field mobility is inversely proportional to the damping constant α. The value of α cannot be derived without considering the explicit interaction between the ion and gas molecules, however, for small average velocities $\langle v \rangle$, α will be constant. This demonstrates that K(0) is a constant in the low-field region. Above the low-field region we can write

$$K = v_d/E = e/\alpha + \frac{\langle \tilde{F}(t) \rangle}{E\ \alpha} \tag{1-11}$$

Here, however, the form of $\langle \tilde{F}(t) \rangle$ is unknown and the damping term may vary from being linear in v, and we can only state that the mobility will deviate from its zero-field value K(0). The Einstein relation, Equation (1-6), can also be derived from the Langevin equation [3].

In addition to the drift and diffusion of the ions, it is also possible for the ions to react with the gas to produce other ionic species. The <u>reaction frequency</u> per ion α is pressure dependent and is related to the <u>rate coefficient</u> k by

$$\alpha = k\ N^{(q-1)} \tag{1-12}$$

where q refers to an q-body reaction. The units of α are sec^{-1}, and the units of k depend upon q; for example when q = 3, k has units of

cm^6/sec. It is common practice to use the symbol k for both the rate coefficient and Boltzmann's constant. The meaning of the symbol k will always be apparent from its usage.

Measurements of mobilities, diffusion coefficients, and reaction rates are of both theoretical and practical interest. Theoretically, mobilities and diffusion coefficients provide information about interaction potentials at much larger ion-molecule separations than are attainable by conventional, single-beam techniques. Mobilities and diffusion coefficients can be measured at energies down to thermal values, whereas beam techniques are useful only above about 2 eV.

Mobilities, diffusion coefficients, and reaction rates are of interest in studies of aeronomic processes which occur in the upper atmosphere. These coefficients determine which processes occur and their relative importance in the ionized upper atmosphere. The rate of ion-ion recombination is controlled by the transport properties of the ions. This process partially determines the rate at which ionized gases neutralize through recombination. The basic transport properties are also necessary in determining the rate coefficients of ion-molecule reactions by certain experimental techniques. Because the atmosphere is a mixture of gases, free radicals, ions and water vapor the number of possible ion-molecule reactions is very large, and many reaction rates of considerable interest have yet to be measured. Ion-molecule reactions are of interest in the upper and lower atmospheres of planets (including the earth), in the physics of gas lasers, in electrical discharges, in flames, and in the radiation chemistry of gases.

Review of Past Research on Ion Swarms in Hydrogen

Albritton [4] and Miller [5] have given detailed accounts of the drift tube research performed on hydrogen ions in hydrogen gas through 1967. Experimental measurements amde prior to 1960 are in general only of historic interest since the lack of mass analysis made the ionic identity and the effects of reactions uncertain. Prior to mass analysis it was assumed that H_2^+ was the predominant positive ion produced in hydrogen gas. Although H_2^+ is readily produced by the ionization of H_2 molecules, it quickly reacts with hydrogen gas [6] by the scheme

$$H_2^+ + H_2 \rightarrow H_3^+ + H \qquad (1\text{-}13)$$

This reaction is exothermic and gives up about 1 eV of energy, and H_3^+ is a stable ion [7]. The rate coefficient of this reaction is so high that after a very few collisions, all H_2^+ has been converted to H_3^+; thus H_2^+ cannot exist in an equilibrium drift condition in hydrogen gas [6,8]. The following chronological account gives only theoretical results of interest and those experimental results obtained with mass analysis. Much work has been done on the reaction given by Equation (1-13); however, that reaction rate is known to be very large and the exact value is unimportant in the present research.

1951-1953

Wannier [9] investigated theoretically the problem of charged particles moving through a gas in a uniform electric field. All ion-molecule collisions were assumed to be elastic and emphasis was placed on the high-field region. The limiting cases of a point charge-induced

dipole and an elastic hard core interaction were considered.

For the point charge-induced dipole the interaction potential is $\sim 1/r^4$ and yields a constant mean free time between collisions of the ion and molecules. Wannier showed that when the polarization force dominates the ion-molecule interaction, the drift velocity is $\sim E/N$ for all field strengths. In the high field region, if the $1/r^4$ potential is assumed to dominate, the average energy of an ion is given by

$$E = \tfrac{1}{2} m v_d^2 + \tfrac{1}{2} M v_d^2 + \tfrac{3}{2} kT \qquad (1\text{-}14)$$

where m and M are the ion and gas molecule masses, respectively. The second term on the right relates to the fact that the ion stores random energy as the result of collisions with gas molecules.

For the elastic hard core interaction the scattering is isotropic in the center of mass frame and the mean free path between collisions is a constant. When the hard core term dominates the ion-molecule interaction the drift velocity is $\sim (E/N)^{\frac{1}{2}}$ for high field strengths.

For both interaction potentials, Wannier derived expressions for longitudinal and transverse diffusion coefficients in terms of the mean time between collisions and the ionic and molecular masses.

1958

Mason and Schamp [10] calculated the mobilities of ions in a weak electric field as a function of temperature and field strenght. Kihara's [11] extension of the Chapman-Enskog theory was used and clustering, charge exchange, and quantum effects were ignored.

Agreement between theory and experiment was shown to be good where these approximations are believed to be valid. No calculations on hydrogen ions were made.

1959

Mason and Vanderslice [12] calculated theoretically the mobilities of H^+, H_2^+, and H_3^+ ions in hydrogen gas. The long-range forces between the ion-molecule pairs were calculated theoretically and the short-range forces were obtained from low energy ion beam experiments. A total interaction potential was obtained from a composite of these two potentials. Based upon these potentials the mobilities were calculated as a function of temperature. At 300 °K the zero field reduced mobilities were calculated to be 18.3, 13.9, and 22.0 $cm^2/V \cdot sec$ for H^+, H_2^+, and H_3^+ in H_2 respectively.

1960

Varney [6] pointed out that the cross-section for conversion of H_2^+ into H_3^+ by equation (1-13) is enormous and concluded that H_2^+ could not exist under equilibrium drift conditions. He conjectured that past mobility measurements of ions in hydrogen thought to be H_2^+ were probably of H_2^+. Varney also noted the possibility of proton exchange between the H_3^+ ions and hydrogen molecules. The cross section for this reaction

$$H_3^+ + H_2 \rightarrow H_2 + H_3^+ \qquad (1\text{-}15)$$

was thought to be extremely large. The binding energies of H_2 with respect to H + H and H_3^+ with respect to $H_2 + H^+$ are 4.48 and 4.18 eV

respectively, and since these energies are close the possibility of a resonant charge exchange exists. Mason and Vanderslice did not include a charge exchange interaction in their theoretical calculation of the mobility of H_3^+ in H_2. Such an exchange force would lower the predicted mobility and possible bring the theoretical value into agreement with experimentally measured values.

1961

Barnes, Martin, and McDaniel [8] reported observing H^+, H_2^+, and H_3^+ in a drift-tube mass spectrometer. This was the first time a mass analyzer had been used to study the drift motion of ions in a gas. In support of Varney's predictions it was observed that H_3^+ was indeed the predominant ion and that H_2^+ could only be observed at very low pressures and short drift distances. H^+ ions were also observed under drift conditions and it was assumed that the two ions observed by other investigators not using mass analysis were either H^+ and H_3^+ or an impurity ion and H_3^+. No mobilities were reported at this time.

1965

Saporoschenko [13] reported on the formation of H_3^+ and H_5^+ ions in hydrogen gas using a mass spectrometer. Ions were produced in a source using electron bombardment and the relative intensities of the resulting ions were studied as a function of electron impact energy and gas pressure. In agreement with Varney and Barnes the intensity of H_2^+ was observed to decrease very rapidly with increasing pressure. The formation of H_5^+ was shown to proceed through the three-body reaction

$$H_3^+ + 2H_2 \rightarrow H_5^+ + H_2 \qquad (1\text{-}16)$$

In a later paper [14] Saporoschenko reported the first mobilities of mass analyzed H^+, H_3^+, and H_5^+ ions in hydrogen gas. The values of the reduced mobilities were measured to be 14.4, 10.2, and 9.6 $cm^2/V \cdot sec$ for H^+, H_3^+, and H_5^+ ions, respectively, at an E/N of 28 Td. However, since H^+ did not exhibit a zero slope at this E/N, it is not a zero field value.

1967

Albritton, Miller, Martin, and McDaniel [1] measured the mobilities of H^+, H_3^+, and K^+ ions in hydrogen in a drift tube mass spectrometer using a pulsed time-of-flight technique. The apparatus used has a long, variable drift length (up to 44 cm) and the measurements were made at room temperature over a substantial range in E/N. The mobilities of H^+ and H_3^+ were constant at low values of E/N and it was possible to unambiguously state a zero field reduced mobility of 16.0 and 11.1 $cm^2/V \cdot sec$, respectively, for these two ions. It was noted that at an E/N above about 150 Td there was a contribution to the H^+ ions from the H_3^+ ions breaking up in collisions with the gas. The formation of H_5^+ from H_3^+ was observed. However, no mobility of H_5^+ was reported because it was impossible to analyze the reaction effects quantitatively.

1968

Miller, Moseley, Martin, and McDaniel [2] reported additional measurements with the drift-tube mass spectrometer. The mobilities of H^+, H_3^+, Li^+, Na^+ and K^+ in H_2 and the corresponding ions in D_2 were measured. In each case an unambiguous zero-field reduced mobility was obtained. The mobilities of corresponding ions in H_2 and D_2 were shown to scale, according to Langevin's theory, proportional to the

inverse square root of the reduced mass of the ion-molecule combination. The rate coefficients for the reactions

$$H^+ + 2H_2 \rightarrow H_3^+ + H_2 \qquad (1\text{-}17)$$

and

$$D^+ + 2D_2 \rightarrow D_3^+ + D_2 \qquad (1\text{-}18)$$

were measured using an attenuation method. The reactions were shown to be three-body reactions, with rate coefficients independent of E/N below 28 Td. The rate coefficients assigned were 3.2 and 3.0 x 10^{-29} cm^6/sec, respectively.

1969

Fleming, Tunnicliffe, and Rees [15] measured the ratio (D_T/K) for H^+ and K^+ and the mobility of ions identified as H_3O^+ in H_2 using a drift-tube with a mass analyzer. They noted that many experimenters in the past had measured the mobility of an ion in H_2 with a value of approximately 12.5 $cm^2/V \cdot sec$. Since these previous experiments were done without the benefit of mass analysis it had been assumed that the ionic species present was H_3^+. Fleming, et al., suggested that the ion actually present during these earlier measurements was H_3O^+. They measured the mobility of an ion identified as H_3O^+ and found it to be 12.6 $cm^2/V \cdot sec$. The problem is left unresolved, however, as to how the large quantities of impurity has entered the systems thought to contain only hydrogen.

Goals of Present Research

Since Albritton and Miller first reported on positive ions in hydrogen great strides have been made in data analysis and data gatherings techniques. Using these new techniques it is the goal of the present research to:

1. Obtain unambiguous zero-field reduced mobilities for H^+ and H_3^+ in H_2 and D^+ and D_3^+ in D_2.

2. Obtain longitudinal diffusion coefficients for these same ions and compare them with existing theory.

3. Obtain the rate coefficient of the reactions between H^+ and H_2, and D^+ and D_2 using a detailed curve fitting scheme.

4. Investigate any negative ions that may be formed in hydrogen and deuterium gas, their mobilities, longitudinal diffusion coefficients, method of formation and any reactions that may occur.

CHAPTER II

APPARATUS

General Description

The apparatus used in the present research is a drift-tube mass spectrometer of ultra-high vacuum construction. The basic apparatus was designed and constructed by D. L. Albritton, T. M. Miller, D. W. Martin, and E. W. McDaniel and was completed early in 1967. Since then improvements have continuously been made in gas handling, pressure measurement, ion production and detection, and analysis. Since the basic apparatus has been described in detail elsewhere, only a brief description will be given here. A detailed description will be given, however, of modifications incorporated for the present research and areas of importance not sufficiently covered previously.

Figure 1 shows a cut-away view of the apparatus and a block diagram of the ion production and detection electronics. With the isolation valve closed, gas is admitted into the drift-tube through a servo-controlled leak valve. The pressure is continuously measured by a capacitance manometer and is maintained at a constant value by controlling the servo valve with an automatic pressure controller.

The drift field guard rings maintain a uniform electric field within the drift region. The ion source is moveable and the total drift distance may be varied between 0 and 44 cm. Ions are produced in the source by either electron bombardment or thermionic emission.

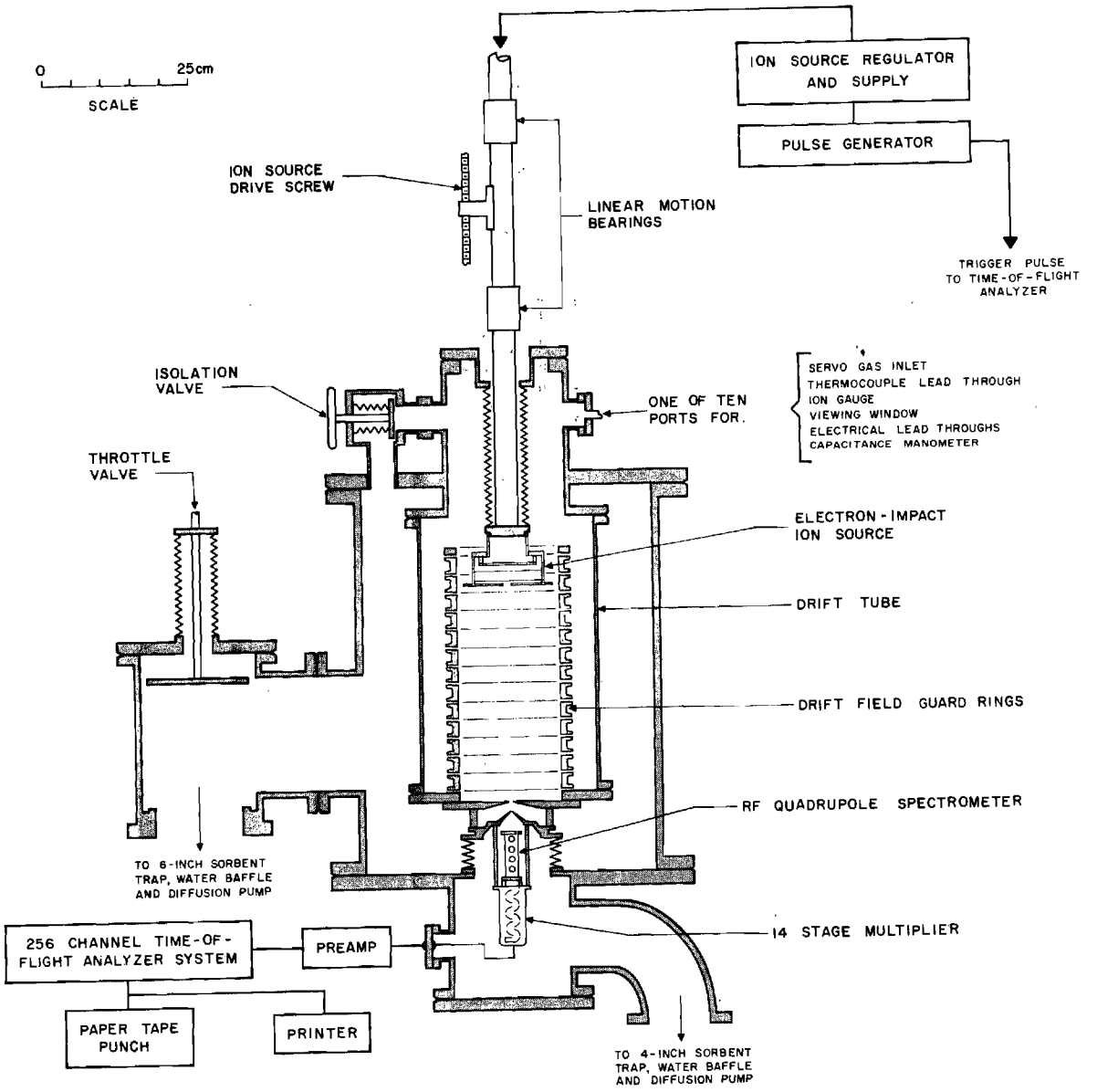

Figure 1. Sectioned View of the Drift Tube, the Outer Vacuum Enclosure and the Analysis Region.

These ions are gated into the drift region in temporally short pulses (about 1 μsec) through a circular hole in the source. Each ion swarm gated into the drift region subsequently diffuses and in some cases undergoes ion-molecule reactions as it drifts down the tube under the influence of the uniform axial electric field. A sample of the ions reaching the far end of the drift region passes through a small aperture (0.035 cm diameter, located on the axis) into a differentially pumped region, and thence through a skimmer, focusing elements and to an rf quadrupole mass filter. Ions of the particular species which the filter is set to pass are detected by a channel electron multiplier. Voltage pulses generated by the detection of single ions are time sorted by a 256 - channel time-of-flight analyzer. The accumulation of time-sorted counts from many thousands of identical source bursts produces a histogram of the transit times of the ions through the apparatus for a particular drift distance, gas pressure, and drift field intensity. Such "arrival time spectra" are obtained successively for each species of ions present in the drift tube over a wide range of the experimental variables, and the drift velocities, longitudinal diffusion coefficients and reaction rates, are calculated from these spectra by methods discussed in Chapter III.

Vacuum System

The apparatus is stainless steel throughout and all vacuum seals are metal gaskets to reduce outgasing. The vacuum chambers are evacuated by oil diffusion pumps using Convoil 20 diffusion pump oil. Silicone base pump fluids are not used since they might coat the surfaces of the drift region in event of an accidental venting of the

system to the atmosphere. Because of their low vapor pressure it might be possible to have silicone oil within the drift region without noticing an increase in base pressure. However, this insulating coating could charge up and deflect the ions in the drift region, giving erroneous experimental results. The diffusion pumps and the vacuum chambers are separated by water-cooled optically-opaque baffles and molecular sieve traps to reduce backstreaming. The diffusion pumps are backed by a mechanical forepump which is also filled with Convoil 20 to prevent any problems of forepump oil creepage into the diffusion pumps.

Bakeout

The outside of the apparatus is encased in heating mantles for system baking. The region between the drift-tube and the drift field guard rings is heated by nichrome wires. All valves are of ultra-high vacuum and all metal construction and are fitted with bakeout clamps and ovens during a system bake. When baking the system, the molecular sieve traps are baked at 450°C and the rest of the system is baked at 250°C while under high vacuum. Because of the large mass of the system it takes 24 hours for it to reach final baking temperatures throughout. The system is baked for an additional 24 hours at this temperature and then allowed to cool. Cooling to ambient temperature takes three days. At this time base pressures of about 1×10^{-9} Torr are obtained. With the isolation valve closed the base pressure in the drift-tube does not exceed 1×10^{-7} Torr.

Temperature Measurements

The temperature of the drift gas is determined by three chromel-alumel thermocouples attached to the top, center, and bottom drift

field guard rings. These thermocouples are Omega Engineering Corp. type CHAL-032 and have an accuracy of ± 0.1°C. The vacuum feedthroughs between the drift tube, outside chamber, and the outside of the apparatus have chromel-alumel conductors to eliminate any contact potentials that could be introduced due to dissimilar metal connections. The thermocouple potentials are reduced to a standard of 0°C by a thermocouple compensator type CJ-K, also from Omega Engineering Corp., with an accuracy of ± 0.25°C. The thermocouple compensator replaces the usual ice bath as a reference for temperature with a mercury cell and a voltage dividing network. A calibration variable resistor is adjusted to give an output potential that one would obtain from a chromel-alumel thermocouple at 0°C. The thermocouple compensator is calibrated by reference to a chromel-alumel thermocouple in a methyl alcohol bath enclosed in a dewar. The temperature of the bath is measured by two precision mercury thermometers with an accuracy of ± 0.1°C. The two thermometers and the thermocouple are connected to an aluminum block and immersed in the methyl alcohol bath. The aluminum block, methyl alcohol bath, and dewar provide a temparature reference with a large thermal inertia.

The potential of the compensated thermocouples is measured with a Fluke differential voltmeter type 881A. The overall accuracy of an individual temperature measurement is considered to be ± 0.5°C. However, in the process of producing ions, the source is heated and produces a temperature gradient within the drift region. To ensure that the temperature is well known, no data are taken when the temperature difference between the top and bottom guard rings exceeds 1.0°C. The

overall accuracy of a single temperature measurement of the gas in the drift region is estimated to be ± 2.0°C, or ± 0.7 percent at 300°K.

Drift Distances and Potentials

The drift region is bounded by 14 drift field guard rings radially, the grounded end plate (or exit aperture plate) on the lower end, and the source front plate (or drift field termination plate) on the upper end (Figure 2). The drift distance is the distance between the source front plate and the end plate. There are seven preset drift distances that can be selected automatically. At any of these seven positions the lower edge of the source front plate is positioned at the center of a guard ring. At position seven the source front plate is located at the center of the 14th guard ring and corresponds to the longest drift distance (~ 44 cm). The other six positions are evenly spaced at intervals of ~ 6.25 cm and are located at the centers of alternate guard rings. Thus position six is located at the center of guard ring 12, etc., and the shortest drift distance, position 1, is located at the center of guard ring two and has a drift length of ~ 6.25 cm. The location of the seven positions is precisely controlled by seven microswitches [16]. The repeatability of the source location in successive positionings is measured to be within ± 0.001 inches and the drift distances are conservatively estimated to be known within ± 0.003 inches.

When the source is located at a specific position, the source front plate is placed at the same potential as the corresponding adjacent guard ring. The potentials of the guard rings are maintained at accurately known and uniformly spaced potentials by a Fluke Model

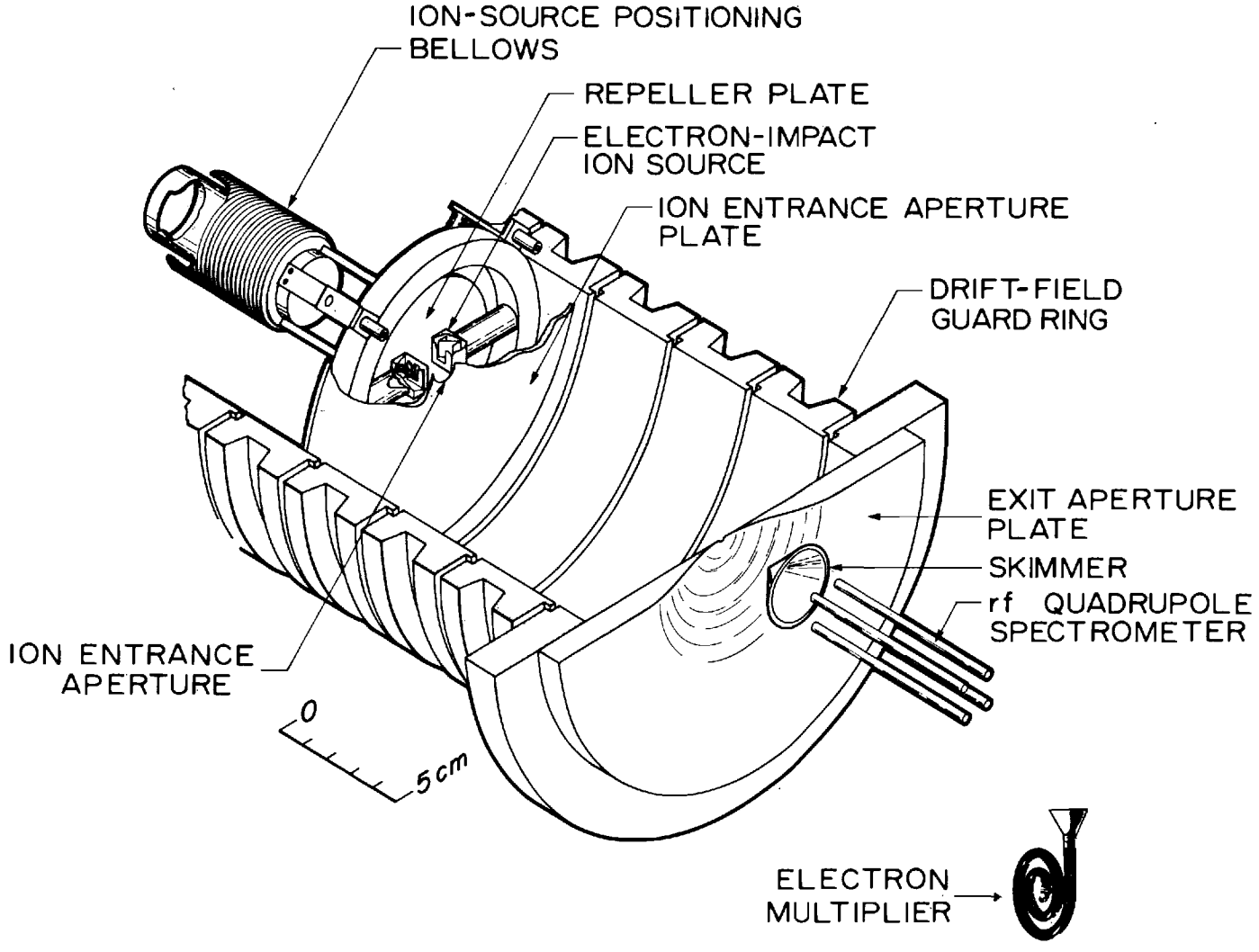

Figure 2. Cut-away View of the Drift Chamber and Mass Analysis and Detection Apparatus.

301E dc power supply (0.005 percent stability per hour) connected across a string of 0.1 percent wire-wound resistors. The potentials are measured by a Fluke Model 881A differential voltmeter (± 0.01 percent + 5 μvolts).

Albritton [17] has shown the electric field to be uniform within 0.1 percent for all points within 4 cm of the axis and within 1.0 percent for all points within 6 cm of the axis. The electric field intensity within this region is given by

$$E = V/d \qquad (2\text{-}1)$$

where V is the potential of the source front plate and d is the drift distance. For the electric field to be the same for each position of the source this ratio must remain constant for each drift distance. Table 1 lists the measured drift distances and potentials and electric fields for each position when 70 volts are applied across the resistor chain supplying the potentials to the guard rings. The electric field at position 7 is taken as the experimental value and the maximum variance of electric fields for different positions from this value is + 0.18 percent when the source is at position 1.

Pressure Measurement and Calibration

The pressure is measured using a MKS "Baratron" capacitance manometer. The Baratron consists of three units: (1) the pressure measuring head, (2) an electronic pressure indicator, and (3) a temperature control unit for precise regulation of sensor temperature. A type 90H-1 all-metal pressure head capable of being baked at up to

Table 1. Tabulation of Drift Distances, Potentials, and Electric Field Intensities

Position	Drift Distance cm	Drift Potential Volts	Drift Field Volts/cm
7	43.7751	70.0000	1.5991
6	37.5158	60.0010	1.5994
5	31.2656	50.0037	1.5993
4	25.0088	40.0060	1.5997
3	18.7521	30.0042	1.6000
2	12.4991	20.0052	1.6001
1	6.2441	10.0028	1.6020

450°C is used in the present research. With this pressure head and with the electronic indicator on the most sensitive scale, a full scale deflection corresponds to ± 0.0003 Torr. The pressure indicator is normally operated in the null mode. The desired pressure is selected on panel dials of the pressure indicator and gas is let into the drift chamber to null out the pressure indicator reading. Once the drift chamber is filled to the desired pressure, it is maintained by a Granville-Phillips Automatic Pressure Controller which receives an input from the Baratron. The pressure can be automatically maintained at a preset value within ± 0.0001 Torr.

The pressure sensing head and its matching preamplifier are calibrated at the factory using dead weight testing. The calibration procedure is as follows: A piston of accurately known cross section and weight is placed in a cylinder whose top is open to the atmosphere.

To eliminate friction between the piston and the cylinder, the piston is spun by hand and the air between the cylinder wall and the piston forms a cushion or air bearing. The pressure in the cylinder is the atmospheric pressure plus the weight of the piston divided by the area of the piston. The pistons are so constructed that additional donut shaped weights may be added on a peg in the center of the piston. By leaving the reference side of the manometer open to the atmosphere and connecting the unknown side of the manometer to the cylinder, a pressure differential of the piston weight divided by piston area is across the manometer. The gain of the preamp associated with the specific pressure head is adjusted so that the correct differential pressure is indicated. MKS has found this calibration procedure to be highly repeatable and accurate; however, the calibration is not certified by the National Bureau of Standards.

Because of the construction of the pressure head, it must be recalibrated when operated under conditions of high vacuum. The pressure head is basically ahhollow metal cylinder with a thin metal diaphragm in the middle. This diaphragm is welded to the cylinder wall and forms an air-tight seal between the two halves. Wehn a pressure differential is placed across the two ends of the pressure head the metal diaphragm flexes toward the side with the lower pressure. By placing two rigid metal plates on either side of the diaphragm a capacitor is formed and when the metal diaphragm flexes the capacitances of the two sides change. By measuring the change in capacitance one has a measure of the change in pressure across the two ends of the pressure head. The system is calibrated with atmospheric pressure on

both the inside and the outside of the pressure head. However, in the present apparatus both ends of the head are connected to relatively low pressure (< 1 Torr) while the outside of the head is still at atmospheric pressure. This causes the outside of the head to push slightly inward and in the process change the tension in the matal diaphragm. This change in tension necessitates the recalibration of the pressure head. To prevent any change in tension of the diaphragm due to thermal stress, the head is maintained at 50°C ± 0.1°C by a thermal oven from MKS.

It is worth noting that the need of recalibration could possibly be eliminated by placing the pressure head in a vacuum chamber that could be evacuated to a pressure $\lesssim$ 10 Torr. This could have two distinct advantages. (1) It would eliminate the need of recalibration. (2) The accuracy of calibration by dead weight testing is much greater than that by any means under vacuum conditions. Thus pressure measurement accuracy at low pressures could possibly exceed that of other more complicated means (i.e., McLeod Gauge).

In the present research the pressure was recalibrated using a method devised by McDaniel and Martin [18]. The zero field reduced mobility of K^+ ions in N_2 has been recently measured by several experimenters. Their values cluster about an average value of 2.54 $cm^2/V \cdot sec$ with a spread of less than $\frac{1}{2}$ percent. Knowing all other experimental variables except the accuracy of the pressure measurement, the zero-field reduced mobility of K^+ in N_2 is measured. The pressure calibration is then adjusted so that the zero-field reduced mobility is exactly 2.54 $cm^2/V \cdot sec$. The reduced mobility K_o is defined by

$$K_o = K \left(\frac{P}{760} \right) \left(\frac{273.16}{T} \right) \qquad (1\text{-}2)$$

If K_o calculated using the uncorrected pressure is too high, then the pressure must be corrected downward. In the present calibration runs, the average zero-field reduced mobility is determined to be 2.580 $cm^2/V \cdot sec$ in 12 measurements. The standard deviation of these measurements is ± 0.005 $cm^2/V \cdot sec$ or ± 0.10 percent. The correction factor thus obtained is 0.9843 in excellent agreement with the correction factor of 0.9866 previously measured.

This method of pressure calibration has several advantages. (1) It involves a measurement readily amenable to the experimental apparatus. (2) The calibration thus obtained is probably accurate within ± 0.5 percent. (3) If the zero-field reduced mobility of K^+ in N_2 is shown to be different than 2.54 $cm^2/V \cdot sec$, all data taken can readily be corrected using the correct value of $K_o(0)$.

Gas Purity and Supply

Gas to be used is stored in an all metal gas feed line. This feed line is connected to the drift region by a servo-controlled leak valve. During preparation for measurements on a different gas, the feedline is baked while under a high vacuum and the pressure in the feed line is measured by a nude ion gauge. Upon completion of baking and after cooling the base pressure in the feedline is $< 1 \times 10^{-7}$ Torr. When the feedline is isolated from pumping, the pressure in it does not rise above 5×10^{-6} Torr.

In the present research only hydrogen and deuterium gas is used. The gases used are Matheson's "C.P." with a stated purity of 99.5% for deuterium and Air Product's "UHP" with a stated purity of 99.995% for hydrogen. The gas is further purified by passage through a silver-palladium diffusion tube. The inside of the tube is connected to the feedline and the outside of the tube is jacketed by a hollow pyrex cylinder. Pure hydrogen or deuterium is placed in the pyrex cylinder at a pressure of about 5 psig. When the palladium tube is heated above 150°C, hydrogen (or deuterium) diffuses through into the feedline.

To maintain a constant pressure in the drift region gas is continuously let in through the servo-controlled leak valve and is continuously being pumped away through the exit aperture. If the gas in the feedline is not replenished the pressure in the feedline slowly drops as the gas is leaked into the drift tube. The changing pressure differential between the feed line and the drift-tube requires the servo-controlled leak valve to be continually opened further to maintain the same gas flow rate into the drift-tube. Operationally, this makes the pressure control in the drift-tube more difficult. By maintaining a constant pressure in the pyrex cylinder around the palladium tube, hydrogen is continuously replaced in the feed line and a constant pressure differential is maintained.

The purity of the gas has been checked by making mass scans, with the rf quadrupole mass spectrometer, of ions produced by electron bombardment. No appreciable impurities were detected between 0 and 120 amu and the use of a refrigerated vapor bath to reduce impurities was not necessary.

Ion Source

Ions are produced in the source either by electron bombardment of the drift-tube gas or by thermionic emission [19]. In the present research we are concerned only with ion production by electron bombardment.

Figure 3 is a cross-section of the source and a block diagram of the associated power supplies and pulsers. The filament emits electrons which are accelerated across the source ionization region into the collector. The filament is a thoriated-iridium ribbon from a Veeco ionization gauge tube, type RG-75K. A constant current (± 0.03 percent for 8 hours) is maintained through the filament by a Harrison Type 6263 power supply. The control plate is normally biased to prevent electrons from escaping the filament enclosure. Periodically the control plate is pulsed to allow electrons to cross the ionization region of the source. The ionization region of the source is open to the drift tube gas and is thus at the same pressure as the drift region. The control plate is shaped so that the electrons are admitted in a thin wide strip. This causes ion production to occur in a plane in the source parallel to the front plate and over a wide enough area to fill the entrance aperture. The electrons are collected by a metal cup within the collector enclosure. To ensure that electrons are not scattered into the drift region by collisions with the gas, a magnetic field of about 100 gauss is applied along the path between the filament and collector. This confines the motion of scattered electrons to tight helices around the magnetic field lines. In the present research, measurements were made with and without the magnet to

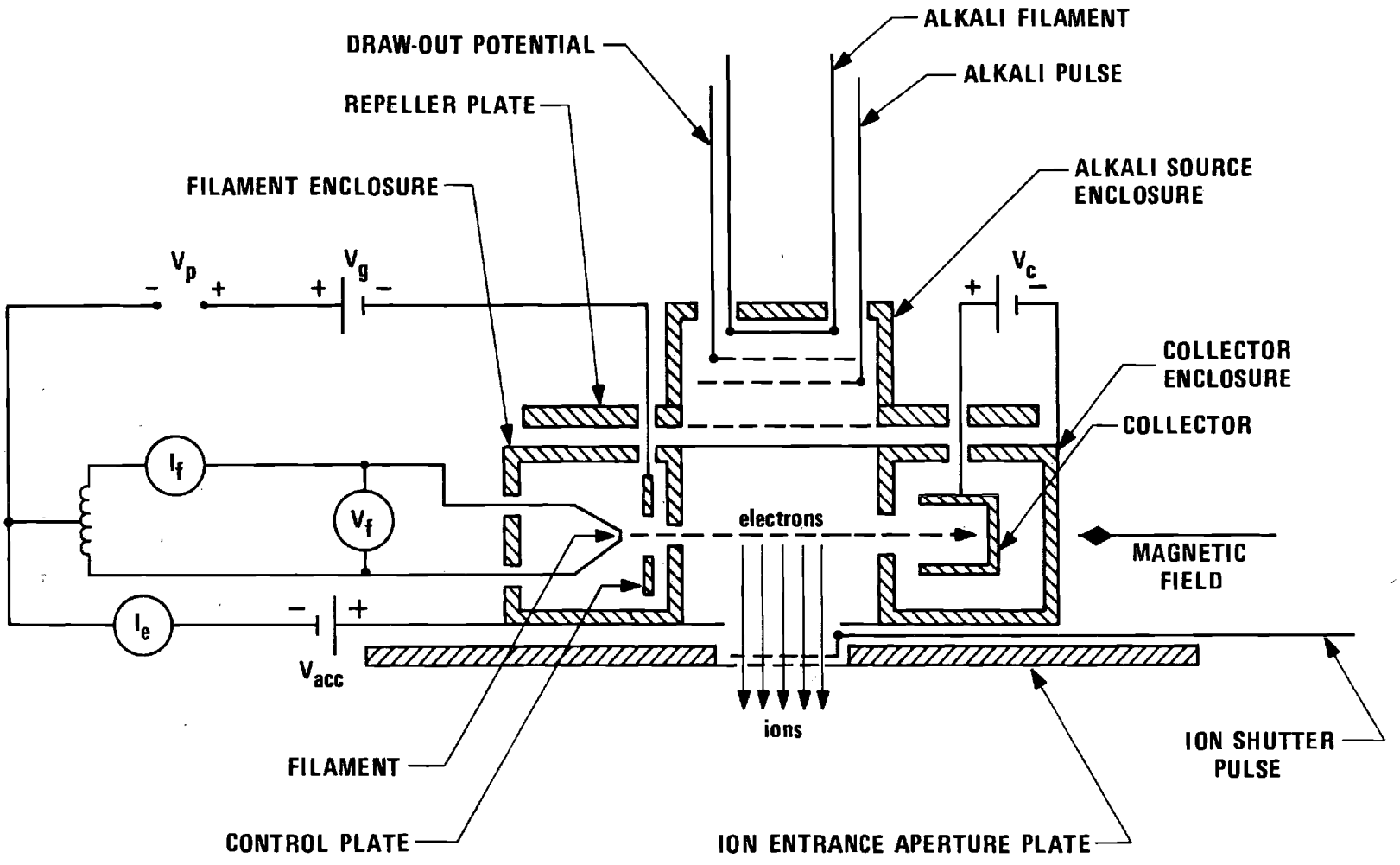

Figure 3. Schematic Diagram of the Ion Source. (The Alkali Source is Mounted Above the Electron Impact Ion Source.)

determine its effect. No appreciable difference was noted and the magnet was left in the source.

Within the ion production region of the source an electric field is maintained parallel to the drift region electric field by placing potentials on the repeller plate, collector and filament enclosures, and the front plate. This electric field normally has the same magnitude as the electric field in the drift region, although it can be adjusted to any desired valve. When an ion is produced it moves along the electric field toward the ion entrance aperture. The ion shutter or Tyndall grid is normally biased to prevent ions from entering the drift region. A temporally short pulse (about 1 μsec) is applied to the Tyndall grid and ions are admitted into the drift region.

The energy of the electrons is controlled jointly by the filament bias, V_{acc}, and the collector potential, V_c. Since there is a potential drop across the filament of about 4 volts, the electrons are not monoenergetic.

For production of ions the source is set up by the following procedure. (1) Filament current is adjusted for 4.0 - 5.5 amperes, depending on gas pressure. (2) Filament bias, control plate bias, and collector potentials are adjusted to maximize production of the desired ion. (3) The control plate is biased to prevent electrons from escaping the filament enclosure and thus prevent ion production. (4) The control plate is periodically pulsed to allow electrons to escape in short bursts of 10 - 100 μsec in length. Thus ions are produced and the magnitude and width of the pulse are adjusted to maximize ion production. (5) The Tyndall grid is biased to prevent ions from

entering the drift region. (6) The Tyndall grid is pulsed to allow ions to enter the drift region. The time between the control plate pulse and the Tyndall grid pulse is varied to maximize ion production. The center of the Tyndall grid pulse is defined as time t = 0. The width of the Tyndall grid pulse is kept at the minimum value that will maintain sufficient ion production. In the analysis (Chapter III) it is assumed that the source is a δ-function in time, i.e., all ions are created at the same time. In practice the width of the Tyndall grid pulse is the length of time over which ions may be considered to be produced. Since the time-of-flight analyzer divides time into segments of 0.25 - 64 μsec, the criterion for a δ-function source is that the Tyndall grid pulse be no wider than one channel width of the analyzer.

Ion Selection and Detection

When an ion leaves the drift region through the exit aperture, it enters a differentially pumped region and undergoes no further collisions with the gas. The ions are accelerated through the skimmer by an electric potential on the skimmer (Figure 4) and into the analysis region which is maintained at a low pressure ($< 1 \times 10^{-5}$ Torr) by a 4 inch diffusion pump. The skimmer, both focusing lens elements, and the quadrupole pole pieces are externally biased to provide the maximum ion detection efficiency. It has been determined that the transmission efficiency of the quadrupole mass filter does not increase appreciably when the bias is above about 50 volts. The skimmer and focusing elements are biased between 10 and 40 volts such that as the ion traverses the analysis region it is never decelerated by a lower potential. Two general properties of a quadrupole mass filter are

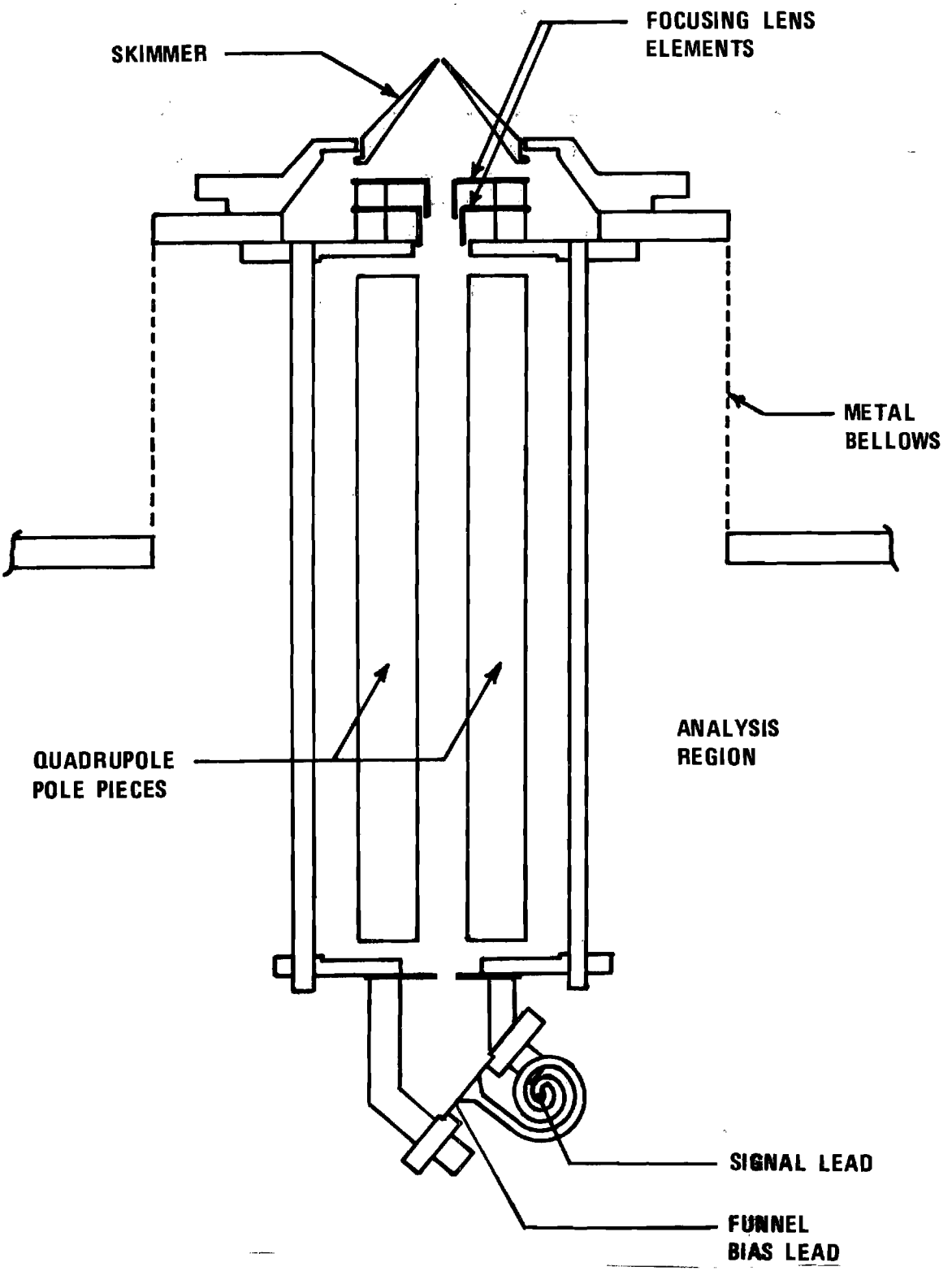

Figure 4. Cross Section of the Skimmer, Focusing Elements, Quadrupole Mass Filter, Exit Aperture Plate, and the Channeltron.

that (1) increasing the length of the pole pieces increases the resolution and the capability of handling ions of higher energies and (2) increasing the pole diameter increases the sensitivity. The quadrupole mass filter used is an Extranuclear Labs Type 324-9 which has both a long length (22 cm) and a large pole diameter (1.90 cm). This filter coupled with the appropriate driving head has a mass range of 0 - 352 amu and a mass resolution (full width at half maximum) of greater than 800. Three heads are used in the present research; Types A, B, and D_1 with mass ranges of 0 - 16, 29, and 124 amu respectively. In the present research it was determined that head D_1 could not distinguish between masses 1 and 3 at the low end of the mass range. Hence head A was used for all measurements except when making mass scans to determine impurity levels, and pressure calibration. This head provided excellent resolution over the entire mass range.

Ions exiting the quadrupole mass filter go through an aperture plate with a 7/32 inch diameter. These ions are detected by an Amperex Channel Electron Multiplier Type B419BL/01. This multiplier has a large (1 cm) diameter funnel on the front and is capable of withstanding baking to 400°C. Channel electron multipliers (here after referred to as channeltrons even though this is a trade name of Bendix) are notoriously fragile both mechanically and electrically. To facilitate mounting and handling, the channeltron is mounted on a piece of machined SUPRAMICA (from Mycalex Corp. of America) and the funnel glued in place with Eccobond 57C conductive cement (from Emerson and Cuming, Inc.). To prevent mechanical stress the signal end of the channeltron is left free. The channeltron is operated with

the signal lead bias 3000 volts higher than the funnel bias. During operation with positive ions the bias potentials used are -3000 volts and 0 volts for the funnel and signal leads, respectively; with negative ions +1000 volts and +4000 volts are used for the funnel and signal leads, respectively. The signal lead is connected to an isolation device (Figure 5) which protects the preamp from high voltage. The blocking capacitor passes small pulses from the channeltron to the preamp. This capacitor is chosen relatively large (500 pfd) so that the sharp pulses from the channeltron are not attenuated. The 0.1 MΩ resistor prevents the pulses from going to ground in the power supply instead of going to the preamp. The back-to-back silicon diode arrengement shorts any signals larger than about 1.2 volts to ground; however, the incoming signals from the channeltron are smaller than this and the diodes have a very large resistance for small (< 1.2 volts) signals. The purpose of the diodes is to protect the preamp from high-voltage transients when the signal lead power supply is turned off and on.

Ions that are rejected by the mass filter may strike the pole pieces or other metal surfaces and emit photons. To prevent these photons from being counted as ions, the channeltron is mounted off-axis so that it cannot "see" the inside of the mass filter. With the aperture plate installed on the bottom of the quadrapole and the channeltron mounted off-axis the background count rate is reduced to below 2 counts/100 seconds.

Figure 5 schematically shows the ion detection and signal processing equipment.

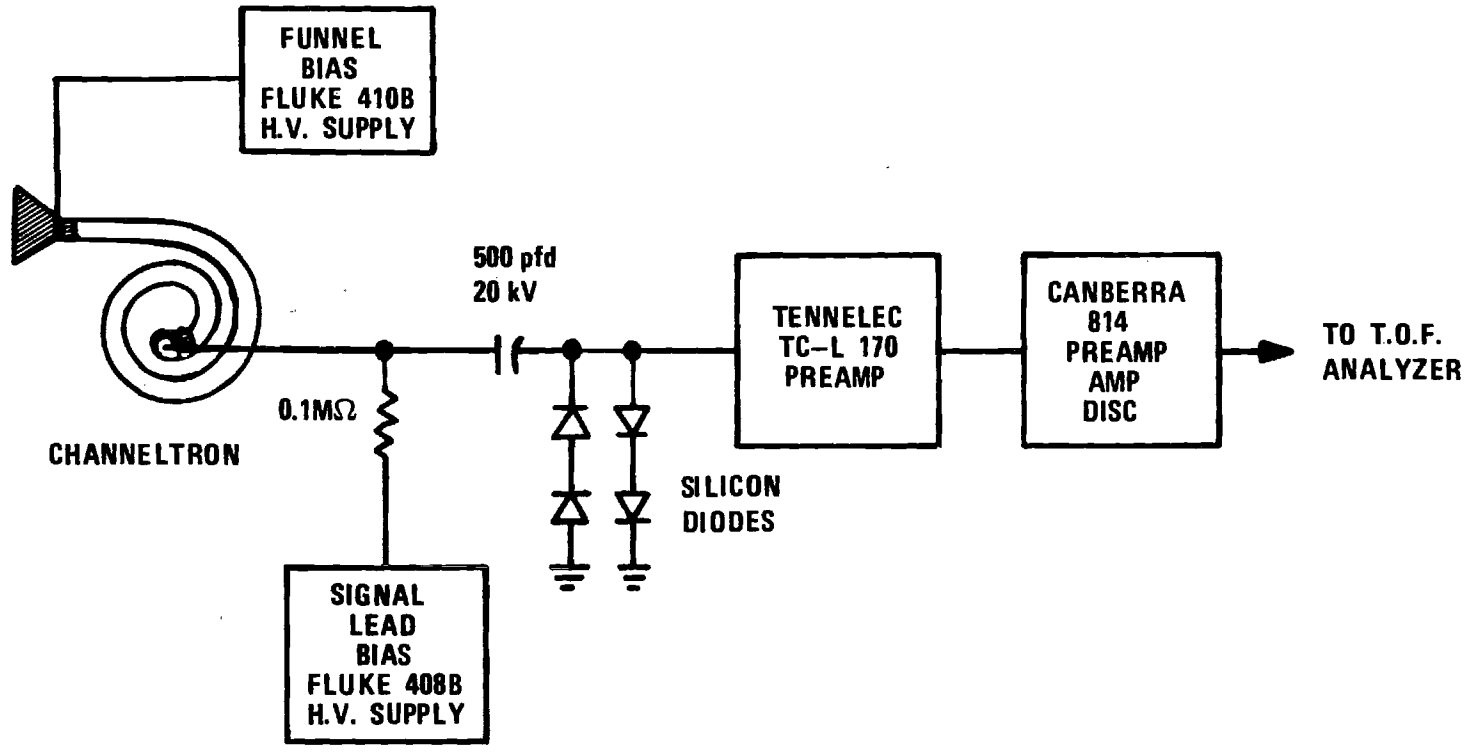

Figure 5. Schematic Diagram of the Isolation Device, and Signal Processing Electrons for the Detection of Ions.

Timing

The timing of the control plate pulse, Tyndall grid pulse, and the start of the time-of-flight analyzer is accomplished with a Hewlett-Packard Type 5330B Preset Counter.

The time-of-flight analyzer has a fixed number of channels (256) in which to sort the detected ions. The channel width (c.w.) is adjustable by powers of two from 0.25 to 64 μsec per channel; thus the total time covered by the analyzer is T = 256 x c.w.. To obtain the greatest detail of an arrival time spectrum it is necessary to spread the spectrum over as many channels as possible. This is accomplished by delaying the start of the analyzer to slightly before the first ions begin to arrive. The channel width is then adjusted so that the arrival time spectrum covers as many channels as possible and still lies totally within the time covered by the analyzer. Since the channel widths are adjustable by powers of two, it is always possible to fill at least half the channels (128) with a specific arrival time spectrum.

The Preset Counter controls sequencing of the control plate pulse, Tyndall grid pulse, and the start of the time-of-flight analyzer by providing timing pulses at "preset" times. The counter has an internal 1MHz crystal oscillator. By dividing the oscillator frequency by any integral number, N, between 1 and 10,000, a variable time base of N μsec is available. This time base is then counted by an internal Counting Register. The counting register is initially set at a preset value, R, and each time base pulse increases the value in the counting register by 1. The counting register continues counting through a preset value LO and up to a preset value HI. When the counting register

reaches the HI value, it is automatically reset to the value R and begins the counting sequence again. The cycle thus repeats itself every (HI-R) timing pulses or every N x (HI - R) μsec. This timing sequence correlates the control plate, Tyndall grid, and start pulse for the analyzer as follows: Normally N = 1, and the time base is in units of 1 μsec. The R value is set at a negative value (~ - 100 μsec). When the counting register reaches zero, the Tyndall grid is pulsed and this defines time t = 0. When the counting register reaches the LO value, the analyzer is started. The HI value is adjusted such that all 256 channels of the analyzer have been scanned and the analyzer has had time (16 μsec) to reset to channel 1 before the timing sequence begins again. Thus N x (HI - LO) > (c.w. x 256) + 16.0 μsec. The reset value R is used to pulse the control grid and occurs before t = 0. One complete sequence is shown in Figure 6a: (1) The control plate is pulsed when the counting register reads R. This corresponds to a time t < 0. (2) The Tyndall grid is pulsed when the counting register reads 0. This corresponds to time t = 0. (3) The time-of-flight analyzer is started when the counting register reads LO. This corresponds to some fixed delay time t > 0. (4) The counting register is reset to R when it has counted to the value HI. Thus HI and R occur at the same physical time; however, the HI value refers to the timing sequence just completed and the R value refers to the timing sequence just starting. This allows the arrival time spectrum to be spread over as many channels of the analyzer as possible.

This procedure produces one burst of ions which drift the length of the drift-tube and are then detected. The analyzer is waiting on

the arrival of the ions from the time they are created until the LO pulse is received. Thus the analyzer is "dead" for at least (LO - R) x N μsec. A technique called multipulsing is used to decrease this dead time and thereby increase the rate of data taking. By this procedure, several bursts of ions are simultaneously drifting in the drift region. To accomplish this the timing is initially set up as described previously (single pulsing - Figure 6a). A convenient repetition time, larger than the time covered by the analyzer and its reset time, is chosen. For example with a channel width of 1 μsec, the total time covered by the analyzer is 256 μsec and the reset time of the analyzer is fixed at 16 μsec. Thus a convenient repetition time is 300 μsec. The HI value is then increased so that the time difference between the R value and the HI value, N x (HI - R) μsec, is an integral multiple, m, of the repetition time (Figure 6b). The HI value is now set such that the value (HI - R) x N is equal to one repetition time and the LO value is decreased in multiples of one repetition time until the LO value lies between R and HI (Figure 6c). The equipment is now multipulsing and m bursts of ions are in the drift chamber at any particular time. Figure 6c demonstrates multipulsing where m = 2. The preset counter is repeatedly counting from R <u>through</u> LO <u>to</u> HI. Now, however, a particular LO pulse starts the analyzer to detect the burst of ions created by the R pulse on the m^{th} previous preset counter cycle. Similarly, a burst of ions created by a particular R pulse will be detected by the analyzer started on the m^{th} LO pulse in the future.

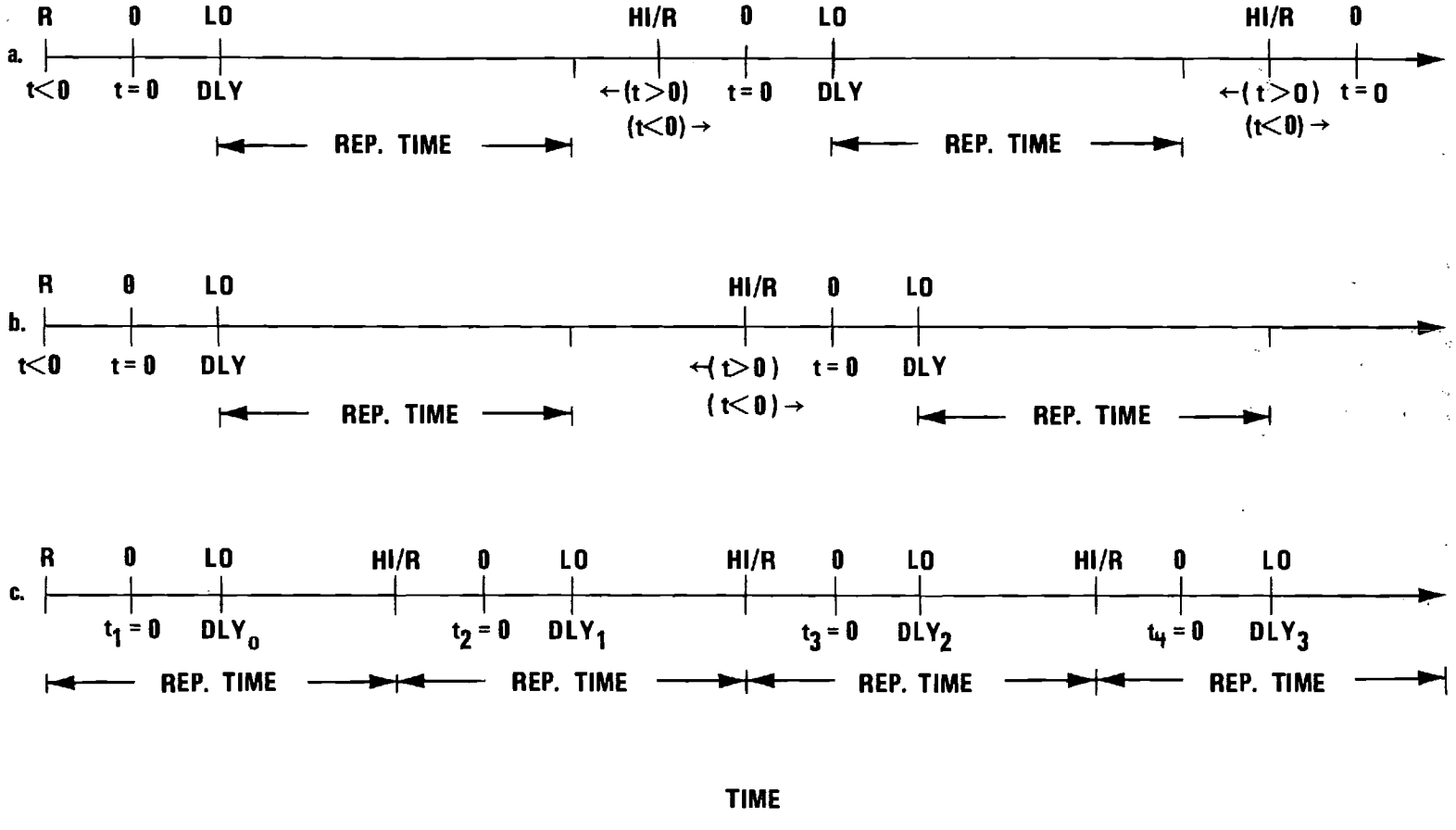

Figure 6. Timing Diagram for Sequencing of Control Plate Pulse, Tyndall Grid Pulse, Start of Analyzer, and Multipulsing.

CHAPTER III

ANALYSIS

In this section we will outline the analysis necessary to evaluate the transport coefficients of ions in swarm motion. To do this we will solve the applicable transport equation with the boundary and initial conditions specified by the experimental apparatus. Because of the large size of the drift region we assume it to be infinite in this analysis though it can be extended to finite boundary conditions. We first consider ions which may undergo depleting reactions only. Secondly we consider ions which may react with the drift gas to produce secondary ions which then may in turn react to produce ternary ions, etc. This analysis was developed by Ian Gatland [20] to describe the drift motion of two species of ions which react with the drift gas to produce each other. This reaction can be characterized by:

$$A \underset{\alpha_{AB}}{\overset{\alpha_{BA}}{\rightleftharpoons}} B$$

where α_{ij} is the reaction frequency to species i from species j. This type of reaction is referred to as a foreward-backward or "fore-back" reaction. Once the analysis is developed it is immediately applicable to more complicated reaction schemes such as:

$$A \rightarrow B \rightarrow C \ ,$$

$$A \rightleftarrows B \rightarrow C \ ,$$

and

$$A \rightarrow B \rightleftarrows C \ , \text{ etc.}$$

Reactions of the form

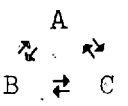

can also be solved; however, to date the latter reaction scheme must be expressed approximately to whatever degree we care to calculate using a power series in the reaction frequencies.

The Transport Equation and Solution

The present experimental apparatus is cylindrically symmetric around the z-axis. The electric field $\vec{E}$ and thus the drift velocity $\vec{v}_d$ are along the z-axis. Since the electric field defines a unique direction the rate of diffusion of the ions will in general be different along the electric field lines and perpendicular to the electric field lines. Thus in general the diffusion must be characterized by a tensor $\overrightarrow{\overrightarrow{D}}$ which because of the choice of axes will be diagonal and of the form:

$$\overrightarrow{\overrightarrow{D}} = \begin{pmatrix} D_T & 0 & 0 \\ 0 & D_T & 0 \\ 0 & 0 & D_L \end{pmatrix} . \qquad (3\text{-}1)$$

D_T and D_L are the scalar transverse and longitudinal diffusion coefficients respectively. The ionic current density $\vec{j}$ is (from Equation 1-3):

$$\vec{j}(\bar{x}) = \vec{v}_d n(\bar{x}) - \vec{\vec{D}} \cdot \vec{\nabla} n(\bar{x}) \tag{3-2}$$

where $n(\bar{x})$ is the ionic number density and $\bar{x}$ is a 4-vector and refers to x, y, z and t.

The continuity equation is:

$$\vec{\nabla} \cdot \vec{j}(\bar{x}) + \frac{\partial n(\bar{x})}{\partial t} + \alpha n(\bar{x}) = \beta(\bar{x}) \tag{3-3}$$

where α is the reaction frequency to all other species of ions and $\beta(\bar{x})$ is a source of ions as yet of unspecified nature.

If we define the operator $\mathcal{D}$ by

$$\mathcal{D} = D_T \left(\frac{\partial^2}{\partial x^2} + \frac{\partial^2}{\partial y^2} \right) + D_L \frac{\partial^2}{\partial z^2} - v_d \frac{\partial}{\partial z} - \alpha \tag{3-4}$$

combining Equations (3-2) and (3-3) we obtain the equation:

$$\frac{\partial n(\bar{x})}{\partial t} - \mathcal{D} n(\bar{x}) = \beta(\bar{x}). \tag{3-5}$$

We now seek a solution to the differential equation:

$$\mathcal{O} n(\bar{x}) \equiv \left(\frac{\partial}{\partial t} - \mathcal{D} \right) n(\bar{x}) = \beta(\bar{x}). \tag{3-6}$$

A Green's function solution $G(\bar{x})$ to such a differential equation is defined by the statement:

$$\text{If} \qquad \mathcal{O}n(\bar{x}) = \beta(\bar{x}) \ , \tag{3-7}$$

$$\text{and} \qquad \mathcal{O}G(x) = \delta(\bar{x}) \ , \tag{3-8}$$

$$\text{then} \qquad n(\bar{x}) = \int_{-\infty}^{\infty} G(\bar{x}-\bar{x}_o)\beta(\bar{x}_o)d\bar{x}_o \ . \tag{3-9}$$

We assert that the Green's function $G(\bar{x})$ of the operator $\mathcal{O} = \left(\frac{\partial}{\partial t} - \mathcal{D} \right)$ is given by:

$$G(\bar{x}) = F(\bar{x})\Theta(t) = \left[(4\pi D_L t)(4\pi D_T t)^2\right]^{-\frac{1}{2}} \exp\left[- \alpha t - \frac{x^2+y^2}{4D_T t} - \frac{(z-v_d t)^2}{4D_L t}\right]\Theta(t) \tag{3-10}$$

where $\Theta(t)$ is the step function defined as

$$\Theta(t) = \begin{cases} 1 & t > 0 \\ 0 & t \leq 0 \end{cases} \tag{3-11}$$

To show that Equation (3-10) is indeed the Green's function of the operator $\mathcal{O}$ we must show that $G(\bar{x})$ obeys Equation (3-8). The δ-function has the properties that:

$$\delta(\bar{x}) = 0 \qquad \text{for } \bar{x} \neq 0 \ , \tag{3-12}$$

and

$$\int_{-\infty}^{\infty} \delta(\bar{x})d\bar{x} = 1. \tag{3-13}$$

Equation (3-8) can be written as:

$$\mathcal{O}G(\bar{x}) = \mathcal{O}[F(\bar{x})\Theta(t)] = \Theta(t)\mathcal{O}F(\bar{x}) + F(\bar{x})\mathcal{O}\Theta(t)$$

$$= \Theta(t)\mathcal{O}F(\bar{x}) + F(\bar{x})\delta(t) \tag{3-14}$$

By straightforward though somewhat tedious calculation we can show that $\mathcal{O}F(\bar{x}) = 0$ for $t \neq 0$.

Thus for $\bar{x} \neq 0$ we have $\mathcal{O}G(\bar{x}) = 0$. It is also straightforward to show, using integration by parts, that:

$$\int_{-\infty}^{\infty} \mathcal{O}G(\bar{x})\, d\bar{x} = 1 \ . \tag{3-15}$$

Thus $\mathcal{O}G(\bar{x})$ does obey properties (3-12) and 3-13) of the δ-function and Equation (3-10) is a Green's function for the operator $\mathcal{O}$.

By Equation (3-9), if we let the Θ function alter the limits of t_o integration, we have

$$n(\bar{x}) = \int_{-\infty}^{\infty} G(\bar{x}-\bar{x}_o)\beta(\bar{x}_o)\, d\bar{x}_o \tag{3-16}$$

$$= \int_{-\infty}^{t} dt_o \int_{-\infty}^{\infty} dx_o \int_{-\infty}^{\infty} dy_o \int_{-\infty}^{\infty} dz_o \, \frac{\beta(t_o,x_o,y_o,z_o)}{\left\{[4\pi D_T(t-t_o)]^2[4\pi D_L(t-t_o)]\right\}^{\frac{1}{2}}}$$

$$\times \left\{-\alpha(t-t_o) - \frac{(x-x_o)^2 + (y-y_o)^2}{4D_T(t-t_o)} - \frac{[(z-z_o)-v_d(t-t_o)]^2}{4D_L(t-t_o)}\right\}$$

Because of the cylindrical symmetry of the experimental apparatus it is appropriate to express $n(\bar{x})$ in cylindrical coordinates where:

$$x_o = r_o\cos\theta_o,\ y_o = r_o\sin\theta_o,\ x = r\cos\theta, \text{ and } y = r\sin\theta. \qquad (3\text{-}17)$$

Equation (3-16) can be written in terms of cylindrical coordinates

$$n(\bar{x}) = \int_{-\infty}^{t} dt_o \int_{0}^{\infty} r_o dr_o \int_{0}^{2\pi} d\theta_o \int_{-\infty}^{\infty} dz_o$$

$$\times \frac{\beta(t_o, r_o, \theta_o, z_o)}{\left\{[4\pi D_T(t-t_o)]^2[4\pi D_L(t-t_o)]\right\}^{\frac{1}{2}}} \qquad (3\text{-}18)$$

$$\times \exp\left\{-\alpha(t-t_o) - \frac{r^2+r_o^2-2rr_o\cos(\theta-\theta_o)}{4D_T(t-t_o)} - \frac{[(z-z_o)-v_d(t-t_o)]^2}{4D_L(t-t_o)}\right\}$$

The ion source admits ions into the drift region through a circular aperture of radius r_s centered on the z-axis. Ions are gated into the drift region in temporally short pulses and we use the location of the ion gate to define z = 0. If the source input of ions β is cylindrically symmetric, then the ion number density n will also be cylindrically symmetric. For the one ion solution the input function β describes source produced ions only. If the source density of ions

s is constant across the entrance aperture it is reasonable to assume a source term of the form

$$\beta(\bar{x}_o) = \beta(t_o, r_o, z_o) = s\delta(t_o)\delta(z_o)\Theta(r_s - r_o) \tag{3-19}$$

Equation (3-18) now is

$$n(\bar{x}) = s \int_{-\infty}^{t} dt_o \int_{0}^{\infty} r\, dr_o \int_{0}^{2\pi} d\theta_o \int_{-\infty}^{\infty} dz_o$$

$$\times \frac{\delta(t_o)\delta(z_o)\Theta(r_s - r_o)}{\left\{[4\pi D_T(t-t_o)]^2 [4\pi D_L(t-t_o)]\right\}^{\frac{1}{2}}}$$

$$\times \exp\left\{-\alpha(t-t_o) - \frac{r^2 + r_o^2 - 2rr_o\cos(\theta-\theta_o)}{4D_T(t-t_o)} - \frac{[(z-z_o) - v_d(t-t_o)]^2}{4D_L(t-t_o)}\right\}$$

$$= \frac{se^{-\alpha t} \exp\left[-\frac{(z-v_d t)^2}{4D_L t}\right]}{[(4\pi D_T t)^2 (4\pi D_L t)]^{\frac{1}{2}}} \int_0^{r_s} r_o dr_o \int_0^{2\pi} d\theta_o$$

$$\times \exp\left[-\frac{r^2 + r_o^2 - 2rr_o\cos(\theta-\theta_o)}{4D_T t}\right] \tag{3-20}$$

Since $n(\bar{x})$ is radially symmetric we can define any particular direction as $\theta = 0$; thus we replace $\cos(\theta-\theta_o)$ with $\cos(\theta_o)$. Now, n depends only on r, z, and t.

The modified Bessel function of the first kind and zeroth order [21]

has an integral representation and power series expansion given by

$$I_o(\eta) = \frac{1}{\pi}\int_o^{\pi} d\theta e^{\pm\eta\cos\theta} = \sum_{m=0}^{\infty} \frac{(\eta/2)^{2m}}{(m!)^2} \qquad (3\text{-}21)$$

Thus from Equations (3-20) and (3-21)

$$\int_o^{2\pi} d\theta_o \, e^{\frac{2rr_o\cos\theta_o}{4D_T t}} = 2\pi \sum_{m=0}^{\infty} \frac{\left(\frac{rr_o}{4D_T t}\right)^{2m}}{(m!)^2} \qquad (3\text{-}22)$$

Combining (3-20) and (3-21)

$$n(r,z,t) = \frac{2\pi s\, e^{-\alpha t}\exp\left[-\frac{(z-v_d)^2}{4D_L t}\right]}{[(4\pi D_T)^2(4\pi D_L t)]^{\frac{1}{2}}} \exp\left(-\frac{r^2}{4D_T t}\right) \qquad (3\text{-}23)$$

$$\times \int_o^{r_s} r_o dr_o \exp\left(-\frac{r_o^2}{4D_T t}\right) \sum_{m=0}^{\infty} \frac{\left(\frac{rr_o}{4D_T t}\right)^{2m}}{(m!)^2}$$

If we let

$$\xi = \frac{r_o^2}{4D_T t}, \quad a = \frac{r_s^2}{4D_T t}, \quad \text{and} \quad b = \frac{r^2}{4D_T t}$$

we can write

$$\int_o^{r_s} r_o dr_o \exp\left(-\frac{r_o^2}{4D_T t}\right) \sum_{m=0}^{\infty} \frac{\left(\frac{rr_o}{4D_T t}\right)^{2m}}{(m!)^2} \qquad (3\text{-}24)$$

$$= 2D_T t \sum_{m=0}^{\infty} \frac{b^m}{(m!)^2} \int_0^a \xi^m e^{-\xi} d\xi$$

The integral can be evaluated by integration by parts m times, and

$$\int_0^a \xi^m e^{-\xi} d\xi = m! \left(1 - e^{-a} \sum_{k=0}^{\infty} \frac{a^k}{k!}\right) \tag{3-25}$$

Combining Equations (3-23), (3-24), and (3-25)

$$n(r,z,t) = \frac{se^{-\alpha t} \exp\left[-\frac{(z-v_d t)^2}{4D_T t}\right]}{(4\pi D_L t)^{\frac{1}{2}}} \left(1 - \sum_{m=0}^{\infty} \frac{b^m}{m!} \sum_{k=0}^{m} \frac{a^k}{k!} e^{-a} e^{-b}\right) \tag{3-26}$$

All the radial and D_T dependence is contained in the term

$$\rho(a,b) = \left(1 - \sum_{m=0}^{\infty} \frac{b^m}{m!} \sum_{k=0}^{m} \frac{a^k}{k!} e^{-a} e^{-b}\right) \tag{3-27}$$

The double series can be expanded and terms recollected in a different order to obtain (see Appendix IV-B)

$$\rho(a,b) = \left(\sum_{m=0}^{\infty} \frac{a^{m+1}}{(m+1)!} \sum_{k=0}^{m} \frac{b^k}{k!}\right) e^{-a} e^{-b} \tag{3-28}$$

Since a and b depend on D_T, t, r, and r_s, we write $\rho(a,b) = \rho(D_T, t, r, r_s)$.

Thus

$$n(r,z,t) = \frac{se^{-\alpha t}}{(4\pi D_L t)^{\frac{1}{2}}} \exp\left[-\frac{(z-v_d t)^2}{4D_L t}\right] \rho(D_T,t,r,r_s) \qquad (3\text{-}29)$$

$$= \frac{se^{-\alpha t}}{(4\pi D_L t)^{\frac{1}{2}}} \exp\left[-\frac{(z-v_d t)^2}{4D_L t}\right]$$

$$\times \left(\sum_{m=0}^{\infty} \frac{\left(\frac{r_s^2}{4D_T t}\right)^{m+1}}{(m+1)!} \sum_{k=0}^{m} \frac{\left(\frac{r^2}{4D_T t}\right)^k}{k!} \right) \exp\left(-\frac{r_s^2+r^2}{4D_T t}\right)$$

It should be noted that D_T and t only occur in the combination $4D_T t$ indicating that all ionic species will have the same radial dependence as a function of $4D_T t$.

Although to date $\rho(a,b)$ has not been identified in terms of known functions there are several limiting cases of interest which can be simply expressed.

On-Axis Measurements

In the present experimental apparatus the ions are sampled through an exit aperture of small area which is located on the z-axis. Taking the limit of ρ as $r \to 0$, i.e., $b \to 0$, we obtain

$$\lim_{r \to 0} \rho(D_T,t,r,r_s) = 1 - \exp\left(-\frac{r_s^2}{4D_T t}\right) \qquad (3\text{-}30)$$

This is most easily seen using Equation (3-27) and letting $b \to 0$. For on-axis measurements we obtain

$$n(z,t) = \frac{se^{-\alpha t}}{(4\pi D_L t)^{\frac{1}{2}}} \exp\left[-\frac{(z-v_d t)^2}{4D_L t}\right]\left[1 - \exp\left(-\frac{r_s^2}{4D_T t}\right)\right] \quad (3\text{-}31)$$

Two other limiting cases of possible interest are the point source and the infinite plane source solutions.

Point Source

If we let $d = 2\pi r_s^2 s$ be the constant number of ions admitted into the drift region we obtain the point source solution by taking the limit of $r_s \to 0$ of equation (3-29).

$$\lim_{r_s \to 0} n(r,z,t) = \frac{de^{-\alpha t}}{(4\pi D_L t)^{\frac{1}{2}}} \exp\left[-\frac{(z-v_d t)^2}{4D_L t}\right] \quad (3\text{-}32)$$

$$\times \lim_{r_s \to 0} \frac{1}{\pi r_s^2} \rho(D_T,t,r,r_s)$$

Using L'Hospital's rule, it is easy to show that

$$\lim_{r_s \to 0} \frac{1}{\pi r_s^2} \rho(D_T,t,r,r_s) = \frac{e^{-r^2/4D_T t}}{4\pi D_T t} \quad (3\text{-}33)$$

The point source solution is

$$n(r,z,t) = \frac{d\, e^{-\alpha t}}{[(4\pi D_T t)^2 (4\pi D_L t)]^{\frac{1}{2}}} \exp\left[-\frac{(z-v_d t)^2}{4D_L t} - \frac{r^2}{4D_T t}\right] \quad (3\text{-}34)$$

Indeed now $\beta(\bar{x}) = d\delta(\bar{x})$ so $n(\bar{x}) = dG(\bar{x})$.

Infinite Plane Source

The infinite plane source solution is obtained by holding the

source density s constant and taking the limit of $n(r,z,t)$ as $r_s \to \infty$.

$$\lim_{r_s \to \infty} n(r,z,t) = \frac{s\, e^{-\alpha t}}{(4\pi D_L t)^{\frac{1}{2}}} \exp\left[- \frac{(z-v_d t)^2}{4 D_L t} \right] \times \lim_{r_s \to \infty} \rho(D_T,t,r,r_s) \quad (3\text{-}35)$$

and

$$\lim_{r_s \to 0} \rho(D_T,t,r,r_s) = 1 \quad (3\text{-}36)$$

The infinite plane source solution is

$$n(z,t) = \frac{s\, e^{-\alpha t}}{(4\pi D_L t)^{\frac{1}{2}}} \exp\left[- \frac{(z-v_d t)^2}{4 D_L t} \right] \quad (3\text{-}37)$$

Note that as would be expected there is no radial or D_T dependence for a uniform source of infinite extent and the problem reduces to one space dimension.

Fore-back Analysis

We now consider ions which in addition to undergoing depleting reactions may have source terms from other ionic species. Specifically consider the reaction scheme previously mentioned

$$A \underset{\alpha_{AB}}{\overset{\alpha_{BA}}{\rightleftharpoons}} B$$

The transport equations describing two species of ions in drift motion that react to produce each other are

$$\frac{\partial n_A}{\partial t} - \wp_A n_A = \beta_A + \alpha_{AB} n_B \quad (3\text{-}38)$$

$$\frac{\partial n_B}{\partial t} - \mathcal{L}_B n_B = \beta_B + \alpha_{BA} n_A \tag{3-39}$$

where in analogy with Equation (3-4) $\mathcal{L}_i$ is given by

$$\mathcal{L}_i = D_{Ti}\left(\frac{\partial^2}{\partial x^2} + \frac{\partial^2}{\partial y^2}\right) + D_{Li}\frac{\partial^2}{\partial z^2} - v_{di}\frac{\partial}{\partial z} - \alpha_i \tag{3-40}$$

We will solve the coupled differential Equations (3-38) and (3-39) in steps. First we consider a single ionic species that is sourse-produced which reacts with the drift gas to produce a second ionic species, which then in turn reacts with the gas to produce a third species, etc.

As we have already shown the source-produced species obeys the differential equation:

$$\frac{\partial n_1(\bar{x}_1)}{\partial t} - \mathcal{L}_1 n_1(\bar{x}_1) = \beta_1(\bar{x}_1) \tag{3-41}$$

and has a solution:

$$n_1(\bar{x}_1) = \int_{-\infty}^{\infty} d\bar{x}_o \; G_1(\bar{x}_1 - \bar{x}_o)\beta_1(\bar{x}_o) \tag{3-42}$$

where we have now subscripted the Green's function G_i to correspond to the operator $(\partial/\partial t - \mathcal{L}_i)$. The i^{th} ionic species which is produced by reaction from the $(i-1)^{th}$ ionic species obeys the differential equation

$$\frac{\partial n_i(\bar{x}_i)}{\partial t} - \mathcal{L}_i n_i(\bar{x}_i) = \alpha_{i,i-1} n_{i-1}(\bar{x}_i) \tag{3-43}$$

so that

$$n_i(\bar{x}_i) = \int_{-\infty}^{\infty} d\bar{x}_{i-1} G_i(\bar{x}_i - \bar{x}_{i-1}) \alpha_{i,i-1} n_{i-1}(\bar{x}_{i-1}) \tag{3-44}$$

Specifically, the second ionic species density is given by

$$n_2(\bar{x}_2) = \int_{-\infty}^{\infty} d\bar{x}_1 G_2(\bar{x}_2 - \bar{x}_1) \alpha_{2,1} \int_{-\infty}^{\infty} d\bar{x}_o G_1(\bar{x}_1 - \bar{x}_o) \beta_1(\bar{x}_o) \tag{3-45}$$

In general the i^{th} ionic species has solution (letting $\bar{x} = \bar{x}_i$)

$$n_i(\bar{x}) = \int_{-\infty}^{\infty} d\bar{x}_{i-1} G_i(\bar{x} - \bar{x}_{i-1}) \alpha_{i,i-1} \int_{-\infty}^{\infty} d\bar{x}_{i-2} G_{i-1}(\bar{x}_{i-1} - \bar{x}_{i-2}) \alpha_{i-1,i-2} \tag{3-46}$$

$$\cdots \int_{-\infty}^{\infty} d\bar{x}_1 G_2(\bar{x}_2 - \bar{x}_1) \alpha_{2,1} \int_{-\infty}^{\infty} d\bar{x}_o G_1(\bar{x}_1 - \bar{x}_o) \beta(\bar{x}_o)$$

The spatial integrations $\vec{x}_{i-1}$ to $\vec{x}_1$ are Gaussian convolutions of the form:

$$\int_{-\infty}^{\infty} \frac{e^{-\frac{(x-x_1)^2}{a^2}}}{\sqrt{\pi a^2}} \cdot \frac{e^{-\frac{(x_1-x_o)^2}{b^2}}}{\sqrt{\pi b^2}} dx_1 = \frac{e^{-\frac{(x-x_o)^2}{a^2+b^2}}}{\sqrt{\pi(a^2+b^2)}} \tag{3-47}$$

Performing these spatial integrations and changing the time limits of integration to reflect the effect of the Θ functions in the G's yields

$$n_i(\bar{x}) = \int_{t_o}^{t} dt_{i-1} \alpha_{i,i-1} \int_{t_o}^{t_{i-1}} dt_{i-2} \alpha_{i-1,i-2} \cdots \int_{t_o}^{t_2} dt_1 \alpha_{2,1} \tag{3-48}$$

$$\times \int_{-\infty}^{t_1} dt_o \int_{-\infty}^{\infty} dx_o \int_{-\infty}^{\infty} dy_o \int_{-\infty}^{\infty} dz_o \frac{\exp\left[-\gamma_i - \frac{(z-r_{di})^2}{r_{Li}^2} - \frac{x^2+y^2}{r_{Ti}^2}\right]}{\left[(\pi r_{Ti}^2)^2 (\pi r_{Li}^2)\right]^{\frac{1}{2}}} \beta(\bar{x}_o)$$

Where

$$\gamma_i = \sum_{j=1}^{i} \alpha_j (t_j - t_{j-1}) \tag{3-49a}$$

$$r_{di} = \sum_{j=1}^{i} v_{dj} (t_j - t_{j-1}) \tag{3-49b}$$

$$r_{Li}^2 = \sum_{j=1}^{i} 4D_{Lj} (t_j - t_{j-1}) \tag{3-49c}$$

$$r_{Ti}^2 = \sum_{j=1}^{i} 4D_{Tj} (t_j - t_{j-1}) \tag{3-49d}$$

and $t_i = t$. Equations (3-49) have a simple physical interpretation. r_{Ti} is the average distance that the i^{th} ionic species has spread out due to transverse diffusion of itself and the i-1 other ionic species in its history. r_{Li} is the corresponding spread due to longitudinal diffusion. r_{di} is the average distance the i^{th} ionic species has drifted due to the characteristic drift velocity of the i^{th} ionic species and the (i-1) other ionic species in its hostory. γ_i is a measure of the survival probability of the i^{th} species. More precisely, r_{di} is the first moment of the i^{th} species. r_{Ti} and r_{Li} are the second moments of the i^{th} species in the transverse and longitudinal directions

respectively. These moments are a function not only of the transport coefficients of the i^{th} ionic species, but of all the ionic species in its past history.

If we assume $\beta(\bar{x}_o)$ has the familiar form

$$\beta(\bar{x}_o) = s\Theta(r_s - r_o)\ \delta(z_o)\ \delta(t_o)$$

we can do the integrations over $\bar{x}_o$ and obtain the equation

$$n_i(r,z,t) = s \prod_{j=1}^{i-1} \left(\alpha_{j+1,j} \int_o^{t_{j+1}} dt_j \right) \frac{\exp\left[-\gamma_i - \frac{(z-r_{di})^2}{r_{Li}^2}\right]}{(\pi r_{Li}^2)^{\frac{1}{2}}} \tag{3-50}$$

$$\times \left[1 - \sum_{m=0}^{\infty} \frac{\left(\frac{r^2}{r_{Ti}^2}\right)^m}{m!} \sum_{k=0}^{m} \frac{\left(\frac{r_s^2}{r_{Ti}^2}\right)^k}{k!} \exp\left(-\frac{r^2+r_s^2}{r_{Ti}^2}\right)\right]$$

The second term in brackets is recognized as Equation (3-27)

$$\rho(a,b) = \left(1 - \sum_{m=0}^{\infty} \frac{b^m}{m!} \sum_{k=0}^{m} \frac{a^k}{k!} e^{-a} e^{-b}\right) \tag{3-27}$$

where now $a = (r_s^2/r_{Ti}^2)$ and $b = (r^2/r_{Ti}^2)$. For on-axis measurements $r \to 0$, and $\rho(a,b) \to 1 - e^{-a}$ and

$$n_i(z,t) = s \prod_{j=1}^{i-1} (\alpha_{j+1,j} \int_o^{t_{j+1}} dt_j) \exp\left[-\gamma_i - \frac{(z-r_{di})^2}{r_{Li}^2}\right] \tag{3-51}$$

$$\times \left(\pi r_{Li}^2\right)^{-\frac{1}{2}} \left[1 - \exp\left(-\frac{r_s^2}{r_{Ti}^2}\right)\right]$$

Let us consider the specific situation of the fore-back reactions where the source-produced ions are all of species A. These ions then react with the gas to produce species B which may then react with the gas to become species A again, etc. Thus in the preceding analysis all ions labeled with odd subscripts are species A, and those with even subscripts are species B. Thus $n_{2i+1}(\bar{x})$ are ions of species A which have reacted with the gas and back again i times. Similarly n_{2i+2} are ions of species B which have reacted with the gas and back again i times. The total ionic number density of each species is obtained by summing all possible methods of obtaining each species. Thus

$$n_A(\bar{x}) = \sum_{i=0}^{\infty} n_{2i+1}(\bar{x}) \tag{3-52}$$

and

$$n_B(\bar{x}) = \sum_{i=0}^{\infty} n_{2i+2}(\bar{x}) \tag{3-53}$$

There now being only two ionic species involved we may rewrite Equations (3-49) in the form

$$\gamma = \alpha_A(t-u) + \alpha_B u \tag{3-54a}$$

$$r_d = v_{dA}(t-u) + v_{dB}u \tag{3-54b}$$

$$r_L^2 = 4D_{LA}(t-u) + 4D_{LB}u \tag{3-54c}$$

$$r_T^2 = 4D_{TA}(t-u) + 4D_{TB}u \tag{3-54d}$$

where u is the total time the ions spend as species B. If we define

$$u_i = (-1)^{i+1} \sum_{j=1}^{i-1} (-1)^j t_j \tag{3-55}$$

for i odd $u = u_i$ and for i even $u = (t-u_i)$. The t_j appear in Equation (3-51) only through the terms γ, r_d, r_L^2, and r_T^2. In each of these terms the t_j appear in the same linear combination, namely that specified by Equation (3-55). All except one of the time integrations in Equation (3-51) may be done through repeated application of the identity.

$$\int_0^\omega dy \int_0^y dx\, g(y-x)\, \frac{x^n}{n!}\, \frac{(y-x)^m}{m!} = \int_0^\omega du\, g(u)\, \frac{u^m}{m!}\, \frac{(\omega-u)^{n+1}}{(n+1)!} \tag{3-56}$$

where $u = y - x$.

This identity and a sample calculation of $n_i(\bar{x})$ for i = 5 are derived in Appendix IV. Performing these integrations we arrive at

$$n_{2i+1}(z,t) = s \int_0^t du \, \frac{(\alpha_{AB}\alpha_{BA})^i}{(\pi r_L^2)^{\frac{1}{2}}} \frac{u^{i-1}}{(i-1)!} \frac{(t-u)^i}{i!} \tag{3-57}$$

$$\times \exp\left[- \gamma - \frac{(z-r_d)^2}{r_L^2} \right]\left[1 - \exp\left(- \frac{r_s^2}{r_T^2}\right)\right]$$

$$n_{2i+2}(z,t) = s\,\alpha_{BA} \int_0^t du \, \frac{(\alpha_{AB}\alpha_{BA})^i}{(\pi r_L^2)^{\frac{1}{2}}} \frac{u^i}{i!} \frac{(t-u)^i}{i!} \tag{3-58}$$

$$\times \exp\left[- \gamma - \frac{(z-r_d)^2}{r_L^2} \right]\left[1 - \exp\left(- \frac{r_s^2}{r_T^2}\right)\right]$$

The solution for species A, the odd subscripts, is good for i = 1, 2, 3, ... The solution for species B, the even subscripts, is good for i = 0, 1, 2, ... The case of n_1 must be treated specially since it has no reaction-produced terms. We have solved for n_1 previously and obtained Equation (3-31). This solution can be included in the above Equation (3-57) by letting $u^{i-1}/(i-1)!$ be replaced by $\delta(u)$ for i = 0.

Combining Equations (3-52) and (3-57), and (3-53) and (3-58) we obtain:

$$n_A(z,t) = s \int_0^t du \left[\delta(u) + \sum_{i=1}^{\infty} (\alpha_{AB}\alpha_{BA})^i \frac{u^{i-1}}{(i-1)!} \frac{(t-u)^i}{i!}\right] \tag{3-59}$$

$$\times (\pi r_L^2)^{-\frac{1}{2}} \exp\left[-\gamma - \frac{(z-r_d)^2}{r_L^2}\right]\left[1 - \exp\left(-\frac{r_s^2}{r_T^2}\right)\right]$$

$$n_B(z,t) = s\,\alpha_{BA}\int_0^t du\left[\sum_{i=0}^{\infty}(\alpha_{AB}\alpha_{BA})^i\,\frac{u^i}{i!}\,\frac{(t-u)^i}{i!}\right] \qquad (3\text{-}60)$$

$$\times (\pi r_L^2)^{-\frac{1}{2}} \exp\left[-\gamma - \frac{(z-r_d)^2}{r_L^2}\right]\left[1 - \exp\left(-\frac{r_s^2}{r_T^2}\right)\right]$$

The delta function is treated here, and in the following, as lying entirely within the region of integration.

We define

$$\eta = [4\,\alpha_{AB}\alpha_{BA}\,u(t-u)]^{\frac{1}{2}} \qquad (3\text{-}61)$$

The zero and first order modified Bessel functions of the first kind are

$$I_o(\eta) = \sum_{i=0}^{\infty}\frac{(\eta/2)^{2i}}{(i!)^2} \qquad (3\text{-}62)$$

$$I_1(\eta) = \sum_{i=0}^{\infty}\frac{(\eta/2)^{2i+1}}{i!(i+1)!} \qquad (3\text{-}63)$$

The infinite sums in Equations (3-59) and (3-60) may be expressed in terms of the modified Bessel functions and

$$n_A(z,t) = s \int_o^t du \left[\delta(u) + \alpha_{AB}\alpha_{BA}(t-u)2I_1(\eta)/\eta \right] \qquad (3\text{-}64)$$

$$\times (\pi r_L^2)^{-\frac{1}{2}} \exp\left[- \gamma - \frac{(z-r_d)^2}{r_L^2} \right] \left[1 - \exp\left(- \frac{r_s^2}{r_T^2} \right) \right]$$

$$n_B(z,t) = s \int_o^t du \; \alpha_{BA} \; I_o(\eta) \qquad (3\text{-}65)$$

$$\times (\pi r_L^2)^{-\frac{1}{2}} \exp\left[- \gamma - \frac{(z-r_d)^2}{r_L^2} \right] \left[1 - \exp\left(- \frac{r_s^2}{r_T^2} \right) \right]$$

If we now consider the complimentary case of only species B being created in the source, the solutions for n_A and n_B may be obtained immediately from Equations (3-64) and (3-65) by exchanging A and B subscripts and exchanging u and (t-u). The complete solution to the fore-back reaction where both ionic species are created in the source is obtained by adding these two solutions. We now let s be the total source ion number density of both species and f_k be the fraction of source-produced ions which are species k, so that $f_A + f_B = 1$. The complete solution to Equations (3-38) and (3-39) is

$$n_A(z,t) = s \int_o^t du \left\{ f_A \left[\delta(u) + \alpha_{AB}\alpha_{BA}(t-u)2I_1(\eta)/\eta \right] \right. \qquad (3\text{-}66)$$

$$+ f_B\alpha_{AB}I_o(\eta) \Big\} (\pi r_L^2)^{-\frac{1}{2}} \exp\left[- \gamma - \frac{(z-r_d)^2}{r_L^2} \right]$$

$$\times \left[1 - \exp\left(- \frac{r_s^2}{r_T^2} \right) \right]$$

$$n_B(z,t) = s \int_o^t du \left\{ f_B[\delta(t-u) + \alpha_{AB}\alpha_{BA}\, u\, 2I_1(\eta)/\eta] \right. \qquad (3\text{-}67)$$

$$\left. + f_A\alpha_{BA}I_o(\eta) \right\} (\pi r_L^2)^{-\frac{1}{2}} \exp\left[- \gamma - \frac{(z-r_d)^2}{r_L^2} \right]$$

$$\times \left[1 - \exp\left(- \frac{r_s^2}{r_T^2} \right) \right]$$

At this point several things should be emphasized about the derivations of these equations. First these equations are strictly true only for an unbounded drift region because we did not impose any boundary conditions on these solutions.

Second the assumed form of a source term which involves δ-functions may seem somewhat artificial. Particularly disturbing may be the application of Fick's Law of Diffusion

$$\vec{j} = - D \vec{\nabla} n \qquad (3\text{-}68)$$

to a term involving a spatial δ-function and Θ-function ion density since a step change in the ion number density yields an infinite current. This concern will be shown to be unjustified by the following arguments. Let us instead take for the source term a Gaussian distribution in the r and z directions. We specify $\beta(\bar{x}_o)$ as

$$\beta(\bar{x}_o) = (\pi^3 r_s^4 z_s^2)^{-\frac{1}{2}} \delta(t_o) \exp\left(-\frac{r_o^2}{r_s^2} - \frac{z_o^2}{z_s^2}\right) \tag{3-69}$$

and maintain the radial symmetry of the source. $\beta(\bar{x}_o)$ is normalized such that

$$\int_{-\infty}^{\infty} \beta(\bar{x}_o) d\bar{x}_o = 1 \tag{3-70}$$

Now, from Equation (3-16) we have

$$n(\bar{x}) = \int_{-\infty}^{\infty} G(\bar{x}-\bar{x}_o)\beta(\bar{x}_o) d\bar{x}_o \tag{3-71}$$

$$= s \int_{-\infty}^{\infty} dx_o \int_{-\infty}^{\infty} dy_o \int_{-\infty}^{\infty} dz_o \; e^{-\alpha t} \left(\frac{\exp\left[-\frac{(z-z_o-v_d t)^2}{4D_L t}\right]}{\sqrt{4\pi D_L t}} \frac{\exp\left(-\frac{z_o^2}{z_s^2}\right)}{\sqrt{\pi z_s^2}} \right)$$

$$\times \left(\frac{\exp\left(-\frac{(x-x_o)^2}{4D_T t}\right)}{\sqrt{4\pi D_T t}} \frac{\exp\left(-\frac{x_o^2}{r_s^2}\right)}{\sqrt{\pi r_s^2}} \right) \left(\frac{\exp\left(-\frac{(y-y_o)^2}{4D_T t}\right)}{\sqrt{4\pi D_T t}} \frac{\exp\left(-\frac{y_o^2}{r_s^2}\right)}{\sqrt{\pi r_s^2}} \right)$$

$$= s\, e^{-\alpha t} \frac{\exp\left[-\frac{(z-v_d t)^2}{4D_L t + z_s^2}\right]}{\sqrt{\pi(4D_L t + z_s^2)}} \frac{\exp\left(-\frac{r^2}{4D_T t + r_s^2}\right)}{[\pi(4D_T t + r_s^2)]}$$

We recognize this last step as a Gaussian Convolution. The effect of a finite distribtuion source term is seen only to add an "initial diffusion" term to both the D_L and D_T terms. This may immediately be extended to the case of fore-back reactions where Equations (3-49) and (3-54) now become:

$$r_L^2 = 4D_{LA}(t-u) + 4D_{LB}u + z_s^2 \qquad (3\text{-}72a)$$

$$r_T^2 = 4D_{TA}(t-u) + 4D_{TB}u + r_s^2 \qquad (3\text{-}72b)$$

We can make the Gaussian distribution as "sharp" as we want by letting z_s and/or $r_s \rightarrow 0$ and from Equations (3-72) we see there is no problem of the ion density becoming discontinuous.

Experimental Observables

It would be desirable to be able to sample the entire ion swarm at one time. The drift velocity and diffusion coefficients could then be determined from the first and second spatial moments of the observed

ion number density. However, this is not possible in the present experimental apparatus. What is observed is the flux of ions exiting the drift region through an aperture of area a located on the z-axis. This flux of ions is given by

$$\Phi(z,t) = a j_z(z,t) \tag{3-73}$$

where $j_z(z,t)$ is the ionic current in the z-direction for a specific drift distance z, drift time t, and on the z-axis, i.e., r = 0. We can solve for the ionic current from Equations (3-2), (3-67) and (3-68). For the case of the fore-back reactions we obtain for the separate ionic fluxes

$$\Phi_A(z,t) = as \int_o^t \frac{du}{(\pi r_L^2)^{\frac{1}{2}}} \left\{ f_A \left[\delta(u) + \alpha_{AB}\alpha_{BA}(t-u) \frac{2I_1(\eta)}{\eta} \right] \right. \tag{3-74}$$

$$\left. + f_B \alpha_{AB} I_o(\eta) \right\} \left\{ \left[2D_{LA} \frac{(z-r_d)}{r_L^2} \right] + v_{dA} \right\}$$

$$\times \exp\left[- \gamma - \frac{(z-r_d)^2}{r_L^2} \right] \left[1 - \exp\left(- \frac{r_s^2}{r_T^2} \right) \right]$$

$$\Phi_B(z,t) = as \int_o^t \frac{du}{(\pi r_L^2)^{\frac{1}{2}}} \left\{ f_B \left[\delta(t-u) + \alpha_{BA}\alpha_{AB} u \frac{2I_1(\eta)}{\eta} \right] \right. \tag{3-75}$$

$$+ f_A \alpha_{BA} I_o(\eta) \Big) \left\{ \left[2D_{LB} \frac{(z-r_d)}{r_L^2} \right] + v_{dB} \right\}$$

$$\times \exp \left[- \gamma - \frac{(z-r_d)^2}{r_L^2} \right] \left[1 - \exp \left(- \frac{r_s^2}{r_T^2} \right) \right]$$

Detected ions are sorted according to their time of arrival. The instant of admission of ions into the drift region is defined as time t = 0. From many identical source bursts of ions we build up an arrival time spectrum. Each point on the spectrum consists of the number of ions detected for various times of arrival. Arrival time spectra are taken as a function of drift distance, gas pressure, electric field intensity, source conditions, and ionic mass. Details of this procedure have been previously discussed in Chapter I. From these arrival time spectra we must obtain the transport coefficients and reaction rates of the ion-gas combination. When possible the experimental conditions are varied so to emphasize that part of the arrival time spectrum which depends most strongly on the coefficient being measured.

Drift Velocity

When an ionic species is source produced and undergoes only depleting reactions the on-axis number density is given by Equation (3-31) and the ionic flux is

$$\Phi(z,t) = \frac{as}{(4\pi D_L t)^{\frac{1}{2}}} \left(v_d + \frac{z}{t} \right) \exp \left[-\alpha t - \frac{(z-v_d t)^2}{4D_L t} \right] \qquad (3\text{-}76)$$

$$\times \left[1 - \exp\left(- \frac{r_s^2}{4D_T t} \right) \right]$$

When measuring drift velocities it is desirable to have an arrival time spectrum that is not distorted by reactions. In practice reactions other than depleting reactions can usually be made negligible by the appropriate choice of source, gas pressure and drift field conditions.

The average arrival time of the detected ions is

$$\bar{t} = \frac{\int_0^t t\Phi(z,t)dt}{\int_0^\infty \Phi(z,t)\,dt} \qquad (3\text{-}77)$$

Moseley [22] has calculated $\bar{t}$ for the cases of the point source and infinite plane source to first order. The point source solution is

$$\bar{t} = \frac{z}{v_d}\left(1 - \frac{D_L}{v_d z} - \frac{2\alpha D_L}{v_d^2}\right) \qquad (3\text{-}78)$$

and the infinite plane source solution is

$$\bar{t} = \frac{z}{v_d}\left(1 + \frac{D_L}{v_d z} - \frac{2\alpha D_L}{v_d^2}\right) \qquad (3\text{-}79)$$

To zeroth order the average arrival time is $\bar{t} = z/v_d$. The first order correction terms can be understood on a physical basis. In both cases the depletion frequency α causes $\bar{t}$ to be weighted toward earlier times.

Those ions which have spent a longer time in the drift region due to being spread by diffusion will have undergone more reactions and thus be depleted. This term should be proportional to D_L which determines how much the ions have spread along z, and proportional to α which determines how fast the ions are depleted. This is the origin of the last term in Equations (3-78) and (3-79). In the case of the point source those ions which arrive later have been spread radially more than those which arrived earlier. The transverse diffusion causes these ions to be spread away from the axis and thus acts as a depletion term. This is the origin of the second term in Equation (3-78). This also weights $\bar{t}$ to earlier times.

For an infinite plane source there is no effect of transverse diffusion. There is thus no depletion of ions on axis due to the ion swarm being spread radially. Those ions which arrive later have, however, diffused longitudinally more than those which arrived earlier. Thus longitudinal diffusion weights the arrival time toward later times. This is the origin of the second term in Equation (3-79).

In the present experimental apparatus the source is of finite radius r_s. In this case the first order correction of $\bar{t}$ due to diffusion would be anticipated to be between the limits of those for the point source and the infinite plane source.

In practice we calculate the experimental drift velocity, v_d', by calculating $\bar{t}$ for two successive drift lengths and computing

$$v_d' = \frac{z_i - z_j}{\bar{t}_i - \bar{t}_j} \qquad (3\text{-}80)$$

Applying this formula to either Equations (3-78) or (3-79) yields:

$$v_d' = \frac{v_d}{\left(1 - \frac{2\alpha D_L}{v_d^2}\right)} \simeq v_d \left(1 + \frac{2\alpha D_L}{v_d^2}\right) \qquad (3\text{-}81)$$

This "differencing" technique has several advantages. The time taken to sample and detect an arriving ion swarm, the analysis time, is unknown and depends upon many factors such as pressure, ionic mass, etc. This time will, however, remain constant between successive positions of the source provided everything else remains constant. By "differencing", this unknown analysis time is removed. In addition most end effects are also removed.

Equation (3-81) indicates that all effects due to diffusion have been removed. This is not strictly true since Equations (3-78) and (3-79) were only first order approximations. Moseley [22] has investigated the remaining diffusion error for N_2^+ ions in N_2 by constructing arrival time spectra from Equation (3-76) for several drift distances. From these constructed spectra the "experimental" and actual drift velocities were computed and compared. This analysis showed Equation (3-81) to realistically express the error of the experimental drift velocity and the remaining diffusion error to be well below the statistical scatter of the experimental results. By appropriately choosing pressures to minimize the term αD_L the best agreement is obtained. If $\alpha = 0$ the reaction term is removed completely. Theory predicts that the drift velocity v_d, and ND_L are dependent on E and N only through the combination E/N. If a reaction is two-body then

$\alpha = kN$ and the correction term in Equation (3-81) is $2kND_L/v_d^2$. Since ND_L is constant for a specific E/N, the correction term is independent of pressure. If the reaction is three-body then $\alpha = kN^2$ and the correction term in Equation (3-81) is $2kN^2D_L/v_d^2$. Here the correction term is directly proportional to the pressure for a fixed E/N. Many reactions are three-body. Among reactions of this type are:

$$H^+ + 2H_2 \rightarrow H_3^+ + H_2 \qquad (3\text{-}82a)$$

$$N_2^+ + 2N_2 \rightarrow N_4^+ + N_2 \qquad (3\text{-}82b)$$

$$CO^+ + 2CO \rightarrow CO^+ \cdot CO + CO \qquad (3\text{-}82c)$$

$$K^+ + 2Ar \rightarrow K^+ \cdot Ar + Ar \qquad (3\text{-}82d)$$

Reactions like Equations (3-82c) and (3-82d) are called clustering reactions. When the predominant force binding an ion-molecule is the $1/r^5$ polarization force, the combination is called an ionic cluster or simply a cluster. [23] As can be seen by Equation (3-82d), clustering can occur between unlikely combinations. Clustering has been observed between K^+ and N_2, CO_2, NO, CO, O_2 Ar, Ne, He, and D_2 by this laboratory [24] at pressures as low as 100 microns. Clustering is mentioned here to demonstrate that when measuring drift velocities great care must be taken to ensure that all reactions are understood and accounted for, even the unexpected.

The magnitude of this correction should be calculated for each

ion-gas combination. Some authors [25] have reported a measured pressure dependence of the mobility for a fixed E/N. Clustering is one possible explanation for this dependence. [26]

Longitudinal Diffusion

The shape of an arrival time spectrum of an ion undergoing only depleting reactions is a skewed gaussian. The effect of both transverse diffusion D_T and depleting reactions α is to cause the arrival time spectrum to have a steeper rise at earlier times. This skewing prevents us from obtaining diffusion coefficients from simply calculating the second moment of $\Phi(z,t)$. The width of $\Phi(z,t)$ is, however, a measure of longitudinal diffusion. To obtain longitudinal diffusion coefficients from arrival time spectra a curve fitting scheme is used. The detailed arrival time spectrum is fitted by the theoretical expression (3-76) for $\Phi(z,t)$. In Equation (3-76) the source intensity s, the transverse diffusion coefficient D_T, the reaction frequency α, and the longitudinal diffusion coefficient D_L are in general unknown. Moseley [27] has shown that while D_T and α drastically affect the intensity of $\Phi(z,t)$, the overall shape of the arrival time spectrum is relatively insensitive to changes in D_T and α. The time dependence of D_T and α is sufficiently weak to be essentially constant over the time width of an arrival time spectrum. The time dependence of the term $e^{-\alpha t}$ is pressure dependent. During drift velocity and longitudinal diffusion coefficient measurements a pressure is used that makes α small. Since ND_L is constant for a fixed E/N, operating at lower pressures thus makes D_L larger and the arrival time spectrum wider. For a specific channel width, a wide spectrum has more data points and statistically

gives a better fit.

$\Phi(z,t)$ depends on D_T through the factor

$$\left[1 - \exp\left(-\frac{r_s^2}{4D_T t}\right)\right] \qquad (3\text{-}83)$$

Equation (3-83) depends inversely on t. By choosing long drift distances the time of arrival of ions is made large and (3-83) varies little over the time width of an arrival time spectrum.

When fitting $\Phi(z,t)$ to the experimental arrival time spectrum, we set D_T equal to the Einstein or Wannier values and α equal to zero. The heights of the experimental spectrum and $\Phi(z,t)$ are set equal. This eliminates the dependence of $\Phi(z,t)$ on the absolute source intensity s. The value of D_L is obtained by varying D_L in $\Phi(z,t)$ to obtain the best least squares fit between $\Phi(z,t)$ and the experimental data. A detailed description of the actual fitting procedure has been given by Schummers [28] and will not be repeated here.

Reactions Rates

Reactions rates can be determined by two different methods. The first method measures the attenuation of the parent ionic species as a function of drift distance. This procedure is useful when the reaction occurs in only one direction. Reactions of this type may be characterized by:

$$A^+ + B \rightarrow C^+ + D \qquad (3\text{-}84)$$

where ion C^+ does not react or break up to form ion A^+. The total

ionic current detected for a specific drift distance is given by: [29]

$$I(z) = \int_0^\infty \Phi(z,t)\, dt \qquad (3\text{-}85)$$

$$= \frac{as \exp\left(\frac{zv_d}{2D_L}\right)}{4\sqrt{D_L}} \left\{ \left[2D_L^{\frac{1}{2}} + \frac{v_d}{\left(\alpha + \frac{v_d^2}{4D_L}\right)^{\frac{1}{2}}} \right] \exp\left[- \frac{z}{\sqrt{D_L}} \left(\frac{v_d^2}{4D_L} + \alpha \right)^{\frac{1}{2}} \right] \right.$$

$$- \left[\frac{z}{(z^2/4D_L + r_s^2/4D_T)^{\frac{1}{2}}} + \frac{v_d}{\left(\alpha + \frac{v_d^2}{4D_L}\right)^{\frac{1}{2}}} \right]$$

$$\left. \times \exp\left[-2 \left(\frac{z^2}{4D_L} + \frac{r_s^2}{4D_T} \right)^{\frac{1}{2}} \left(\frac{v_d^2}{4D_L} + \alpha \right)^{\frac{1}{2}} \right] \right\}$$

This current can be fit by a least squares procedure with the experimentally measured currents for several drift distances. Since the absolute source intensity is not known one drift distance must be used to normalize the current. α is then varied to obtain a best fit. As previously mentioned the intensity depends strongly on both α and D_T. Usually D_T is not accurately known and must also be determined from either the Wannier or Einstein equations. [30] The dependence of $I(z)$ on α and D_T is separated by the pressure dependence of α and D_T. α is proportional to either N or N^2 depending on whether the reaction is two or three body. D_T on the other hand is proportional to $1/N$. By

use of I(z), D_T may then be determined at low pressures where reaction effects are minimized and α may be determined at higher pressures where reaction effects are accentuated and transverse diffusion is minimized. Miller [2,31] has used this "attenuation" method to determine the reaction rate of

$$H^+ + 2H_2 \rightarrow H_3^+ + H_2$$

The second method used to determine reaction rates is detailed fitting of the arrival time spectra. When forward-backward reactions occur the arrival time spectra of both ionic species must be analyzed. In the present cases of interest the reaction is only forward and reaction rates may be obtained from a detailed fit of only the product ion arrival time spectrum. Schummers [32] has discussed the procedure used in evaluating reaction rates in the case of fore-back reactions.

Under specific assumptions the analysis of the product ion arrival spectrum may be simplified. If we assume species B to be the product ion the arrival time spectrum is given by Equation (3-75). In the case the backward reaction does not occur, $\alpha_{AB} = 0$ and $\Phi_B(z,t)$ is specified by:

$$\Phi_B(z,t) = as \int_o^t \frac{du}{(\pi r_L^2)^{\frac{1}{2}}} \left\{ f_B\, \delta(t-u) + f_A\, \alpha_{BA} \right\} \qquad (3\text{-}86)$$

$$\times \left\{ \left[2D_{LB} \frac{(z-r_d)}{r_L^2} \right] + v_{dB} \right\} \exp \left[-\gamma - \frac{(z-r_d)^2}{r_L^2} \right]$$

$$\times \left[1 - \exp\left(-\frac{r_s^2}{r_T^2}\right)\right]$$

When the difference in distances the two ionic species have traveled in time t, $(v_{dA} - v_{dB})t$, is large compared to the square root of the sum of the diffusion areas $(4D_{LA}t + 4D_{LB}t)^{\frac{1}{2}}$ then

$$(v_{dA} - v_{dB})^2 t^2 \gg (4D_{LA}t + 4D_{LB}t) \geq [4D_{LA}(t-u) + 4D_{LB}u] = r_L^2 \quad (3\text{-}87)$$

and the approximation can be made that [33]

$$(\pi r_L^2)^{-\frac{1}{2}} \exp\left[-\frac{(z-r_d)^2}{r_L^2}\right] \simeq \frac{1}{|v_{dA}-v_{dB}|}\,\delta(u-u_1) \quad (3\text{-}88)$$

where
$$u_1 = \frac{v_{dA}t - z}{v_{dA}-v_{dB}} \quad (3\text{-}89)$$

and
$$u - u_1 = \frac{z-r_d}{v_{dA}-v_{dB}}\,. \quad (3\text{-}90)$$

Using this approximation in Equation (3-86) we have

$$\Phi_B(z,t) = as\left\{f_B\,\delta(t-u_1) + f_A\,\alpha_{BA}\right\}\frac{v_{dB}\,e^{-\gamma_1}}{v_{dA}-v_{dB}} \quad (3\text{-}91)$$

$$\times \left[1 - \exp\left(-\frac{r_s^2}{r_{T1}^2}\right)\right]$$

where $$r_{T1}^2 = 4D_{TA}(t-u_1) + 4D_{TB}u_1 \tag{3-92a}$$

and $$\gamma_1 = \alpha_A(t-u_1) + \alpha_B u_1 \tag{3-92b}$$

To determine reaction rates we examine that part of the spectrum which is completely reaction produced. We can set $f_B = 0$ in Equation (3-91) for this part of the spectrum. Taking the natural logarithm of $\Phi_B(z,t)$ and differentiating with respect to time yields

$$\frac{\partial \ln \Phi_B}{\partial t} = -\frac{\partial \gamma_1}{\partial t} + \frac{r_s^2 \left(\frac{4D_{TB}v_{dA} - 4D_{TA}v_{dB}}{v_{dA} - v_{dB}} \right)}{r_T^4 \left(1 - e^{-r_s^2/r_t^2}\right)} \tag{3-93}$$

When $D_{TA}/v_{dA} = D_{TB}/v_{dB}$ then the second term on the RHS of Equation (3-93) is equal to zero. This condition holds, for example, in the low field region where the Einstein relation is strictly true. Under conditions such that this assumption is true, Equation (3-93) reduces to

$$\frac{\partial \ln \Phi_B}{\partial t} = \frac{v_{dB}\alpha_A - v_{dA}\alpha_B}{v_{dA} - v_{dB}} \tag{3-94}$$

When species A reacts to produce only species B then $\alpha_A = \alpha_{BA}$, and when species B has no depleting reactions $\alpha_B = 0$. Under these conditions Equation (3-94) has the particularly simple form

$$\frac{\partial \ln \Phi_B}{\partial t} = \frac{\alpha_{BA} v_{dB}}{v_{dA} - v_{dB}} \qquad (3\text{-}95)$$

The assumptions used in deriving this simple form might seem so restrictive as to be of no practical importance but, this form does give good quantative agreement when species A and B have drift velocities that are appreciably different. Examples of this are H^+ and H_3^+, and O^- and O_2^-. In addition reaction rate measurements are made at sufficiently high pressures to make the terms r_L and r_T small. The other assumptions about the reactions, $\alpha_{AB} = 0$, $\alpha_B = 0$, $\alpha_{BA} = \alpha_B$ must be verified for the particular ion-molecule reaction under consideration. The extent to which all of these assumptions are legitimate may be checked by comparing reaction rates for different drift distances and pressures. When these assumptions are found to be unwarranted one can make other less restrictive approximations or fit the full expression of $\Phi_B(z,t)$ given by Equation (3-75) to the experimental data. A detailed description of how this is accomplished is given in Chapter VI.

CHAPTER IV

MOBILITIES

Mobility measurements refer to a single ionic species drifting in a known gas. These measurements are made at specific values of the experimental parameters E/N and T. Since ions may have electronically excited states which interact with the gas differently from the ground state it is also necessary to know to which electronic state a mobility refers.

Ion Production

The ion source is described in Chapter II. In this section the processes involved in the production of each ionic species will be discussed. Both hydrogen ions (H^+, H_3^+, H^-) and deuterium ions (D^+, D_3^+, D^-) are produced; however, since the corresponding processes are identical as we go from one isotope to the other, only hydrogen ions will be discussed.

Ions are created in the ionization region of the source by electron bombardment of the drift-tube gas. Ions will be designated as either primary or secondary. A primary ion is one produced in the source by electron bombardment. A secondary ion is one that is produced from another (primary or secondary) ionic species by reaction. Ions will also be classified as source-produced and reaction-produced. Here source-produced refers to ions originating only from the source no matter how they are formed in the source. Reaction-produced refers

to ions formed by reactions only in the drift region. Thus an ion which is produced in the source by reaction and then enters the drift region is a secondary ion and also a source-produced ion.

$\underline{H^+}$

H^+ ions are created via dissociative ionization of H_2 molecules by electron impact. The two principal processes involved are

$$e^- + H_2 \rightarrow H^+ + H + 2e^- \qquad (4\text{-}1)$$

and

$$e^- + H_2 \rightarrow H^+ + H^- + e^-. \qquad (4\text{-}2)$$

The first process (4-1) can occur at $\gtrsim$ 18.3 eV and the second process (4-2) requires $\gtrsim$ 17.6 eV. When H^+ ions are to be produced in the source, electron acceleration potentials of about 25 volts are used; thus both these processes can contribute to the source output of H^+ ions. It is also possible for H^+ ions to be produced at high E/N by

$$H_3^+ + H_2 \rightarrow H^+ + 2H_2. \qquad (4\text{-}3)$$

This effect would be apparent from the shape of the arrival time spectra. Albritton [34] has observed this process at an E/N > 110 Td. Our measurements do not extend to such high values of E/N, and this dissociation was not observed.

Since H^+ ions are simply protons there are no excited states to consider.

H_3^+

H_3^+ ions are secondary ions produced from H_2^+ in the source and from H^+ both in the source and in the drift region. The H_3^+ ions are therefore both source-produced and reaction-produced ions.

The H_2^+ ions are generated in the source by ionization of the H_2 gas molecules through the reaction

$$e^- + H_2 \rightarrow H_2^+ + 2e^- \quad . \tag{4-4}$$

This reaction requires $\gtrsim 15.4$ eV, the ionization energy of the H_2 molecule. The H_2^+ ions then react in the source to produce H_3^+ ions via

$$H_2^+ + H_2 \rightarrow H_3^+ + H \quad . \tag{4-5}$$

The rate coefficient for this reaction is very large ($k_H \simeq 2 \times 10^{-9}$ cm^3/sec),[35] and all H_2^+ ions are converted to H_3^+ ions within the first few collisions with the H_2 gas molecules. This reaction is so fast that H_2^+ ions cannot exist under steady state drift conditions in H_2 gas. By operating the apparatus at low pressures (< 5 microns) and at short drift distances (6.25 cm), we can observe H_2^+ ions; however, in this mode the apparatus operates as a gas analyzer and drift conditions do not exist. H_2^+ ions are not observed under drift conditions, and at normal operating pressures (> 50 microns) all H_2^+ ions are converted to H_3^+ before exiting the source. H_3^+ ions are also produced through the reaction

$$H^+ + 2H_2 \rightarrow H_3^+ + H_2 \ . \qquad (4\text{-}6)$$

with a rate coefficient $k \tilde{=} 3.05 \times 10^{-29} cm^6/sec$. This reaction can occur both in the source and in the drift region. In our experiments this reaction is much slower than reaction (4-5), and both H^+ and H_3^+ exist under drift conditions. The measruement of this reaction rate coefficient is one of the objectives of the present research and is discussed in detail in Chapter VI.

The possibility of stable electronically excited states for H_3^+ ions must be considered. Once the H_3^+ ion is formed there is insufficient energy in its drift motion (at $E/N < 100$ Td) to excite it to a higher electronic level from the ground state. Thus if H_3^+ exists in an excited state it must be created in this state when formed from H_2^+. This could occur in either of two ways. (1) The H_2^+ ion could be created in an excited state and form H_3^+ in an excited state in the reaction with H_2, or (2) the H_2^+ ion could have sufficient kinetic energy that in the reaction with the H_2 molecule H_3^+ is formed in an excited state. The first process is ruled out since H_2^+ has no stable excited states. [36] In either case no excited states of H_3^+ have been experimentally observed and theoretically no bound excited states have been predicted. [37] From the standpoint of mobility measurements, the best indication that there are no excited states is a well defined zero-field reduced mobility.

$\underline{H^-}$

H^- ions are produced in the source by dissociative attachment [38] via

$$e^- + H_2 \rightarrow H^- + H \qquad (4\text{-}7a)$$

and

$$e^- + H_2 \rightarrow H^- + H^*. \qquad (4\text{-}7b)$$

The threshold for (4-7a) is $\sim$ 6eV. Equation (4-7a) accounts for all H^- production below 13.6 eV. Above 13.6 eV, H^- ions are also produced by reaction (4-7b). At electron energies above $\sim$ 17.6 eV the reaction scheme (4-2)

$$e^- + H_2 \rightarrow H^+ + H^- + e^- , \qquad (4\text{-}2)$$

already discussed in the production of H^+ ions, contributes to the production of H^- ions. During most of the experimental runs electron acceleration potentials of $\sim$ 8 volts were used; thus all H^- production is from reaction (4-7a).

Again the possibility of excited states must be considered. The ground state of the H^- ion is $(1s)^2$. No excited states of H^- have been observed experimentally; however, the possibility of a bound excited state is predicted theoretically. The $(2p)^2\ ^3P$ level of H^- is predicted to be stable if L-S coupling is a good approximation. [39] The energy of this state is calculated to be 10.2 eV above the ground state of the

neutral H atom. The neutral H atom has an electron affinity of about 0.75 eV [40] and thus forms a stable H^- ion in the ground $(1s)^2$ state.

Other Hydrogen Ions

H_5^+. H_5^+ can be observed under drift conditions; however, its intensity is much lower than that of H^+ or H_3^+. The arrival time spectra of H_3^+ and H_5^+ show H_5^+ to be loosely bound and the reaction producing H_5^+ has been reported by Saporoschenko [13] to be three-body. Thus H_5^+ is created and destroyed through the reaction

$$H_3^+ + 2H_2 \rightleftarrows H_5 + H_2 \ . \qquad (4\text{-}8)$$

Because H_5^+ is so loosely bound it is difficult to separate the drift velocity of H_5^+ from its dependence on the drift velocity of H_3^+. [41] The H_5^+ ion has not been investigated in the present research.

H_2^-. The possibility of the existence of H_2^- under drift conditions has been investigated. H_2^- ions have been reported to have been detected experimentally. [42] Ions were produced in an electron bombardment source containing water and antimony vapor and analyzed in a mass spectrometer coupled to an electron multiplier. The mass 2 peak was attributed to H_2^- and not to D^- because of the relative amplitudes of the mass 1 and mass 2 peaks. It was also noted that the height of the mass 2 peak depended on the presence of the antimony vapor. Muschlitz [43] has also investigated the formation of negative ions in hydrogen, but he reported observing only H^- ions. Thus the existence of a stable H_2^- ion is debatable altogether, much less its existence under drift conditions. The theoretical structure of H_2^- has been

extensively investigated by Taylor [44] and it is predicted that any bound states of H_2^- are not stable over time periods compatable with drift measurements.

In hydrogen gas, ions with a mass of 2 were detected under drift conditions. The natural abundance of the deuterium isotope in hydrogen atoms is 0.015 percent or 150 ppm. Mass scans over the positive and negative ions were made and a ratio of ~ 1:1536 or ~ 650 ppm of mass 2 to mass 1 was detected for negative ions and a ratio of ~ 1:3840 or ~ 260 ppm of mass 2 to mass 1 was detected for positive ions. The mass 2 positive ion is D^+. The difference in these ratios from those of naturally appearing deuterium can easily be accounted for because of mass discrimination in the ion sampling and rf quadrupole. In addition, because of the low intensity of the mass 2 signal the experimental ratios are only very approximate. Because all the potentials of the experimental apparatus must be reversed for negative ions and the biasing is different on the rf quadrupole and channeltron, it is not unusual for the mass discrimination to be different between positive and negative ion mass scans. The change in the ratios, therefore, should not be construed as being evidence of the existence of H_2^-.

The mobility of the negative mass 2 ion has been measured. Theory predicts that the mobilities of ions should scale according to the inverse square root of the reduced mass of the ion-gas molecule pair. This scaling between H^- and the mass 2 ion should be strictly true if the mass 2 ion is in fact D^-, with the identical shell structure of H^-. However, if the mass 2 ion is H_2^-, its mobility would probably be greatly reduced by charge exchange with the H_2 gas molecules. The

measured mobility of H^- in H_2 is 43.0 $cm^2/V \cdot sec$. The mobility of D^- in H_2 should be ~ 35.1 $cm^2/V \cdot sec$ according to the reduced mass scaling between H^- and D^-. The measured mobility of the mass 2 ion is 36.6 $cm^2/V \cdot sec$. Because of the intensity of the mass 2 ion and consequently the short drift distances used in this measurement, the accuracy is probably no better than ± 6 percent. The measurement does, however, agree very well with that predicted for D^- in H_2. The mass 2 ion is therefore tentatively identified as D^-.

Impurity Ions

In mass scans of the positive hydrogen and deuterium ions the primary ions detected were H^+ and H_3^+ in H_2 and D^+ and D_3^+ in D_2. Also detected were H_2D^+ and H_5^+ in H_2 and D_2H^+ and D_5^+ in D_2. The hydrogen dual isotope impurity HD is present in both H_2 and D_2 gases and cannot be removed by the palladium-leak. The intensity of isotope ions is small and considered to be no source of error in the present measurements. Other impurity ions are detectable, namely H_3O^+ produced from water vapor; however the intensity is barely above the background noise level and the use of a refrigerated vapor bath was not considered necessary.

No negative ions other than H^- and D^- in H_2 were detected. No doubly charged negative ions have ever been observed in the gaseous phase.

Source Parameters

When measuring mobilities, it is desirable to have only one ionic species in the drift region. This prevents the arrival time

spectra from being distorted by reactions. Quite often this can be accomplished by adjusting the gas pressure and/or the source conditions.

Since the threshold energy for the production of H_3^+ (equations 4-4 and 4-5) is below that for H^+ (Equation 4-2), it is possible to produce exclusively H_3^+ ions in the source. This is accomplished simply by adjusting the filament bias, V_{acc}, and the collector potential, V_c, such that the electrons producing H_2^+ ions do not have sufficient energy to produce H^+ ions. Experimentally this is best accomplished with a low collector potential and a high filament bias.

When producing H^+ ions, it is not possible in the present source to prevent large quantities of H_3^+ ions from also being created. The best one can do is to optimize the ratio between H^+ and H_3^+. Experimentally it is found that the best procedure to do this is to keep the filament bias low ($\sim$ 0 volts) and the collector potential high ($\sim$ 30 volts). The control plate is biased, with a potential V_g, to prevent any electrons from escaping the filament enclosure. Periodically the control plate is pulsed with a large (30 volts) positive pulse. Because of the low filament bias, few electrons are emitted from the filament. When the control plate is pulsed, electrons are pulled from the filament and filament enclosure into the ionization region with energies of about 30 eV. Once in the ionization region the electrons are influenced primarily by the collector and are pulled into the collector by a positive bias, V_c. This procedure keeps the energy of the electrons at approximately 30 eV throughout their transit of the ionization region.

Since H^- is the only negative ion observed (other than minute

quantities of D^-), the source is adjusted for ease of operation instead of for best ion ratios when measuring H^- mobilities.

As previously mentioned, the electrons cross the ionization region in a narrow strip parallel to the source front plate. This restricts ion production by electron bombardment to this same narrow region. Once ions are produced, they are quickly thermalized by collisions with the gas in the source. At the same time, they are slowly drifting toward the source exit aperture under the influence of an electric field produced by potentials on the repeller plate, filament and collector enclosures, and source front plate. The ions are prevented from entering the drift region by a small d.c. bias on the Tyndall grid. Periodically the Tyndall grid is pulsed to allow the ions to enter the drift region. In general the source potentials must be adjusted so that $< \frac{1}{2}$ volt d.c. bias on the Tyndall grid completely prevents any ions from entering the drift region. If a much larger bias is required to "turn off" the ions, it is found that pulsing the Tyndall grid will not let any ions through. There are several reasons for this and one develops a "feel" for setting up the source after making many runs. When the potentials in the source are large, the ions have appreciable kinetic energy after being created. By the time these ions reach the source exit aperture they still have not lost all the excess energy above thermal. If these ions are to be completely "turned off" or prevented from entering the drift region, a relatively large bias is required on the Tyndall grid. This potential is sufficiently large to prevent ions from reaching the source exit aperture. When the narrow ($\sim$ 1 μsec) Tyndall grid pulse is applied,

the ions are so far away as to not be able to be brought through the source exit aperture in the duration of the pulse. It is of course always possible to use a large enough pulse to bring the ions through; however, in that case the ions would not be gated into the drift region already in a steady state drift condition but rather thrown into the drift region at energies above the equilibrium value.

The distance the ions drift in the source is 1.5 cm and is usually sufficient to allow the ions to reach energy equilibrium with the gas and electric field in the source. Under conditions where the ions cannot reach equilibrium in this distance, provision is made to externally adjust the electric field within the source and thus provide a longer residence time in which to reach equilibrium.

After some experience is obtained, it is usually possible to adjust the source so that a sharp cutoff with the Tyndall grid is obtained and the ions are still capable of being brought "back" with small pulses. A background noise count rate is produced by ions leaking through the Tyndall grid cutoff. Noise count rate of < 1 percent are common and no runs are made where this count rate exceeds 5 percent.

When ions are gated through the Tyndall grid, it is desirable to use a pulse width smaller than the channel width of the time-of-flight analyzer. This prevents the arrival time spectrum from reflecting the detailed shape of the source pulse of ions. For example, let the channel width of the analyzer be 4.0 μsec and the width of the Tyndall grid pulse be 2.0 μsec. If the drift length is made so small that the ions are detected immediately after entering the drift region, they have had no time to diffuse and are all detected in either one or

two adjacent channels. So long as the width of the Tyndall grid pulse is less than the channel width of the analyzer, the greatest detail of the source pulse is contained in only two adjacent channels. As the drift length is made longer, the ions diffuse and quickly lose their "memory" of the shape of the source pulse. If on the other hand, a wide Tyndall grid pulse is used, corresponding to many channel widths, the arrival time spectrum would reflect not only the diffusion and reaction properties of the ions but also the shape of the initial ion distribution. In practice it is always possible to use Tyndall grid pulses no wider than two channel widths. Thus the maximum detail of the source distribution is contained in two or three adjacent channels. The Tyndall grid pulses are "square waves" and experimentally no detail of the source pulse is observed in the arrival time spectra.

Analysis Region Parameters

Molecular ions can possible be dissociated by potentials in the analysis region. To ensure that this does not occur the potentials on the skimmer, focusing elements, and quadrupole mass filter are varied. If no change in the relative abundances of the ionic species is noticed, it is unlikely that dissociation is occurring. No dissociation was observed for H_3^+ ions and the potentials were adjusted for best detection efficiency. Also no electron detachment from H^- is detected.

Analysis Time

The analysis time is the time difference between the instant when an ion arrival is recorded by the time-of-flight analyzer and the time when the detected ion actually exited the drift region. This

time is composed of two distinct parts: (1) the time an ion takes from the instant when it leaves the drift region until it impinges on the channeltron and (2) the time the electronics takes to detect the impinging ion and record its arrival in the time-of-flight analyzer. The latter time is a fixed property of the electronics and is constant; however, the first time depends upon the system pressure and analysis parameters. The analysis time is unknown and must be determined to obtain accurate arrival times. The analysis time will, however, remain constant for a specific ionic species if the conditions in the analysis region are not changed. This requires that the potentials on the skimmer and the focusing lens be held constant while making measurements. In addition the operating parameters of the rf quadrupole must be held constant. The potentials on the poles of the quadrupole mass filter are altered by changing the d.c. bias, resolution, or mass. Thus all three controls must be left at fixed values during a measurement.

Boundary Conditions

The transport equation developed in Chapter III describes the motion of a tenuous swarm of ions drifting in a gas of constant number density N and temperature T under the influence of a uniform electric field. This equation has been solved for specific initial and boundary conditions. The extent to which the solution describes the actual physical situation depends upon the degree to which the assumed initial and boundary conditions are satisfied. The ions are assumed to drift in unbounded space; however, the drift region is in fact bounded by the source plate, end plate, and guard rings. We shall consider each

of these boundary effects separately.

Radial Effects

Radially the drift region is bounded by the guard rings at a radius of 8.75 cm. Any ions which diffuse to the guard rings will either be absorbed or reflected; however, before the ions reach the guard rings the electric field becomes non-uniform. Albritton [17] has shown that electric field remains uniform within 1 percent for $r < 6$ cm and that for $r > 6$ cm the electric field quickly becomes non-uniform. Any ions which diffuse into the region of non-uniform electric field and then back on-axis may distort the arrival time spectrum. Since diffusion is a random walk process, the probability of an ion diffusing from on-axis to a radius r and back again is the same as for an ion diffusing from on-axis to a radius 2r. For a single ionic species undergoing depleting reactions only, Schummers [45] has evaluated the fraction of ions within a radius r_1 as a function of $4D_T t$. He showed that less than 1 percent of the ions lie outside a radius of 12 cm for $(4D_T t) < 30$. Thus for $(4D_T t) < 30$, fewer than 1 percent of the detected ions have diffused radially past 6 cm and back on-axis. In Table 2 the quantity $4D_T t$ is evaluated for each ion at a high, intermediate, and low value of E/N. The value of D_T used is the Wannier value and the value of t used is the measured average arrival time. All times are for position 7, the longest drift length, for which transverse diffusion would be the greatest. Since v_d is constant for a fixed E/N, the average arrival time will be constant (for a specific drift length) as the pressure is varied provided the ration E/N remains the same. Since $D_T \sim 1/N$, the term $4D_T t$ will also

Table 2. Tabulation of $4D_T t$ for Ions Drifting in H_2 at Various Values of E/N.

Ion	E/N (Td)	t 10^{-6} sec	D_T cm^2/sec	$4D_T t$ cm^2	P Microns	Posn	$4D_T t$ P $10^{-2} cm^2$.micron
H^-	5	818	3315	10.8	300	7	32.5
H^-	25	180	11894	8.6	200	7	17.1
H^-	70	79	44033	13.9	200	7	27.8
H^+	4.5	2172	1778	15.4	200	7	30.9
H^+	25	423	2112	3.6	200	7	7.1
H^+	100	132	7029	3.7	150	7	5.6
H_3^+	10	1437	1246	7.1	200	7	14.3
H_3^+	25	584	1376	3.2	200	7	6.4
H_3^+	65	219	2422	2.1	200	7	4.2

be $\sim 1/N$. To facilitate comparison between values at different pressures, the value $4D_T t$ is normalized to a pressure of 100 microns by multiplying each value of $4D_T t$ by the pressure, in hundreds of microns, at which it was measured. This number is the value of $4D_T t$ which would be obtained at position 7 if the pressure during the measurement were 100 microns. These calculations indicate three things. (1) At the pressures of these specific measurements, much fewer than 1 percent of the ions detected have diffused radially past 6 cm and back again even for the longest drift lengths. (2) At 100 microns only H^+ and H^- ions would have values of $4D_T t > 30$, and then only at low values of E/N and the longest drift lengths. (3) The value of $4D_T t$ at 100 microns is greatest for low values of E/N. Thus low E/N values are the "worst case" for the present measurements.

To ensure that the radial boundary conditions do not affect the results, no arrival time spectra are taken for H^- at pressures below 200 microns, and none for H^+ and H_3^+ at pressures below 100 microns. At such pressures and over the range of E/N covered the arrival time spectra are not distorted by radial boundary effects.

End Effects

The boundaries of the two ends of the drift region, the source front plate and the end plate, can also alter the arrival time spectrum. Gatland [20] considers the end effects to fall into two categories; (1) the effects of ion production and sampling and (2) the effects of conducting end plates and their associated boundary conditions.

First the effects of ion production and sampling are considered.

When the ions are introduced into the drift region from the source they may enter at energies above equilibrium values. Thus the ions require several mean free paths in which to equilibrate with the gas and electric field. The net result is that the ions are created a few mean free paths inside the drift region with an initial diffusion. This effect will, however, remain constant for each drift distance.

To sample the ions, the end plate has a small circular aperture located on axis that enters a differentially pumped region. Gas within a small volume around the hole will have a flow toward the hole because of the lower pressure in the differentially pumped region. This will give ions within this volume an additional velocity component in the z direction. The exit aperture is small (0.035 cm diameter) and appreciable velocity flow will occur within only a very few hole diameters of the exit aperture. The effect of this flow is to sample all ions within a small volume close to the exit aperture instead of only ions striking the aperature. The average sampling distance is thus moved within the drift region by a small distance. The effects of this flow are difficult to evaluate; however, the flow is independent of drift distance. To first order it is reasonable to assume that the effect of sampling is independent of drift distance.

The conducting front and end plates introduce the boundary conditions

$$n(r,\ z = 0,\ t) = 0 \text{ for } t > 0 \qquad (4\text{-}9)$$

and $$n(r, z = d, t) = 0. \qquad (4\text{-}10)$$

Gatland [20] has solved the transport equation described in Chapter III and applied these boundary conditions. The time of arrival of the peak ion current is evaluated from the solutions of the transport equation with and without the boundary conditions. The difference in these time measurements is shown to be $3D_L/v_d^2$ by not allowing for the end boundary conditions. This correction is also independent of drift length. It should be emphasized that this correction strictly applies only to the peak of the ion current; however, again it is reasonable to assume this is a first order correction over the width of an arrival time spectrum. End effects that remain constant for different drift distances alter the time of arrival of each ion by the same amount. This time remains the same for all drift lengths and may be considered as part of the constant analysis time. End effects of this nature are eliminated by by the differencing technique.

Not all end effects are constant for different drift distances. Miller [2] has shown that at short drift distances (positions 1 and 2) the end effects are accentuated and can cause erroneously high drift velocity measurements. To minimize any end effects not eliminated by the differencing technique, long drift lengths are used. Typically measurements are made at positions 7, 6, 5, and 4 where the shortest drift length is about 25 cm. In the present experimental apparatus the best indication that end effects are negligible is the close

agreement between the experimental arrival time spectra and the theoretically predicted spectra. Sample spectra for H^-, H^+, and H_3^+ are shown later in this chapter.

Experimental Procedures

Drift velocities are determined by taking arrival time spectra for two or more drift distances. During a "run" all source conditions, drift region parameters, and analysis region parameters are maintained constant; only the drift length is changed. A run usually consists of taking arrival time spectra at the four longest drift distances, corresponding to positions 7, 6, 5, and 4. The drift velocities are determined by the differencing technique discussed in Chapter III. The number of channels covered by an arrival time spectrum is determined by visual inspection of the scope display on the T.O.F. analyzer. The high(H) and low(L) channel number limits of the spectrum are used to determine an average background noise level. The average noise count per channel is given by:

$$\overline{nc} = \frac{\sum_{k=1}^{L} n_k + \sum_{k=H}^{256} n_k}{257 - H + L} \qquad (4\text{-}11)$$

The k^{th} channel is given by $\eta_k = n_k - \overline{nc}$. The corrected arrival time spectra are used to calculate drift velocity, longitudinal diffusion coefficients, and reaction rates.

The average arrival time of the ions from the i^{th} source position is given by

$$\overline{t_i} = DLY_i + \frac{\sum_{k=1}^{256} \eta_k \tau_k}{\sum_{k=1}^{256} \eta_k} \qquad (4\text{-}12)$$

Here DLY_i is the delay between the time when the ions are gated into the drift region (t=0) and the start of the T.O.F. analyzer (see Figure 6). The time corresponding to the center of the k^{th} channel of the T.O.F. analyzer is τ_k. This time is measured from the start of the analyzer; i.e., the start of channel 1 corresponds to $\tau = 0$. For example, the center of channel 1 corresponds to $\tau_1 = c.w./2$ and the center of the k^{th} channel corresponds to $\tau_k = (k - \frac{1}{2})$ c.w. Equation (4-12) is the experimental equivalent of the theoretical average arrival time given by Equation (3-77)

$$t = \frac{\int_0^\infty t\Phi(z,t)dt}{\int_0^\infty \Phi(z,t)dt} . \qquad (4\text{-}13)$$

The average arrival times are calculated from the spectra at each drift length. These times are fitted by a least squares fit to the equation

$$t = t_A + \frac{z_i}{v_d} . \qquad (4\text{-}14)$$

Here, t_A is the analysis time, z_i is the drift length, and v_d is the

drift velocity. Since this equation has two unknowns (t_A and v_d), at least two experimental values for $\overline{t_i}$ are required at different drift lengths, z_i, to obtain a valid fit. This least squares fit is equivalent to differencing between the individual values to obtain the drift velocity from Equation (3-80)

$$v_d = \frac{z_i - z_j}{\overline{t}_i - \overline{t}_j} \tag{4-15}$$

The value of v_d thus obtained is used to calculate the mobility from the defining equation

$$K = v_d/E \tag{4-16}$$

The mobility is then reduced to standard conditions and presented in the form of the reduced mobility (Equation 1-2)

$$K_o = K \left(\frac{P}{760} \right) \left(\frac{273.16}{T} \right) . \tag{4-17}$$

Experimental Results

The drift velocities and reduced mobilities have been measured over a wide range of E/N at 300°K. These results are presented graphically in this section and numerical results are tabulated in Appendix I.

H^+

The drift velocity and reduced mobility of H^+ ions drifting in

H_2 has been measured at 300°K over the range of E/N from 4 to 100 Td. The pressures at which these measurements were made were 100, 150, and 200 microns. The drift velocities and reduced mobilities are shown in Figures 7 and 8, respectively, as a function of E/N. The drift velocity has constant slope and the reduced mobility has constant value below and E/N of ~ 10 Td. This fact indicates that in this region the thermal energy dominates the field energy and the ions have a velocity distribution that is approximately Maxwellian. Thus, for H^+ ions in H_2 the region below ~ 10 Td can be considered the low-field region and a zero-field reduced mobility can be obtained from reduced mobility measurements over this region. To obtain a zero-field reduced mobility, $K_o(0)$, the 16 values of K_o below 10 Td were averaged to obtain $K_o(0) = 16.034 \simeq 16.0$ $cm^2/V \cdot sec$. This value is in excellent agreement with other measurements made with apparatus using mass analysis. As previously stated, no comparison will be made with experimental results taken without mass analysis since under those conditions it is impossible to be certain of the ionic identity. Comparison of the present measurements and those of other experimenters is contained in Table 3. Saporoschenko [14] also measured the mobility of H^+ in H_2 using mass analysis, but his data did not exhibit a zero slope at low E/N and a zero-field value was not quoted. His data did, however, exhibit the general behavior at high E/N that the present data show.

An approximate average ionic energy can be calculated from Wannier's Equation (1-14). This equation is

$$\langle E \rangle = \frac{1}{2} m v_d^2 + \frac{1}{2} M v_d^2 + \frac{3}{2} kT \qquad (4\text{-}18)$$

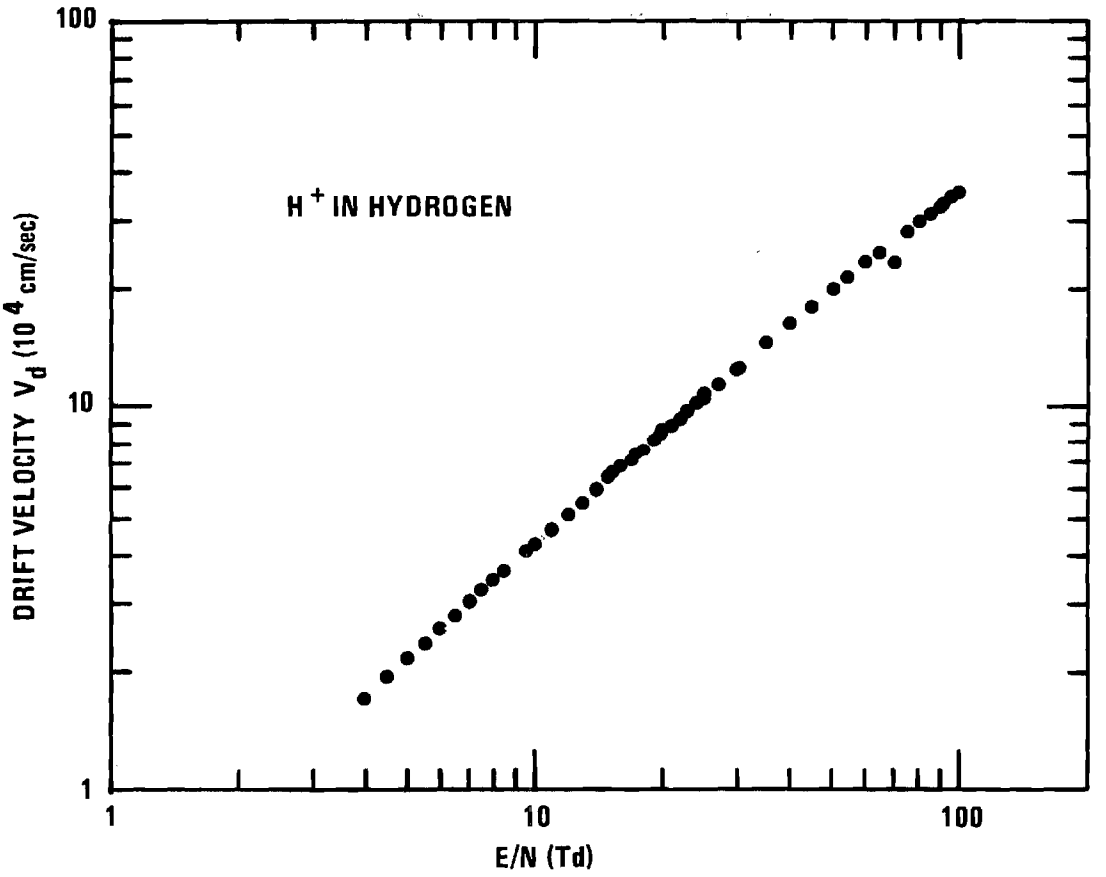

Figure 7. Drift Velocity of H^+ Ions in H_2 Gas at 300°K as a Function of E/N.

Table 4. Average Ionic Energies as a Function of E/N Computed from the Wannier Energy Equation.

Ion	Gas	E/N Td	⟨E⟩ eV
H^+	H_2	5	0.04
H^+	H_2	10	0.04
H^+	H_2	20	0.05
H^+	H_2	30	0.06
H^+	H_2	50	0.10
H^+	H_2	85	0.19
H^+	H_2	100	0.24
H_3^+	H_2	5	0.04
H_3^+	H_2	10	0.04
H_3^+	H_2	20	0.05
H_3^+	H_2	30	0.06
H_3^+	H_2	50	0.10
H_3^+	H_2	85	0.29
H^-	H_2	5	0.04
H^-	H_2	10	0.06
H^-	H_2	20	0.12
H^-	H_2	30	0.21
H^-	H_2	50	0.46
H^-	H_2	70	0.79

Reaction effects will cause the measured drift velocity, v_d', to be larger than the actual drift velocity, v_d. The magnitude of this correction is calculated to be a maximum (0.7 percent) at an E/N of 4 Td and at a pressure of 100 microns. This correction rapidly decreases with increasing E/N and is 0.1 percent at an E/N of 10 Td.

The shape of the arrival time spectrum is the best indication of reactions or end effects. A typical arrival time spectrum of H^+ in H_2 is shown in Figure 9. The histogram represents the experimental data corrected for noise counts and the smooth curve is a theoretical fit based upon the predicted shape of the arrival time spectrum from Equation (3-74). The areas under the two curves are normalized to the same value and this fit is obtained by varying only the time corresponding to the start of channel 1, T1, and the longitudinal diffusion coefficient D_L. The transverse diffusion coefficient used is from the Wannier equation (see Chapter V) and all other parameters are known. The agreement between the two curves indicates that reactions and end effects are not important under the specific experimental conditions involved.

H_3^+

The drift velocities and reduced mobilities for H_3^+ in H_2 are presented in Figures 10 and 11, respectively. These measurements cover the range of E/N from 4.5 to 85 Td at pressures of 100 to 300 microns. Again the predominant features of the figures can be correlated with the average ionic energies in Table 4. In constrast with H^+ ions, for H_3^+ ions the slope of the drift velocity vs. E/N curve increases and

E/N = 24.98 Td
P = 196.9 microns
z = 43.775 cm
T1 = 352.0 μsec
c.w. = 0.5 μsec

$v_d = 10.54 \times 10^4$ cm/sec
$D_L = 2297$ cm^2/sec
$D_T = 2112$ cm^2/sec
$\alpha = 0.0$ sec^{-1}

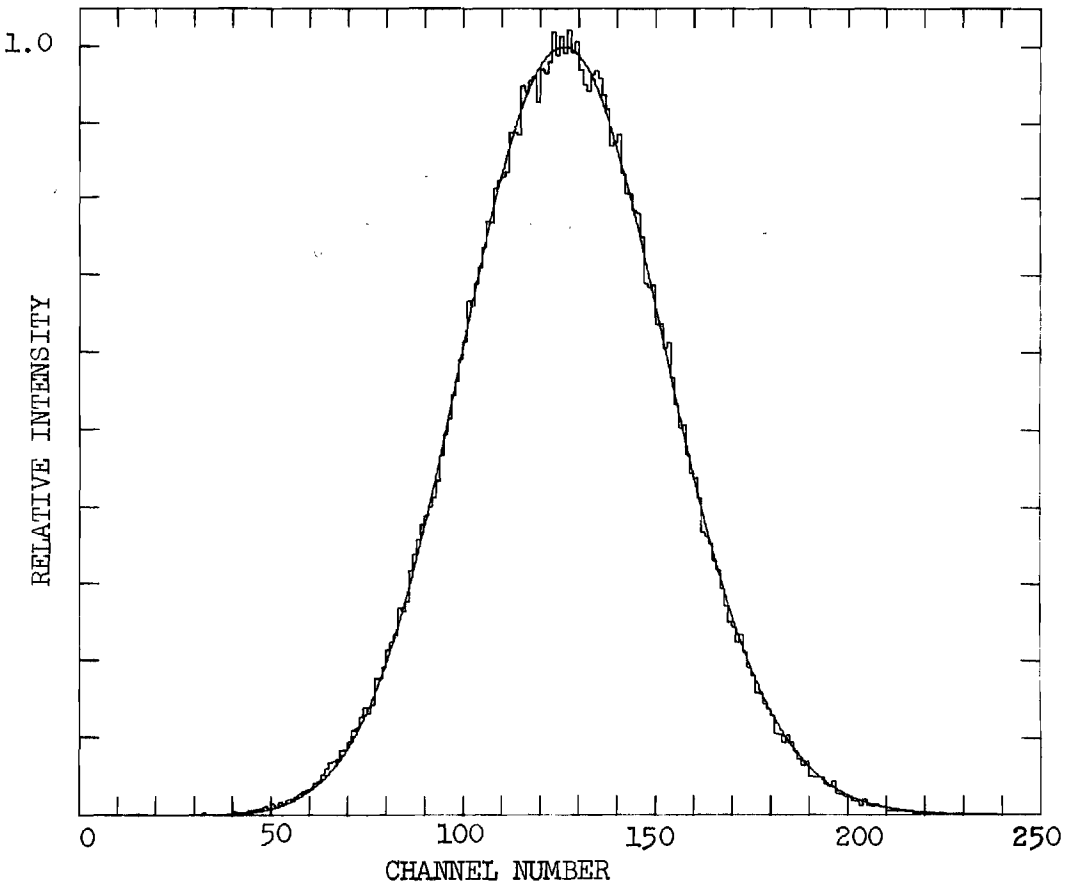

Figure 9. Arrival Time Spectrum for H^+ Ions in H_2 Gas at 300°K.

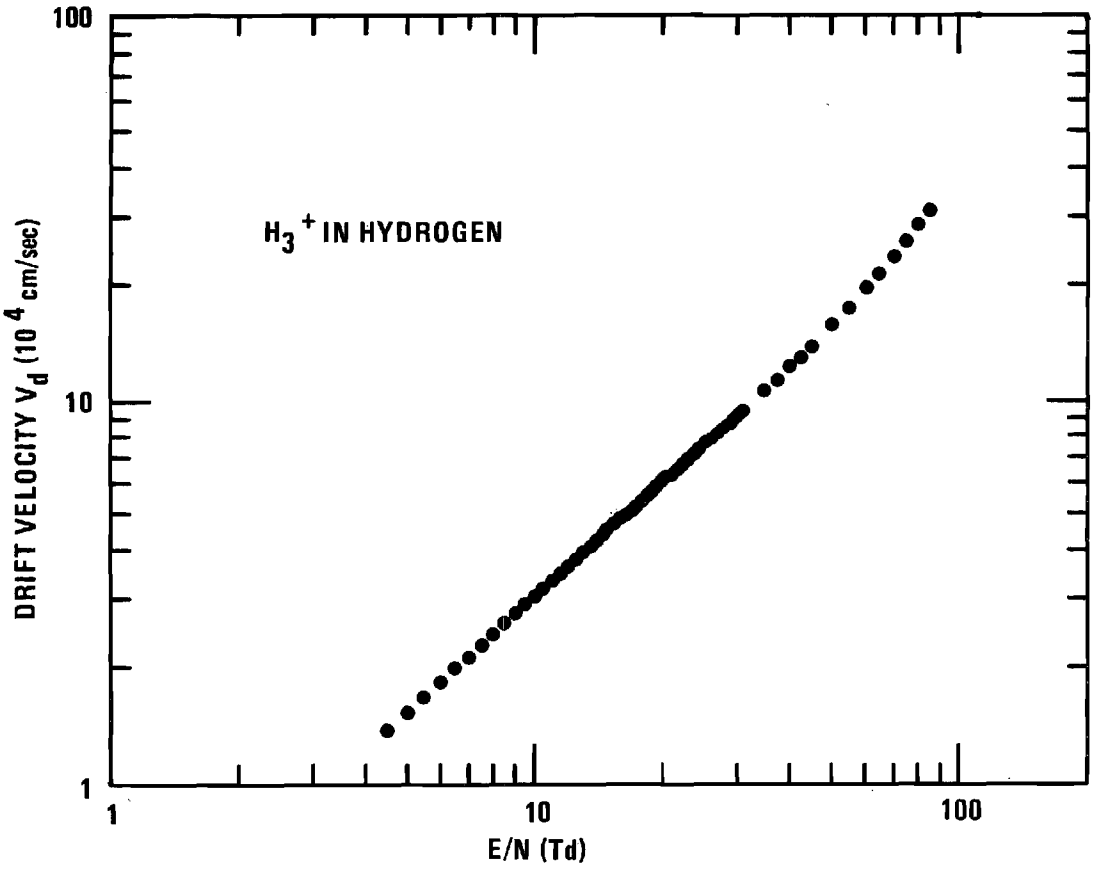

Figure 10. Drift Velocity of H_3^+ Ions in H_2 Gas at 300°K as a Function of E/N.

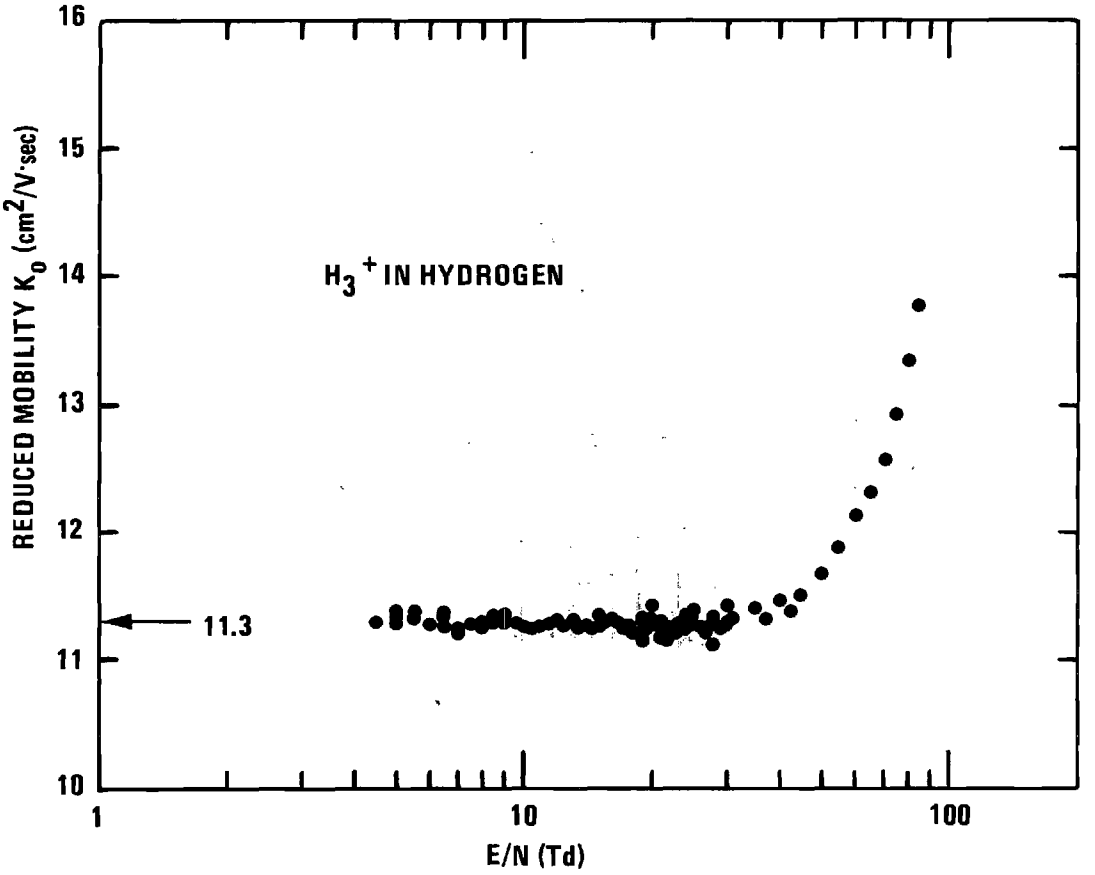

Figure 11. Reduced Mobility of H_3^+ Ions in H_2 Gas as a Function of E/N.

the reduced mobility rises in the high-field region. The differences can be qualitatively explained in terms of the different interactions between H^+ and H_3^+ with H_2. At the energies involved here H^+ behaves like a point charge whereas H_3^+ is a molecular ion capable of being excited rotationally and inductively polarized, and it possesses a quadrupole moment. In addition H_3^+ may possibly undergo proton exchange with H_2 (Equation (1-15)). The mobility of H_3^+ is measured under consitions where there are no H^+ ions in the drift region to distort the arrival time spectrum. There is also no noticeable distortion of the arrival time spectrum due to reactions forming H_5^+ (Equation (4-8)) or end effects. Figure 12 is a representative arrival time spectrum of H_3^+ in H_2. The theoretical fit is obtained again by adjusting only T1 and D_L. The zero-field reduced mobility is obtained by averaging the 62 values below an E/N of 25 Td to obtain $K_o(0) = 11.282 \simeq 11.3$ cm^2/V·sec.

D^+ and D_3^+

The reduced mobilities of D^+ and D_3^+ in D_2 have been measured and are presented in Figures 13 and 14 respectively. The primary purpose of making measurements on deuterium is to check for possible large experimental errors. Between similar systems the mobility should scale according to the inverse square root of the reduced mass. In the case of isotopes the interaction potentials are identical and only the mass is different. Here this scaling law is strictly true. The zero field reduced mobility of D^+ is measured to be $11.708 \simeq 11.7$ cm^2/V·sec for the 12 measurements below 20 Td. The mass scaling from H^+ in H_2 indicates that $K_o(0)$ should be ~ 11.3 cm^2/V·sec; however, this is

E/N = 29.94 Td
P = 196.9 microns
z = 43.775 cm
Tl = 419.8 μsec
c.w. = 0.5 μsec

$v_d = 9.08 \times 10^4$ cm/sec
$D_L = 1899$ cm^2/sec
$D_T = 1410$ cm^2/sec
$\alpha = 0.0$ sec^{-1}

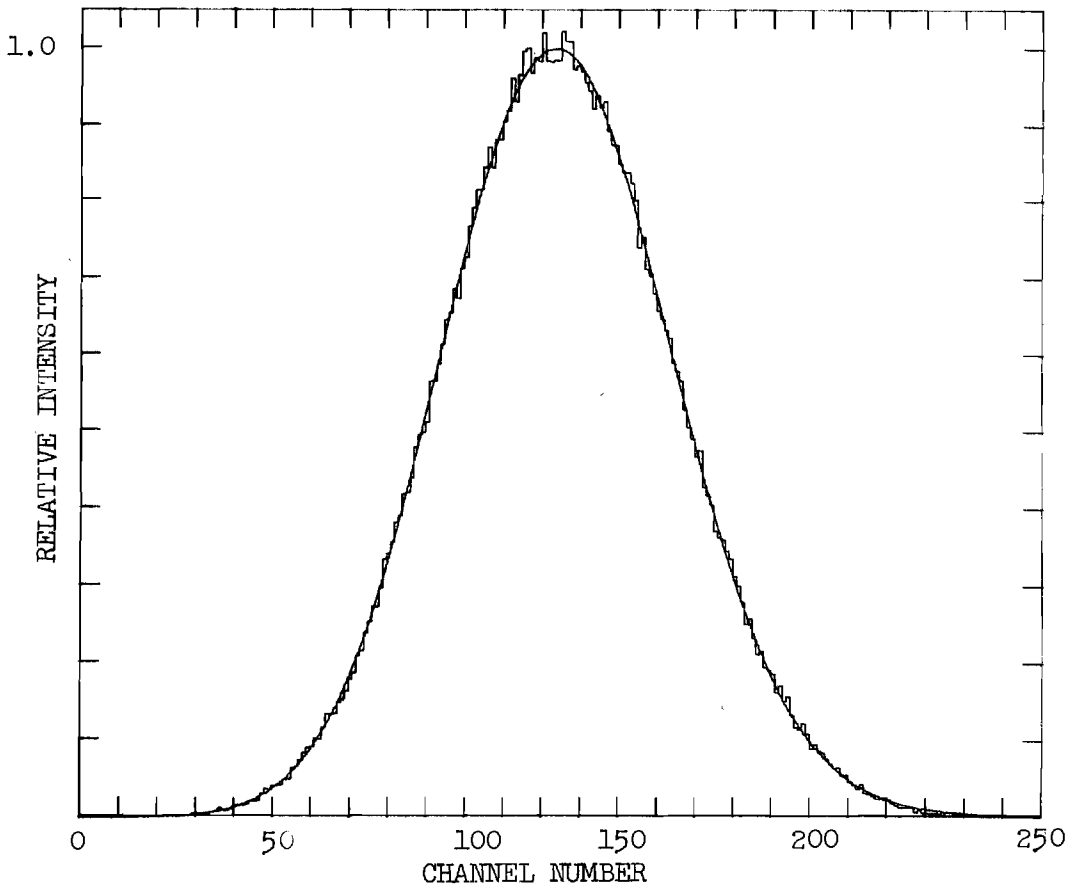

Figure 12. Arrival Time Spectrum for H_3^+ Ions in H_2 Gas at 300°K.

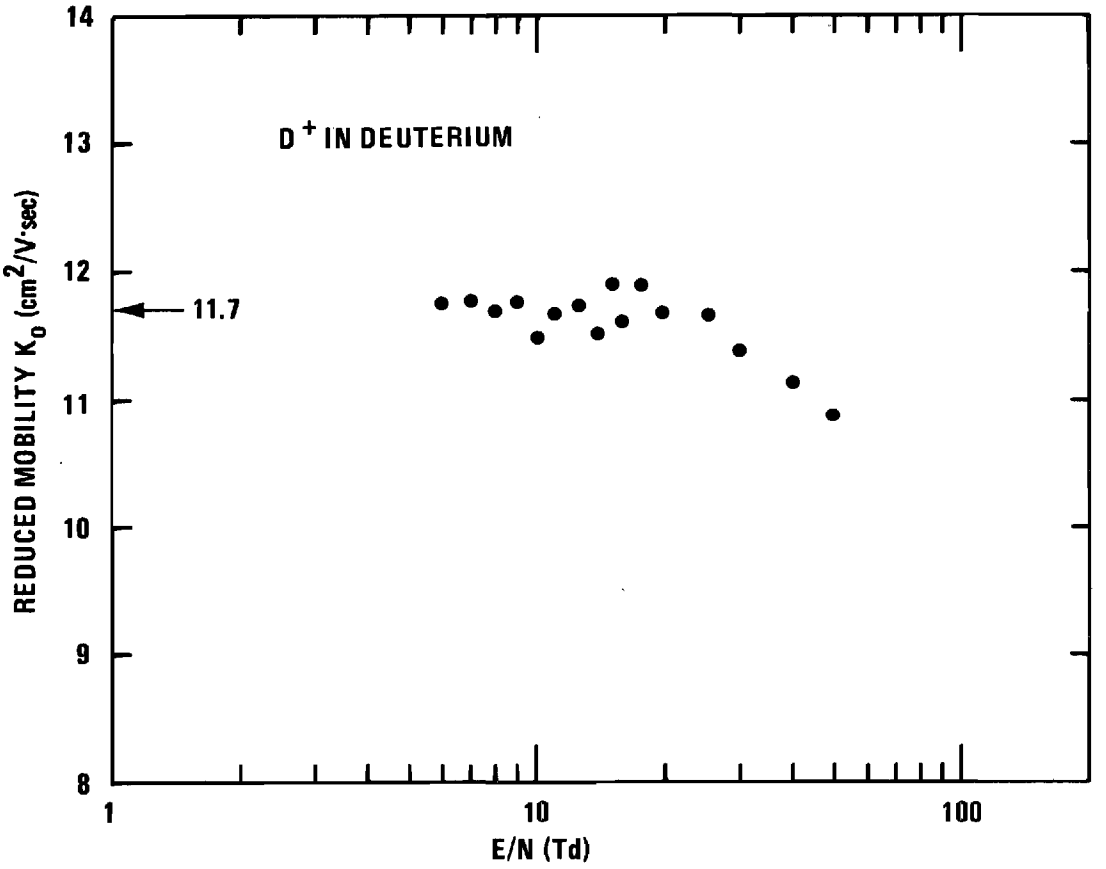

Figure 13. Reduced Mobility of D^+ Ions in D_2 Gas at 300°K as a Function of E/N.

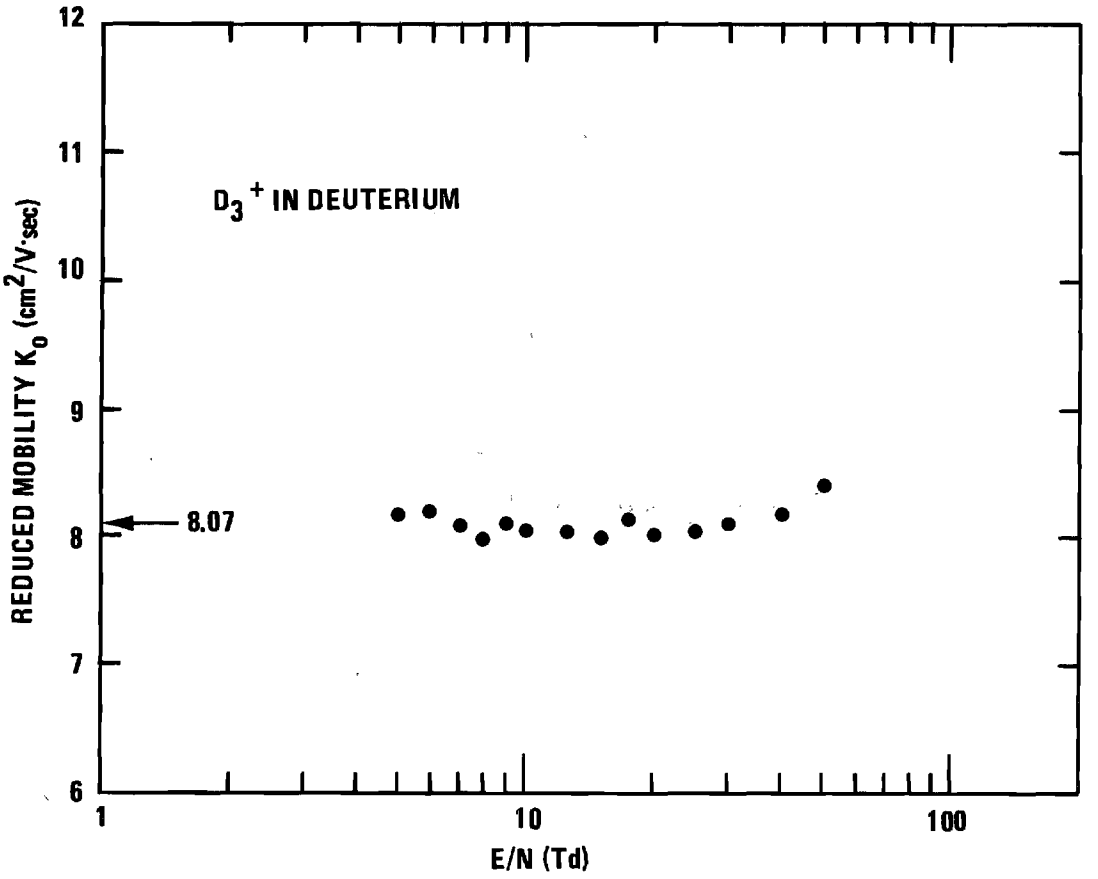

Figure 14. Reduced Mobility of D_3^+ Ions in D_2 Gas at 300°K as a Function of E/N.

within the error bounds of the D^+ in D_2 measurement. For D_3^+ in D_2, $K_o(0)$ is measured to be $8.065 \simeq 8.07$ $cm^2/V \cdot sec$ for the 10 measurements below 20 Td. Here the mass scaling from H_3^+ in H_2 indicates $K_o(0)$ should be ~ 7.98 $cm^2/V \cdot sec$, in good agreement with the experimental value.

$\underline{H^-}$

The drift velocity and reduced mobility have been measured for H^- in H_2 over a range of 2.5 to 70 Td and are presented in Figures 15 and 16. These measurements were made at pressures between 200 and 750 microns. The overall shape of these curves is similar to those for H^+ in H_2; however, the remarkable feature of these curves is that H^- drifts much faster than H^+. The zero-field reduced mobility is determined from the 23 measurements below 15 Td to be $43.023 \simeq 43.0$ $cm^2/V \cdot sec$. This is about 2.7 times as large as $K_o(0)$ for H^+ (Figure 17). Because this result was unexpected, the experimental conditions were widely varied to ensure that the result was not due to experimental error. No variance of K_o was observed for large changes in source conditions, drift region parameters, and analysis region parameters. The possibility of electrons in the drift region introducing error was considered and ruled out for the following reasons. (1) The characteristic drift velocity of electrons in H_2 is well known and at 2.5 Td the electron velocity is about 10^6 cm/sec whereas the drift velocity for H^- is about 3×10^4 cm/sec. (2) The differencing technique would eliminate any effects of electrons creating H^- ions part way down the drift region. (3) Once electrons are in the drift region they have insufficient energy to produce H^- ions by dissociative attachment to H_2 molecules.

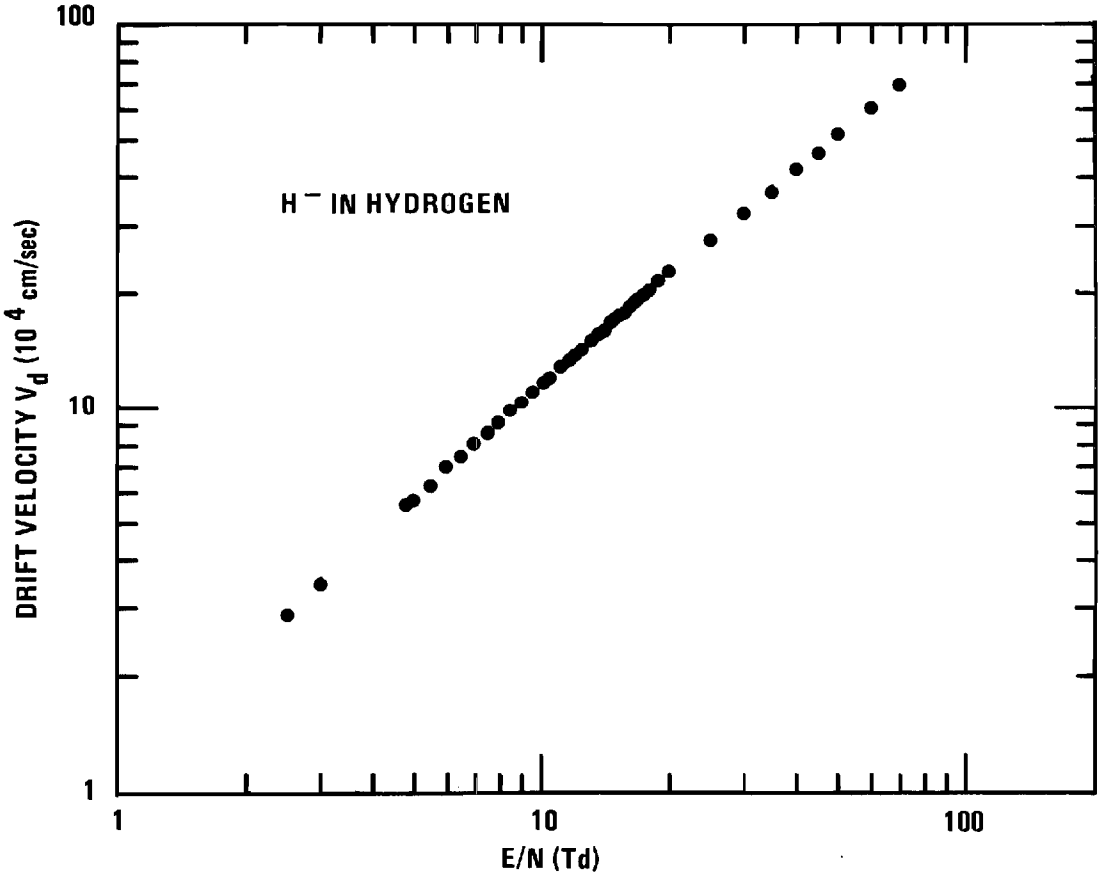

Figure 15. Drift Velocity of H^- Ions in H_2 Gas at 300°K as a Function of E/N.

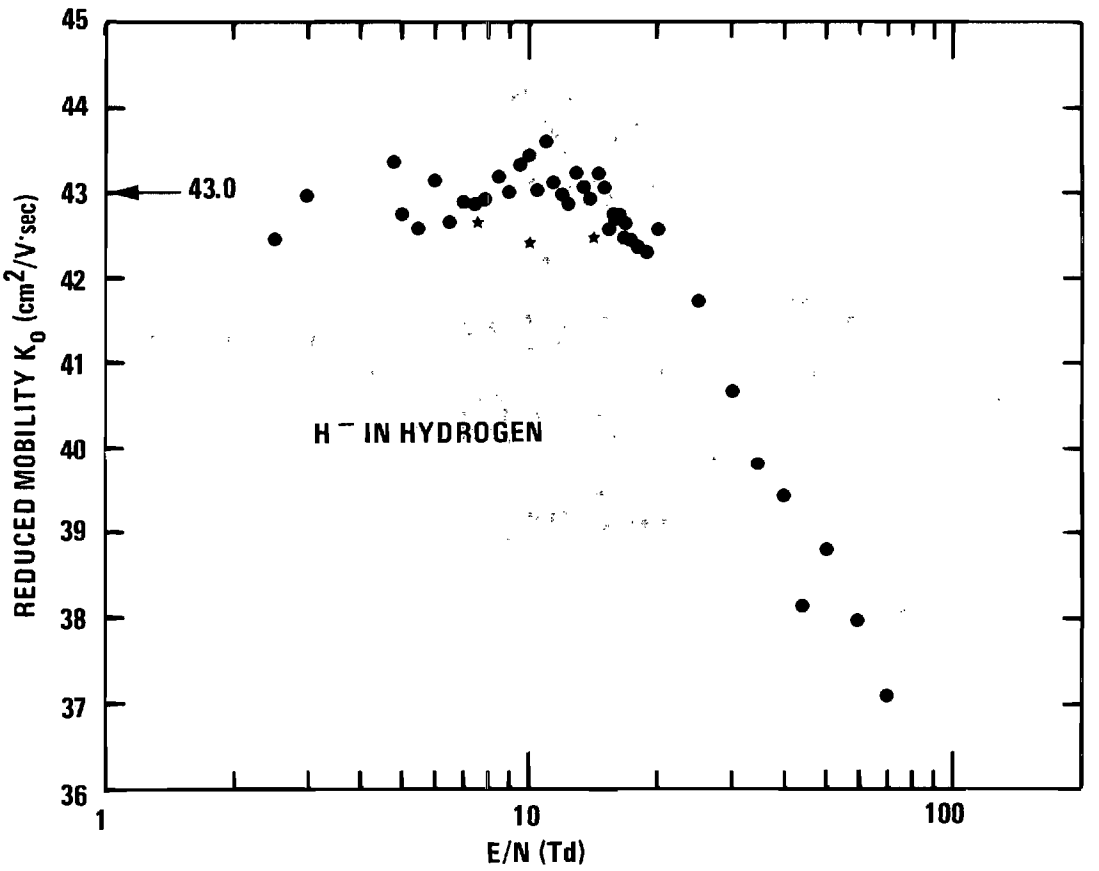

Figure 16. Reduced Mobility of H^- Ions in H_2 Gas at 300°K as a Function of E/N.

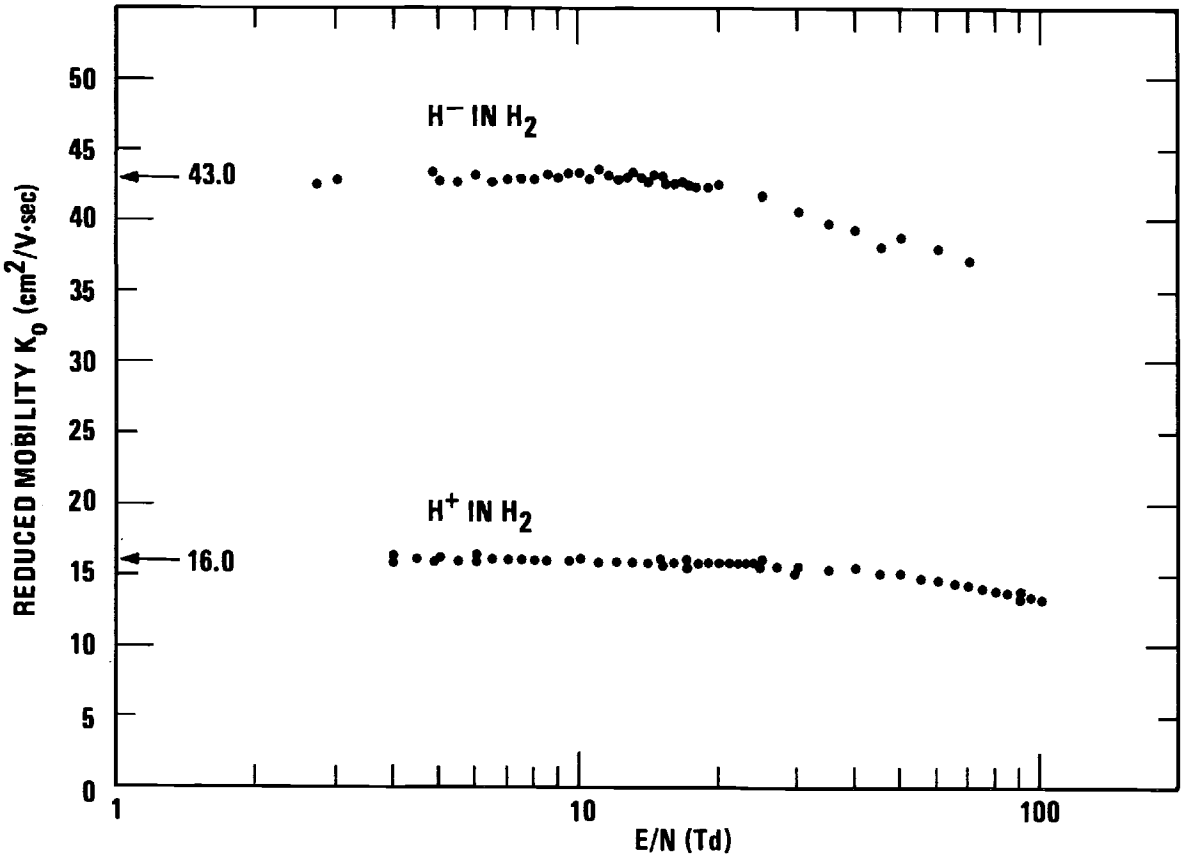

Figure 17. Reduced Mobilities of H^+ and H^- Ions in H_2 Gas at 300°K as a Function of E/N.

The arrival time spectrum of H^- in H_2, Figure 18, indicates that measurements are not distorted by end effects. Since H^- does not react with the gas there are no corrections to the drift velocities.

Joyce Kaufman [46] has offered a qualitative explanation of the large difference in mobilities of H^+ and H^-. Since H^+ reacts with H_2, the ion can closely approach the H_2 molecule and probably undergoes spiraling collisions. While the spiraling is occurring, the charge carrier has the mass of the complex ion $H^+ \cdot H_2$ and hence a considerably reduced drift velocity. The H^- ion, on the other hand, does not react with the gas and thus probably does not closely approach the H_2 molecule or undergo spiraling collisions. By not closely approaching the H_2 molecule the H^- ion is thus not "held" in the interaction. However, the large difference in the magnitudes of the mobilities of H^+ and H^- is remarkable, as is the large deviation of the H^- zero-field reduced mobility from the Langevin polarization limit value, which is 18.8 $cm^2/V \cdot sec$ for both H^+ and H^- in H_2.

Mason and Vanderslice [48] have determined the $H^- - H_2$ potential in the range from 0.87 to 2.0 $\mathring{A}$ by analysis of elastic scattering cross sections. An expression that fits this potential and has the proper behavior at large r is

$$V(r) = [129\, e^{-2.72r} - (5.81/r^4)]\ eV,$$

where r is in angstroms. Whealton and Mason [49] used (8-4) and (12-4) potentials that have the correct well depth and polarization tails in a classical calculation of the zero-field reduced mobility of the H^-

E/N = 15.01 Td
P = 196.9 microns
z = 43.775 cm
T1 = 186.7 μsec
c.w. = 0.5 μsec

$v_d = 17.37 \times 10^4$ cm/sec
$D_L = 10890$ cm^2/sec
$D_T = 7651$ cm^2/sec
$\alpha = 0.0$ sec^{-1}

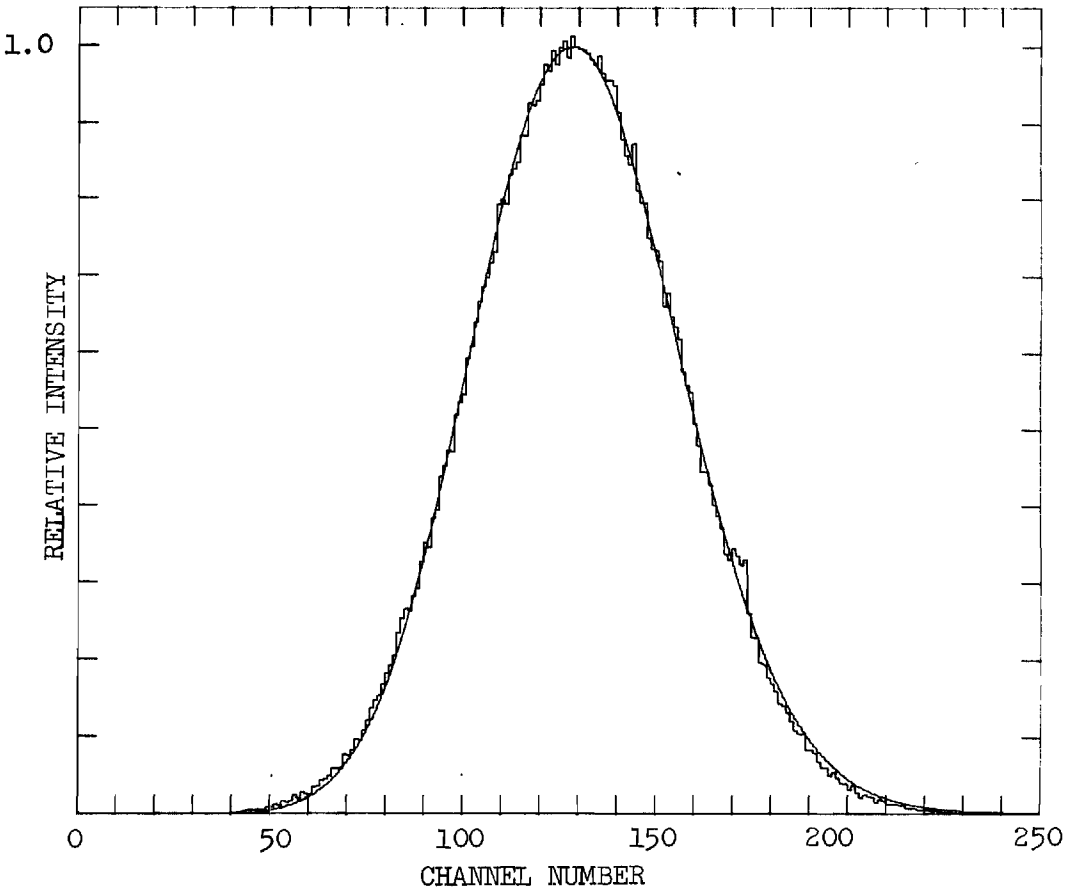

Figure 18. Arrival Time Spectrum for H^- Ions in H_2 Gas at 300°K.

ion in H_2 at 300°K and obtained the values 31.4 and 27.5 $cm^2/V \cdot sec$, respectively. The measured value of 43.0 is well above the theoretical mobilities, and this difference is thus far unexplained. One possible explanation is that the repulsive part of the H^- - H_2 potential is considerably softer than that used in the calculation. Another possibility is that some additional mechanism other than elastic scattering should be considered in the theory.

The mobility of H^- in H_2 has not been measured by other experimenters; however, Albritton [50] and McFarland [51] have measured the reduced mobility for H^- in He and report a value of 39 $cm^2/V \cdot sec$.

D^-

The drift velocity and reduced mobility of D^- in D_2 was measured for three values of E/N. The reduced mobility has been scaled according to the inverse square root of the reduced mass to compare with H^- and the data are presented as stars on Figure 16. The data have an average $K_o(0)$ of 30.08 ≃ 30.1 $cm^2/V \cdot sec$. The scaled $K_o(0)$ of H^- is 30.4, in excellent agreement with the present measurement.

Error Analysis

The measurement of the drift velocities from arrival time spectra requires the drift length and drift time for at least two positions to be known. The reduced mobility is then calculated from the drift velocity in terms of the experimentally measured quantities v_d, E, P, at T from the equation:

$$K_o = \frac{v_d}{E} \left(\frac{P}{760} \right) \left(\frac{273.16}{T} \right) \qquad (4\text{-}20)$$

$$= \frac{\Delta z/\Delta t}{V/z} \left(\frac{P}{760} \right) \left(\frac{273.16}{T} \right)$$

The errors in the measured quantities arise from the five basic experimentally determined quantities: length z, time t, drift potential V, pressure P, and temperature T. The source and magnitude of these individual errors will be considered separately.

Drift Length

The drift length of any position is considered to be known within ± 0.008 cm and successive positionings of the source are repeatable within ± 0.003 cm. In the present research no data are taken at drift distances shorter than about 12.5 cm. For a single position measurement the maximum systematic error is ± 0.064 percent and the maximum random error is ± 0.024 percent. In measuring drift velocity two positioning measurements are required. In addition drift length is required to determine the electric field E. Since these errors are additive the total systematic error due to drift length measurements is ± 0.19 percent and the total random error is ± 0.07 percent.

Voltage

The error in electric field due to voltage errors arises from two sources. The accuracy of measurement by the Fluke 881A differential voltmeter is considered to be ± 0.01 percent. The primary source of error is the 0.1 percent resistors determining the guard ring potentials. Although the actual potentials have been measured to have a much smaller error than indicated by the resistor accuracy (see Table 1), it is possible for the values to change due to thermal drift and an overall

accuracy of ± 0.1 percent is assigned to the systematic error. A random error of ± 0.05 percent is assigned due to power supply drift (± 0.005 percent per hour) and the error in reading the drift potential from the Fluke 881A DVM.

Temperature

The temperature of the top, center, and bottom guard rings is measured for each arrival time spectrum. A run usually involves four positions and the temperature is obtained by averaging the 12 individual temperature measurements. The overall systematic error of an individual temperature measurement is ± 0.5°C or ± .17 percent at 300°K. The temperature gradient in the drift region due to source heating does not exceed ± 1.5°C. The random error assigned is ± 0.5 percent at 300°K.

Pressure

The possible error in the pressure calibration is considered to be ± 1.0 percent due to comparison with the reduced mobility of K^+ in N_2. The measured values of the zero-field reduced mobility of K^+ in N_2 clustered around an average value with a standard deviation of ± 0.19 percent. The pressure controller maintains the pressure constant within ± 0.0001 Torr and the Baratron drift is less than ± 0.0002 Torr during a run. This corresponds to an error of ± 0.3 percent at 100 microns. The systematic error is ± 1.19 percent and the random error is ± 0.3 percent.

Time

The systematic error in time differencing measurements has been

discussed in Chapter III. The remaining diffusion error for differenced time measurements does not exceed ± 0.1 percent. The reaction correction occurs only for H^+ and D^+ ions and these data have been corrected for the depleting reaction. In a specific run consisting of four positions the criterion for accepting a time measurement is that the random scatter about a straight line fit be less than ± 0.5 percent. In general the random scatter is smaller and on the order of ± 0.2 percent; however, the maximum random error is taken to be ± 0.5 percent. There may also be scatter of measured times between successive runs and the best indication of the random error is the spread among the values. For H^+ and H_3^+ this scatter is taken to be ± 1.0 percent. Thus the total random scatter for these two ions is ± 1.5 percent. The large drift velocities of H^- and D^- ions result in short drift times and a larger scatter among successive measurements. This scatter is approximately ± 2.0 percent and a total random error of time measurements for H^- and D^- is assigned a value of ± 2.5 percent. The scatter among the individual measurements in D^+ and D_3^+ is approximately ± 2.0 percent and a total random error of ± 2.5 percent is assigned.

The errors for the mobility measurements on each of the ionic species is summarized in Table 5. Since the individual systematic errors are independent and the random errors are independent, a measure of the total error is obtained by taking the square root of the sum of the squares of the individual errors. These errors are tabulated below the specific ions in Table 5.

Table 5. Summary of Errors Involved in the Mobility Measurements

Error	Type	H^+	H_3^+	H^-	D^+	D_3^+	D^-
Distance	systematic	0.19	0.19	0.19	0.19	0.19	0.19
	random	0.07	0.07	0.07	0.07	0.07	0.07
Voltage	systematic	0.1	0.1	0.1	0.1	0.1	0.1
	random	0.05	0.05	0.05	0.05	0.05	0.05
Temperature	systematic	0.17	0.17	0.17	0.17	0.17	0.17
	random	0.5	0.5	0.5	0.5	0.5	0.5
Pressure	systematic	1.19	1.19	1.19	1.19	1.19	1.19
	random	0.3	0.3	0.3	0.3	0.3	0.3
Time	systematic	0.1	0.1	0.1	0.1	0.1	0.1
	random	1.5	1.5	2.5	2.5	2.5	2.5
RMS of Systematic and Random Errors		2.03	2.03	2.85	2.85	2.85	2.85

CHAPTER V

LONGITUDINAL DIFFUSION COEFFICIENTS

The longitudinal diffusion coefficients and mobilities are measured from different characteristics of the same arrival time spectra. A necessary but not sufficient condition for accurate measurements of both mobility and longitudinal diffusion coefficients is that the arrival time spectra not be distorted by reactions or end effects. As previously explained in Chapter IV, the best indication that a spectrum is not distorted is the quantitative fit between theory and experiment. The experimental procedures used to minimize reaction and end effects have been discussed in Chapter IV and are the same for a longitudinal diffusion measurement.

Experimental Procedures

The transport equation for an ionic species undergoing only depleting reactions has been solved in Chapter III. The solution for the ionic flux density is given by Equation (3-76)

$$\Phi(z,t) = \frac{a\, s}{4(\pi D_L t)^{\frac{1}{2}}} \left(v_d + \frac{z}{t} \right) \exp \left[-\alpha t - \frac{(z - v_d t)^2}{4 D_L t} \right] \qquad (5\text{-}1)$$

$$\times \left[1 - \exp \left(- \frac{r_s^2}{4 D_T t} \right) \right] .$$

This equation describes the predicted arrival time spectrum of an ion

which undergoes only depleting reactions. A detailed comparison of this equation with the experimental arrival time spectrum gives a measure of the longitudinal diffusion coefficient D_L, provided all other parameters in the equation are known. This procedure will be briefly described here.

An experimental run usually consists of arrival time spectra taken at four different drift lengths. From these spectra the drift velocity is determined. This measured drift velocity is substituted into Equation (5-1). The drift tube exit aperture area a, drift distance r, and ion source exit aperture radius r_s are known dimensions of the apparatus. The source ion density s is unknown; however, the dependence on s is eliminated by normalizing the heights of the experimental and theoretical spectra to the same value. Moseley [27] has shown that α and D_T drastically change the intensity of $\Phi(z,t)$ but have little effect on the shape of the arrival time spectrum. The intensity dependence on α and D_T is removed by the normalization procedure. Diffusion measurements are made at pressures such that reactions are minimized (see Chapter IV) and α is set equal to zero. The value of D_T used is from the Wannier equations and will be discussed later in this chapter. The only unknowns left in Equation (5-1) are D_L and t. The time difference between channels of the experimental arrival time spectrum is well known. The time corresponding to the start of the first channel is the sum of the delay time DLY and the analysis time t_A and will be designated as time Tl. The time corresponding to the center of the k^{th} channel of the analyzer is given by

$$t_K = DLY + t_A + (k - \tfrac{1}{2})\ c.w. = T1 + (k - \tfrac{1}{2})\ c.w. \qquad (5\text{-}2)$$

Since the analysis time t_A is an average value for the four spectra, it is necessary to make slight adjustments in the T1 value when fitting each spectrum. The values of T1 and D_L are adjusted to obtain a best fit, in the least squares sense, between the experimental arrival time spectrum and the theoretical arrival time spectrum $\Phi(z,t)$. Comparisons of such fits for H^+, H_3^+, and H^- have previously been shown in Figures 9, 12, and 18 respectively. The values of D_L obtained for each arrival time spectrum are used to calculate a best value for the run at the particular experimental conditions of P, E/N, and T. These four values normally cluster around an average value with a spread of less than 5 percent. However, under certain conditions a steady trend toward larger values of D_L is observed for decreasing drift distances. This trend is caused by the ions being gated into the drift region with energies above the equilibrium value. The net effect is to create the ions a short distance inside the drift region with an initial diffusion. At shorter drift distances this initial diffusion becomes more noticeable and at sufficiently long drift distances the effect becomes negligible. This initial diffusion can be accounted for by assuming a source term like Equation (3-69) with an initial z-diffusion. The solution to the transport equation with this initial diffusion has been discussed in Chapter III. The solution is identical to Equation (5-1) with $4D_Lt$ replaced with $4D_Lt + z_s^2$ whereever it appears. Thus

when a trend toward higher D_L is noted a "best" value can be obtained in either of two ways. The value of z_s can be adjusted such that the D_L all cluster about an average value, or the value of D_L obtained at the longest drift distance can be used. The first method being somewhat artificial, the second is used in the present research.

Comparison with Theory

The longitudinal diffusion coefficient D_L is inversely proportional to N. To facilitate comparison between values of D_L measured at different pressures it is customary to use the value ND_L which is independent of pressure.

In the low field region the diffusion coefficients D, D_L, and D_T are equal and may be compared with the mobility K through the Einstein relation

$$K = \frac{e}{kT} D \ . \tag{5-3}$$

Since both K and D are inversely proportional to N we can use the ideal gas law, the definition of K_o, and the Einstein relation to obtain

$$ND = \frac{T(760)}{3(273.16)} K_o(0) \tag{5-4}$$

$$= (2.315 \times 10^{15}) \ T \ K_o(0)$$

where T is in °K and N is in cm^{-3}. Here $K_o(0)$ is used instead of K_o

to emphasize that this relation is true only in the low field region.

Above the low field region the ions are not in equilibrium with the gas and the velocity distribution is unknown. Under these conditions there is no simple reation, such as the Einstein equation, connecting the mobility and diffusion coefficients.

Wannier [9] has derived formulas for D_L and D_T under the assumption of a $1/r^4$ potential and, separately, for the case of isotropic scattering. For the polarization potential, $V(r) = -\alpha e^2/2r^4$, the equations are

$$D_L = \frac{M + m}{Mm} 0.905\ \tau_s kT \tag{5-5}$$

$$+ \frac{1}{3} \frac{(M + m)^3(M + 3.72m)}{M^2m(M + 1.908m)} \left(\frac{eE}{m} \right)^2 (0.905\tau_s)^3$$

and

$$D_T = \frac{M + m}{Mm} 0.905\ \tau_s kT \tag{5-6}$$

$$+ \frac{1}{3} \frac{(M + m)^4}{M^2m(M + 1.908m)} \left(\frac{eE}{m} \right)^2 (0.905\tau_s)^3.$$

Here α is the polarizability of the gas molecule, m and M are the ionic and gas masses, respectively, and τ_s is the mean free time between collisions of the ion with gas molecules. A direct consequence of the $1/r^4$ potential is a constant mean free time between collisions τ_s,

where the subscript s refers to spiraling collisions. The parameter τ_s is not experimentally observable; however, we may relate it to the observable zero field mobility K(0) by the following procedure. In the limit of low fields Equations (5-5) and (5-6) must reduce to the rigorous Einstein relation. In the low field limit, $E \rightarrow 0$, the second terms on the RHS of Equations (5-5) and (5-6) become zero and we can write

$$D_L(0) = D_T(0) = D(0) = \frac{M + m}{Mm} (0.905\tau_s)\, kT \qquad (5\text{-}7)$$

$$= \frac{K(0)kT}{e} = \frac{v_d kT}{eE} ;$$

thus $$(0.905\tau_s) = v_d \frac{Mm}{(M + m)eE} = K(0) \frac{Mm}{(M + m)e} . \qquad (5\text{-}8)$$

Using this equation to eliminate $(0.905\tau_s)$ in Equation (5-5) and multiplying by N to obtain the pressure independent ND_L we obtain

$$ND_L = ND(0) + \frac{(M + 3.72m)M}{3(M + 1.908m)e} (K(0)^3 E^2 N) \qquad (5\text{-}9)$$

It is often more convenient to relate the drift velocity to the reduced mobility and write

$$ND_L = K_o(0) \frac{(760)T}{(273.16)e} \qquad (5\text{-}10)$$

$$+ \frac{1}{3} K_o(0)^3 \frac{(M + 3.72m)M}{(M + 1.908m)ek^3} \frac{(760)^3}{(273.16)^3} (E/N)^2$$

Here by using $K_o(0)$ we explicitly point out that the constant mean free time between collisions has been evaluated in the low field region. The value thus obtained for τ_s, in terms of the constant $K_o(0)$ is then substituted into Equation (5-5). In the low field region Equation (5-10) reduces to the Einstein relation (see Equation (5-4)). In the high field region Equation (5-10) predicts ND_L to vary as $(E/N)^2$.

This equation is strictly true only for a $1/r^4$ potential. In actuality the interaction between the ions and gas molecules cannot be described by only a $1/r^4$ term and the mean free time between collisions is not in general constant but a function of E/N. The form of Equation (5-10) suggests an immediate way to remove some of the model dependence and to obtain τ_s as a function of E/N. This is accomplished by replacing $K_o(0)$ with $K_o(E/N)$, the value of K_o at the specific E/N of the measurement. This is equivalent to using Equation (5-8) over all ranges of E/N to determine a relation between τ_s and v_d. This is of course not strictly valid since Equation (5-8) was derived under the hypothesis of low fields; it is merely an approximate correction to τ_s. Numerically Equation (5-10) reduces to

$$ND_L = K_o(E/N)T(2.315 \times 10^{15}) \qquad (5\text{-}11)$$

$$+ K_o(E/N)^3 \frac{(M + 3.72\ m)M}{(M + 1.908m)} (6.701 \times 10^{11}) (E/N)^2$$

where m and M are expressed in amu, T in °K, E/N in Td, K_o in $cm^2/V \cdot sec$, and ND_L in $cm^{-1} \cdot sec^{-1}$. The explicit dependence of K_o on E/N is indicated by writing $K_o(E/N)$.

Recently additional corrections to D_L and D_T have been derived by Whealton and Mason [52] and independently by Robson[53]. The derivation by Whealton and Mason is based on kinetic theory whereas that by Robson is based on nonequilibrium thermodynamics. These corrections are

$$D_L' = D_L \left(1 + \frac{d\ln K}{d\ln E}\right) \tag{5-12}$$

and

$$D_T' = D_T \left(1 - c \frac{d\ln K}{d\ln E}\right) \tag{5-13}$$

where c is a constant on the order of 1/3. For our purposes we express Equation (5-12) in terms of pressure independent quantities and obtain

$$ND_L' = ND_L \left(1 + \frac{(E/N)}{K_o(E/N)} \frac{dK_o(E/N)}{d(E/N)}\right) \tag{5-14}$$

This equation will be called the Whealton-Mason equation throughout this thesis. The quantity ND_L preceding the term in parentheses is from Equation (5-11) and includes the explicit dependence of τ_s on E/N, or equivalently K_o on E/N.

Experimental Results

The experimentally measured coefficients ND_L are plotted as a function of E/N at 300°K and numerical results are tabulated in Appendix

II. The experimental points are the best values for ND_L and are plotted as solid circles. The three solid curves correspond to the theoretical predictions of Equations (5-10), (5-11), and (5-14) and will be identified under the discussion of the specific ion. The value above the theoretical curve is the value of ND_L in the low field limit predicted by the Einstein equation in the form of Equation (5-4). The units of this value are the same as those on the ordinate of the respective graphs.

H^+

The values of ND_L have been measured for H^+ in H_2 over a range of 4 to 100 Td and are presented graphically in Figure 19. From Equation (5-4) the predicted value for ND_L in the limit of zero field is 11.1×10^{18} $cm^{-1} \cdot sec^{-1}$. This is based on a value $K_o(0) = 16.0$ $cm^2/V \cdot sec$. The three solid curves are the theoretical predictions of Equations (5-10), (5-11), and (5-14). The upper curve corresponds to Equation (5-10) where a constant mean free time between collisions is assumed. The center curve corresponds to Equation (5-11) where the mean free time between collisions is calculated for the specific E/N from Equation (5-8). The dependence of the theoretical calculation of ND_L on $K_o(E/N)$ is apparent. Since $K_o(E/N)$ decreases for increasing E/N (for H^+ in H_2 see Figure 8) this curve falls below the curve plotted with the constant value $K_o(0)$. The lowest curve corresponds to Equation (5-14) where the Whealton-Mason correction has been applied to Equation (5-11). Again the dependence of the theoretical calculation on the shape of $K_o(E/N)$ is apparent. The slope of $K_o(E/N)$ vs. E/N is negative for E/N greater than $\sim$ 10 Td. Thus the derivative of $K_o(E/N)$ with

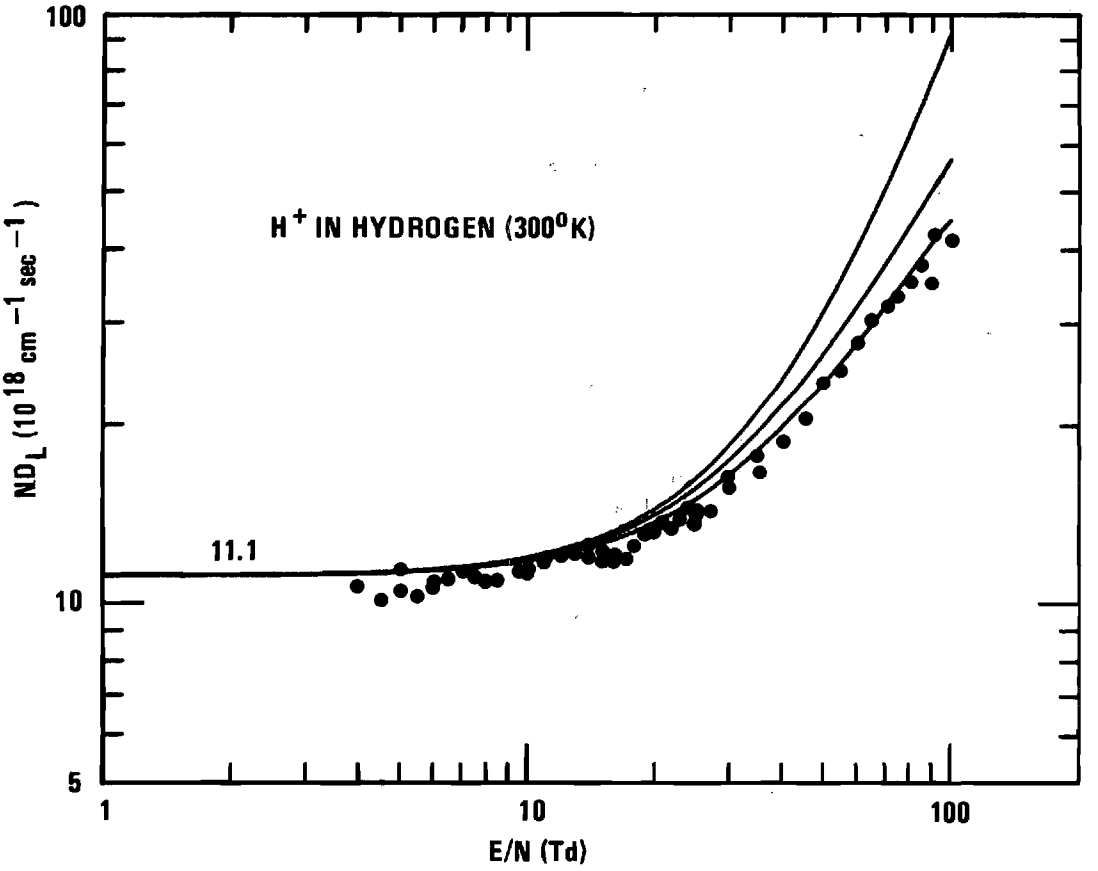

Figure 19. Longitudinal Diffusion Coefficients of H^+ Ions in H_2 Gas at 300°K as a Function of E/N.

respect to E/N is negative and the correction term in Equation (5-14) reduces the value of ND_L. The agreement between this curve and the experimental data is good over the entire range of E/N. The experimental values fall slightly below the theoretical prediction at low E/N and this effect is attributed to experimental error. The values of ND_L measured at different drift distances show no trend toward larger values at short drift distances. The values generally cluster around some average value with less than 3 percent mean deviation. The value of ND_L obtained at the longest drift distance is still considered the best value and it is the value plotted graphically and tabulated in the appendix.

H_3^+

The values of ND_L have been measured for H_3^+ in H_2 over a range of 4.5 to 85 Td and are presented graphically in Figure 20. Based on a value of $K_o(0) = 11.3\ cm^2/V\cdot sec$ the predicted low field value of ND_L is $7.85 \times 10^{18}\ cm^{-1}sec^{-1}$. The three curves are again the theoretical predictions of Equations (5-10), (5-11), and (5-14). In contrast with H^+ in H_2, $K_o(E/N)$ increases as a function of E/N for H_3^+ in H_2 over the range considered here. In this case the corrections used in Equations (5-11) and (5-14) will both be positive. The lowest curve corresponds to the constant mean free time model, Equation (5-10). Above ~ 30 Td $K_o(E/N)$ increases rapidly. The center curve corresponds to Equation (5-11) and the uppermost curve is the curve with the Whealton-Mason correction. The best agreement is again with the Whealton-Mason curve; However, the agreement here is not overall as good as with H^+ in H_2.

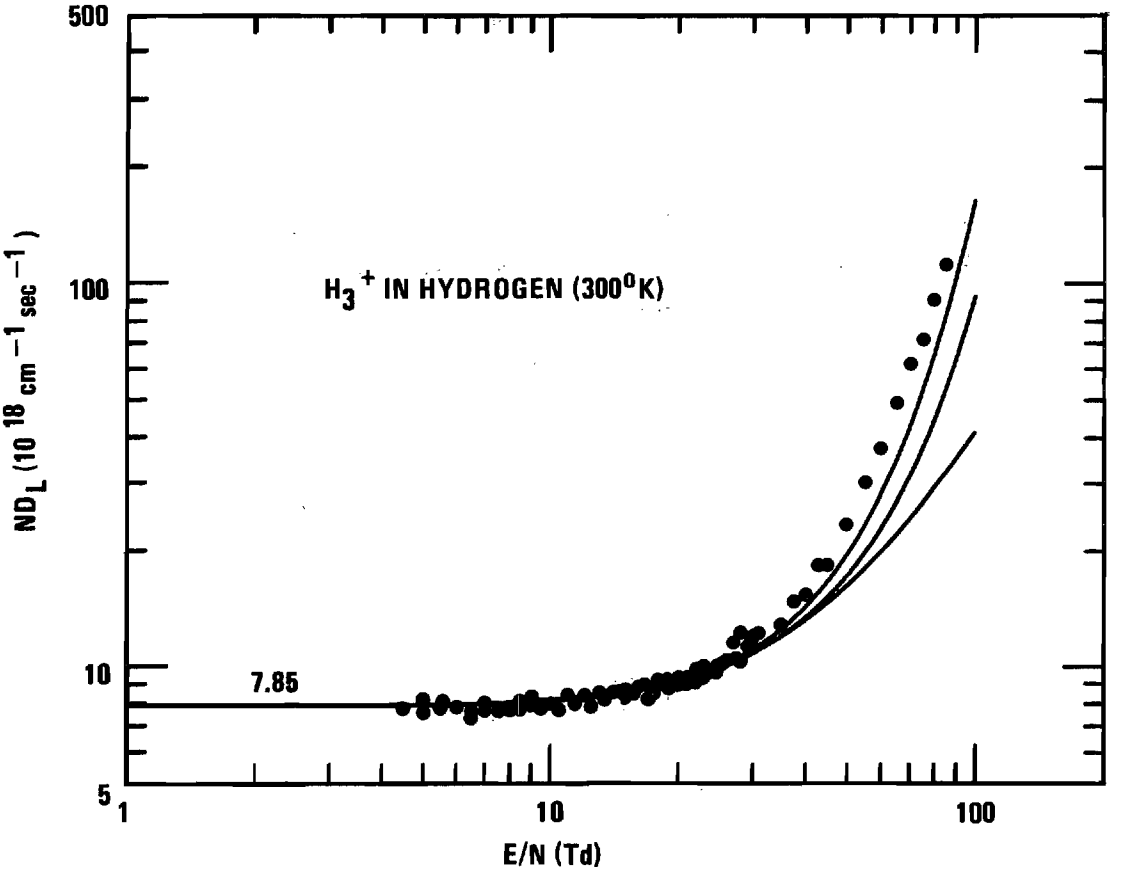

Figure 20. Longitudinal Diffusion Coefficients of H_3^+ Ions in H_2 Gas at 300°K as a Function of E/N.

The low field values are in excellent agreement with the theoretical predictions, but at higher values of E/N the measured values begin to break away from the theoretical (Whealton-Mason) curve. This break-away is considered to be real and not due to experimental error. The values of ND_L measured at the four different drift distances show no consistent trend toward larger values at short drift distances. In almost every instance the scatter among the values is less than 3 percent.

H^-

The longitudinal diffusion coefficients have been measured for H^- in H_2 over a range of 2.5 to 70 Td. These results are plotted in Figure 21 and tabulated in Appendix II. The low field value of ND_L is calculated to be 2.99×10^{19} $cm^{-1} \cdot sec^{-1}$ from a value of $K_o(0)$ of 43.0 $cm^2/V \cdot sec$. The three curves, top, center, and bottom, are based on Equations (5-10), (5-11), and (5-14), respectively. The data above values of E/N of ~ 30 Td are not of sufficiently good quality to show preference toward any one of the three theoretical curves over another. Since the general shape of $K_o(E/N)$ vs. E/N for H^- in H_2 is the same as for H^+ in H_2, the three theoretical curves have the same trend as those for H^+ in H_2.

The values of ND_L measured at the different drift lengths show a definite trend toward larger values at shorter drift lengths. This effect is attributed to an initial diffusion of the ions as previously discussed. The values of ND_L plotted and tabulated are those for the longest drift distance during the measurement. This effect could be minimized by operating at higher pressures. This would act to

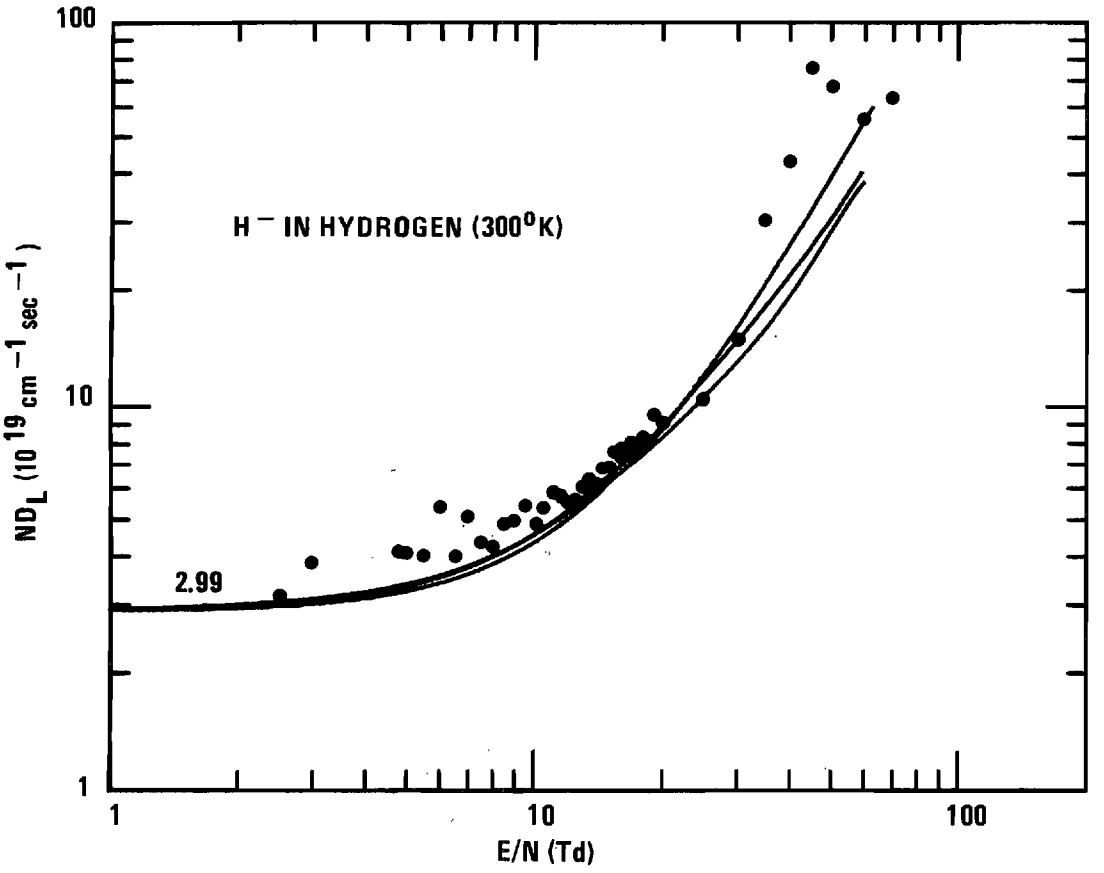

Figure 21. Longitudinal Diffusion Coefficients of H^- Ions in H_2 Gas at 300°K as a Function of E/N.

thermalize the ions more rapidly and to reduce the initial diffusion. For example, the run at an E/N of 2.5 Td was taken at a pressure of 750 microns and the ND_L measured at the longest drift distance is in close agreement with the Einstein value. The data between 10 and 20 Td show fair agreement with theory; however, data outside this region agree poorly with theory and exhibit only the general trend of the theoretical predictions.

Deuterium Ions

Longitudinal diffusion coefficients have been measured for D^+, D_3^+, and D^- in D_2. Because of the similarity with the measurements of H^+, H_3^+, and H^- these results are merely tabulated in Appendix II and will not be plotted or discussed.

Error Analysis

Longitudinal diffusion coefficients are measured by a detailed curvefit of Equation (5-1) to experimental arrival time spectra. These spectra are taken at known measured values of the experimental parameters: pressure P, temperature T, drift distance z, and electric field intensity E. From the measured values of D_L, P, and T the pressure independent value ND_L is calculated. This calculated value of ND_L refers to specific values of the temperature and E/N. Errors in the measured value of ND_L arise from three major sources: (1) Errors in the dependent variables used in Equation (5-1), (2) Errors in the measured experimental parameters P, T, and E, and (3) Errors due to the quality of the curve fitting procedure itself. Each of these sources of error will be considered separately.

The physical dimensions of the apparatus a, r_s and z are known very accurately and are not an appreciable source of error in the present measurements. The transverse diffusion coefficient D_T appears in Equation (5-1) only through the term

$$\left[1 - \exp\left(-\frac{r_s^2}{4D_T t}\right)\right]. \qquad (5\text{-}15)$$

This term is primarily an attenuation term; however, by normalizing the heights of the experimental and theoretical spectra to the same value both the dependence on D_T and the source ion density s is removed. If this normalization procedure is used, the value of D_T can be varied over one order of magnitude and have less than 1 percent effect on the measured value of D_L. The value of D_T in the curve fitting procedure is thus not critical and the value used is from the Wannier Equation (5-6). The reaction frequency α is set equal to zero in the cruve fitting procedure. If diffusion measurements are made at low pressures, any possible reaction effects are minimized and any small effects which may remain are eliminated to first order by the normalization procedure. The primary source of error is due to errors in the measured drift velocity. Schummers[32] has shown that small variations in v_d result in variations in the measured D_L that are approximately three times as large. Thus a 1 percent change in v_d used in Equation (5-1) results in a 3 percent change in the measured value of D_L. The errors in the drift velocity for H^+ and H_3^+ ions in H_2 are ± 1.15 percent and the corresponding error bounds for D_L are ± 4.53 percent.

Errors in the measured values of P, T, and E also affect the

measured values of ND_L. The effect of these parameters is different in the low and high field regions and is difficult to evaluate. The best indication of how errors in these values affect ND_L is obtained by examining the theoretical predictions of Equation (5-10). In the low field region we have

$$ND_L = K_o(0) \frac{(760)T}{(273.16)e} \tag{5-16}$$

Thus even though $K_o(0)$ depends only weakly on T, ND_L is directly proportional to T. The measurements of ND_L are made at room temperature, which is close to 300°K. To facilitate comparison between values of ND_L taken at slightly different temperatures, all values plotted and tabulated in Appendix II have been normalized to 300°K. It should be noted that this is an additive correction and is made only to the low field component of ND_L.

The error in the temperature measurement is considered to be ± 0.53 percent. Thus in the low field region the possible effect on ND_L is ± 0.53 percent. Small variations in the value of E/N can also change the longitudinal diffusion coefficients. In the low field region ND_L is constant and any variation in E/N only affects the value of v_d whose error has already been considered. In the high field region, however, there is an additional error associated with errors in E/N. From Equation (5-10) the values of ND_L vary according to $(E/N)^2$ in the high field region. The accuracy of E/N is considered to be ± 1.26 percent and the corresponding effect on ND_L in the high field region is ± 2.52 percent. Since ND_L is pressure-independent,

there is no direct error associated with the accuracy of the measured number density. For example if N were in error by 1 percent, the measured value of D_L would also be in error by 1 percent, but in the opposite direction. Thus to first order these effects cancel.

When fitting a theoretical curve to an experimental curve it is necessary to have a parameter which indicates the quality of agreement between the two curves. In the present case this parameter is the root mean square value of the difference between the theoretical and experimental arrival time spectra. The rms value has a sharp minimum as a function of the measured parameter D_L. For example a ± 5 percent change in the D_L value from the "best" fit value causes a change in the rms parameter of greater than 100 percent. The quality of this fit of course depends upon the quality of the experimental arrival time spectrum; the more ions that are detected the smaller the random scatter of the experimental data. The present spectra are taken in such a manner that the peak of the experimental spectra corresponds to a height of 2^{12} or 4096 counts. The best indication of random scatter in measurements of ND_L is the scatter among the values measured at the different drift distances during a specific run and also the scatter among the values at the same E/N during different runs. The scatter among the values of ND_L during one run is considered to be ± 3.0 percent for both H^+ and H_3^+. The overall scatter between best values of ND_L at low E/N for different runs gives an indication of the mangitude of end effects and initial diffusion. This scatter is considered to be ± 7.0 percent for H^+ and ± 4.0 percent for H_3^+.

These individual sources of error are considered to be independent

and the best estimate of probable error is obtained by combining them in a square root of the sum of the squares fashion. For H^+ this yields a probable error bound of ± 8.9 percent and ± 9.2 percent in the low and high field regions, respectively; and for H_3^+ ± 6.8 percent and ± 7.2 percent in the low and high field regions, respectively.

The measured values of ND_L for H^- in H_2 show a definite trend toward larger values at shorter drift distances. Since the values do not cluster around an average value it is impossible to give an estimate of the actual value of ND_L or a reasonable error bound. As previously mentioned this trend is caused by an initial diffusion of the ions and "best" values of ND_L can be obtained by going to sufficiently long drift distances or adjusting the initial diffusion z_s such that the measured values all cluster around an average value. To determine how well this latter procedure would work, a sample calculation was made at an E/N of 5.45 Td where the Einstein relation is known to be valid. The initial diffusion was adjusted for the arrival time spectrum taken at position 4, the closest position, such that the measured value of ND_L was that predicted by the Einstein relation. Using this value of z_s the values of ND_L were remeasured at positions 7, 6, and 5. The three values thus obtained clustered around the "correct" Einstein value.

Because of the effects of initial diffusion no error is quoted for H^- in H_2.

CHAPTER VI

REACTIONS

The reaction frequency per ion has been measured for the conversion of H^+ ions into H_3^+ ions by reaction with the H_2 gas molecules and for the conversion of D^+ to D_3^+ by reaction with D_2. Because of the similarity of the reactions only hydrogen will be discussed. These measurements clearly indicate the reaction to be three-body and of the form

$$H^+ + 2H_2 \rightarrow H_3^+ + H_2 \ . \qquad (6\text{-}1)$$

The rate coefficient k is related to the reaction frequency α by the equation

$$\alpha = kN^2 \ . \qquad (6\text{-}2)$$

The reaction frequency is measured as a function of E/N and pressure over the range of 25 to 50 Td and from 250 to 500 microns respectively. Over this range of E/N the rate coefficient is constant.

Experimental Procedure

There are two basic methods of measuring reaction rates which can be used with the present apparatus. The attenuation of the parent ionic species, in this case H^+, can be measured as a function of drift length.

Miller [2,31] has used this method to determine the rate coefficient of reaction (6-1). The main drawback of this procedure is that it requires the source intensity to remain constant over relatively long periods of time. The other method used is the detailed fitting of the product ion arrival time spectrum, in this case the H_3^+ spectrum, to the theoretical prediction for the spectrum. This is the method used in the present research and the advantages and drawbacks of this procedure will be discussed in detail.

Equations (3-74) and (3-75) describe the arrival time spectra of ionic species undergoing fore-back reactions of the form:

$$A \underset{\alpha_{AB}}{\overset{\alpha_{BA}}{\rightleftharpoons}} B \tag{6-3}$$

Although it is immaterial as to which subscript refers to which ion we shall let species A refer to H^+ and species B refer to H_3^+. In the present case species B, H_3^+, does not break up to form species A, H^+. This is readily apparent from the arrival time spectrum of H^+. We may thus set the coefficient $\alpha_{AB} = 0$ and the predicted arrival time spectrum of H_3^+ is given by Equation (3-86)

$$\Phi_B(z,t) = as \int_o^t \frac{du}{(\pi r_L^2)^{\frac{1}{2}}} \left\{ f_B\, \delta(t-u) + f_A\, \alpha_{BA} \right\} \tag{6-4}$$

$$\times \left\{ \left[2D_{LB} \frac{(z-r_d)}{r_L^2} \right] + v_{dB} \right\} \exp \left[- \gamma - \frac{(z-r_d)^2}{r_L^2} \right]$$

$$x \left[1 - \exp \left(- \frac{r_s^2}{r_T^2} \right) \right]$$

where

$$r_T^2 = 4D_{TA}(t-u) + 4D_{TB}u \ , \tag{6-5a}$$

$$r_L^2 = 4D_{LA}(t-u) + 4D_{LB}u \ , \tag{6-5b}$$

$$r_d = v_{dA}(t-u) + v_{dB}u \ , \tag{6-5c}$$

$$\gamma = \alpha_A(t-u) + \alpha_B u \ . \tag{6-5b}$$

In the present situation two other simplifications can be made. Since H^+ reacts to form only H_3^+, the coefficient $\alpha_A = \alpha_{BA}$, and since H_3^+ does not appreciably react to form anything else we have $\alpha_B = 0$.

If it were possible to produce only H^+ ions in the source, a further simplification could be made by setting $f_B = 0$; however, H^+ ions cannot be produced in the source without also producing H_3^+ ions. As previously discussed in Chapter IV, the best that can be accomplished is to optimize the ratio between H^+ and H_3^+.

The ions are created in the source, and both species are gated into the drift region at the same time. As the two ionic species drift they separate because of their different drift velocities, the H^+ ions moving ahead of the H_3^+ ions. As the H^+ ions move ahead they also react with the gas to produce H_3^+ ions. This reaction creates a

"foot" on the H_3^+ arrival time spectrum extending toward earlier times. Figure 22 shows a typical H^+ arrival time spectrum (histogram) used to determine reaction rate coefficients and the analytic fit (smooth curve) given by Equation (6-4). The large peak is due to H_3^+ ions which are produced in the source and which traverse the whole length of the drift region as H_3^+ ions. The front "foot" extending to earlier times is due to H_3^+ ions reaction-produced from H^+ ions.

In Chapter III approximation schemes were discussed which enabled the reaction coefficient α to be determined by examination of the reaction-produced "foot" of the arrival time spectrum. It was shown that when $\alpha_B = \alpha_{AB} = 0$ and if: (1) $(v_{dA} - v_{dB})t >> (4D_{LAt} + 4D_{LB}t)^{\frac{1}{2}}$ and if (2) $D_{TA}/v_{dA} = D_{TB}/v_{dB}$, then the smooth upward sloping part of the foot could be fitted by the very simple formula

$$\frac{\partial \ln \Phi_B}{\partial t} = \frac{\alpha_{BA} v_{dB}}{v_{dA} - v_{dB}} \quad . \tag{6-6}$$

Both of these assumptions have physical interpretations that are perhaps easier to visualize if we first consider the ions to react but not diffuse. The H^+ ions are being continually depleted by reactions and the number of H^+ ions remaining at any time τ is given by

$$n_A(\tau) = n_A(0)e^{-\alpha\tau} \tag{6-7}$$

where $n_A(0)$ is the number of A ions at time $\tau = 0$. The number of B ions reaction-produced at a time τ is given by

E/N = 34.78 Td	$v_{dA} = 14.52 \times 10^4$ cm/sec	$v_{dB} = 10.69 \times 10^4$ cm/sec
P = 442.92 microns	$D_{LA} = 1250$ cm^2/sec	$D_{LB} = 995$ cm^2/sec
z = 43.775 cm	$D_{TA} = 1071$ cm^2/sec	$D_{TB} = 664$ cm^2/sec
T1 = 238.0 μsec	$\alpha_A = 6.42 \times 10^3$ sec^{-1}	$\alpha_B = 0.0$ sec^{-1}
c.w. = 1.0 μsec	$\alpha_{BA} = 6.42 \times 10^3$ sec^{-1}	$\alpha_{AB} = 0.0$ sec^{-1}
N = 14.4×10^{15}cm^{-3}	$f_A = 0.442$	$f_B = 0.558$

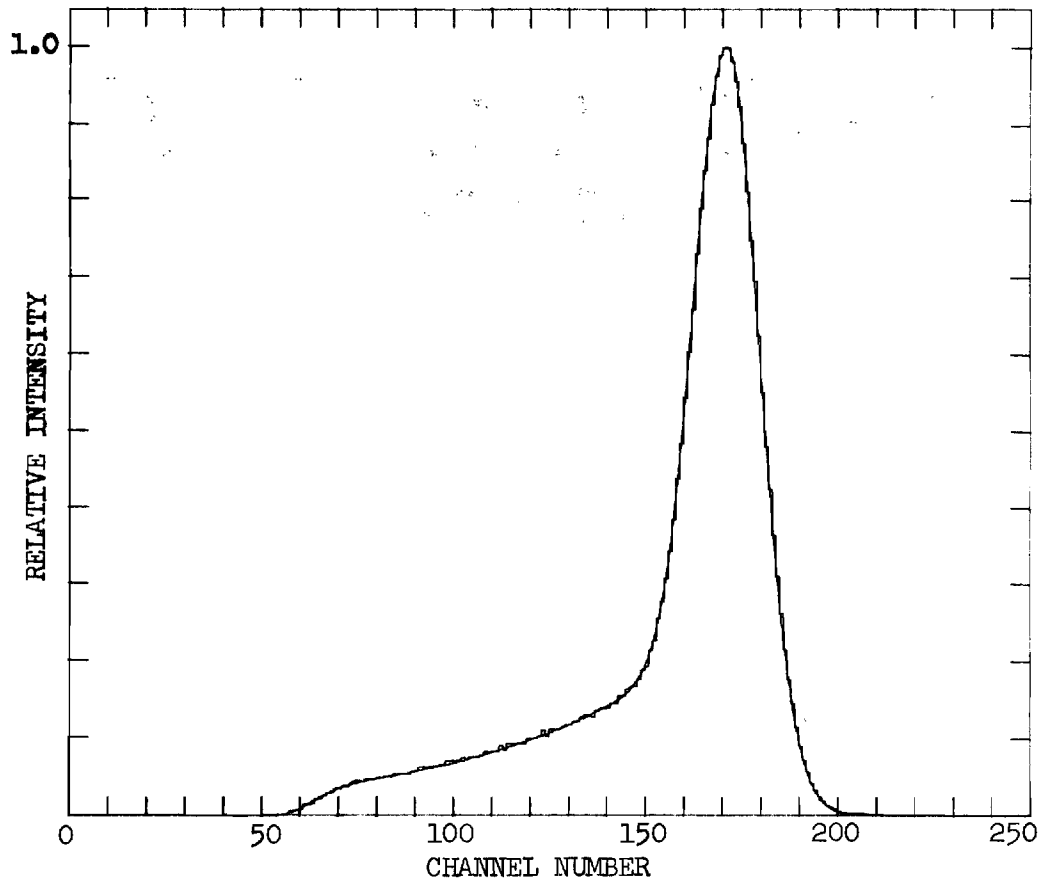

Figure 22. Arrival Time Spectrum for H_3^+ Ions in H_2 Gas at 300°K Showing Reaction Produced Foot and Theoretical Fit.

$$n_B(\tau) = \alpha n_A(\tau) \ . \tag{6-8}$$

The reaction-produced H_3^+ ions are detected at a fixed drift distance z and at a time t. These ions have spent a time u as species B, H_3^+, and a time (t-u) as species A, H^+. We thus have the relation

$$v_{dA}(t-u) + v_{dB}u = z \ . \tag{6-9}$$

The H_3^+ ions detected at time t and drift distance z were produced by reactions of H^+ with the gas at time (t-u). From Equations (6-8) and (6-9) we have

$$n_B(t-u) = \alpha n_A(0)e^{-\alpha(t-u)} \tag{6-10}$$

$$= \alpha n_A(0)e^{-\alpha\left(\frac{z-v_{dB}t}{v_{dA}-v_{dB}}\right)} \ .$$

Since the ions are assumed not to diffuse this is the number of reaction-produced B ions which are detected at a time t and drift distance z. Taking the natural logarithm of Equation (6-10) and differentiating with respect to time yields Equation (6-6). The net result of assumptions (1) and (2) is to require that diffusion not distort the reaction-produced part of the arrival time spectrum. In practice, by staying away from the rounded edges of the reaction-produced foot and fitting only the smooth upward sloping part of the foot to Equation (6-6),

reasonable reaction frequency coefficients α can be determined.

Equation (6-6) was used to determine the reaction frequency for converting H^+ to H_3^+ and the rate coefficients k are tabulated in Appendix III. The measured rate coefficients showed a slight pressure dependence indicating that the two assumptions were not entirely satisfied. To eliminate these effects the exact solution given by Equation (6-4) was fitted to the arrival time spectrum.

Equation (6-4) has as dependent variables the drift velocities, diffusion coefficients, and reaction rates of both ionic species. In addition it depends upon the relative abundance of each ionic species, the source intensity, and physical parameters inherent to the experimental apparatus used. The drift velocities and longitudinal diffusion coefficients have been experimentally measured as a function of E/N, by the methods described in Chapters IV and V. The transverse diffusion coefficients are not directly measured, and the values used in the curve-fitting scheme are obtained from the Wannier Equation (5-6) where τ_s has been replaced with v_d through Equation (5-8). Since the shape of the arrival time spectrum is not appreciably affected by transverse diffusion, an estimate is sufficient to obtain good curve fits. The drift length z, the source radius r_s, and the drift tube exit aperture area a are known dimensions of the apparatus. The only unknown parameters remaining in Equation (6-4) are the source intensity s, the relative intensities of each ion f_A and f_B, and the reaction frequency α_{BA} (recall $\alpha_A = \alpha_{BA}$ and $\alpha_B = 0$). The dependence on the source intensity s is removed by normalizing the areas underneath the experimental spectrum and theoretical spectrum to the same value. It should be

noted that the analysis does not depend upon the source intensity being constant in time.

The time difference between any two channels of the time-of-flight analyzer is known very accurately; however, the time corresponding to the start of the analyzer is only known approximately because the analysis time is unknown. To obtain a good fit between the arrival time spectra it is necessary to adjust the time corresponding to the start of the analyzer, T1 (i.e., the time corresponding to the start of channel 1), α_{BA}, and f_A (where $f_B = 1 - f_A$). This procedure will be outlined by showing the arrival time spectrum at each step of the fitting procedure. First, reasonable estimates are made of T1, f_A, f_B, and α_{BA}. Normally T1 is chosen the same as DLY (see Figure 6), f_A and f_B are both set equal to 0.5 and α_{BA} and α_A are set equal to 3×10^3 sec^{-1}. Figure 23 shows the typical fit of the arrival time spectrum (histogram) and the theoretical fit (smooth curve) using these initial estimates. Here we have choosen $\alpha_{BA} = \alpha_A = 2 \times 10^3$ sec^{-1} and $f_A = 0.6$ to accentuate the individual steps taken. To obtain a better estimate of the time T1 the peaks of the two spectra are matched. The peak of the experimental spectrum is determined by averaging the counts in each channel with the four adjacent channels so that fluctuations of the counts in the peak do not result in a mismatch. Figure 24 shows the same theoretical and experimental spectra with the peaks aligned. This coarse alignment matches the peaks within ± 1 channel. Next the heights of the peaks of the two spectra are matched by adjusting f_A and f_B as shown in Figure 25. The foot of the spectra are then fitted by varying α_{BA} and α_A ($\alpha_{BA} = \alpha_A$), as shown in Figure 26. When reaction

E/N = 25.02 Td	$v_{dA} = 10.40 \times 10^4$ cm/sec	$v_{dB} = 7.54 \times 10^4$ cm/sec
P = 344.5 microns	$D_{LA} = 1271$ cm^2/sec	$D_{LB} = 953$ cm^2/sec
z = 43.775 cm	$D_{TA} = 1227$ cm^2/sec	$D_{TB} = 800$ cm^2/sec
Tl = 370.0 μsec	$\alpha_A = 2 \times 10^3$ sec^{-1}	$\alpha_B = 0.0$ sec^{-1}
c.w. = 1.0 μsec	$\alpha_{BA} = 2 \times 10^3$ sec^{-1}	$\alpha_{AB} = 0.0$ sec^{-1}
N = 11.2×10^{15}cm^{-3}	$f_A = 0.600$	$f_B = 0.400$

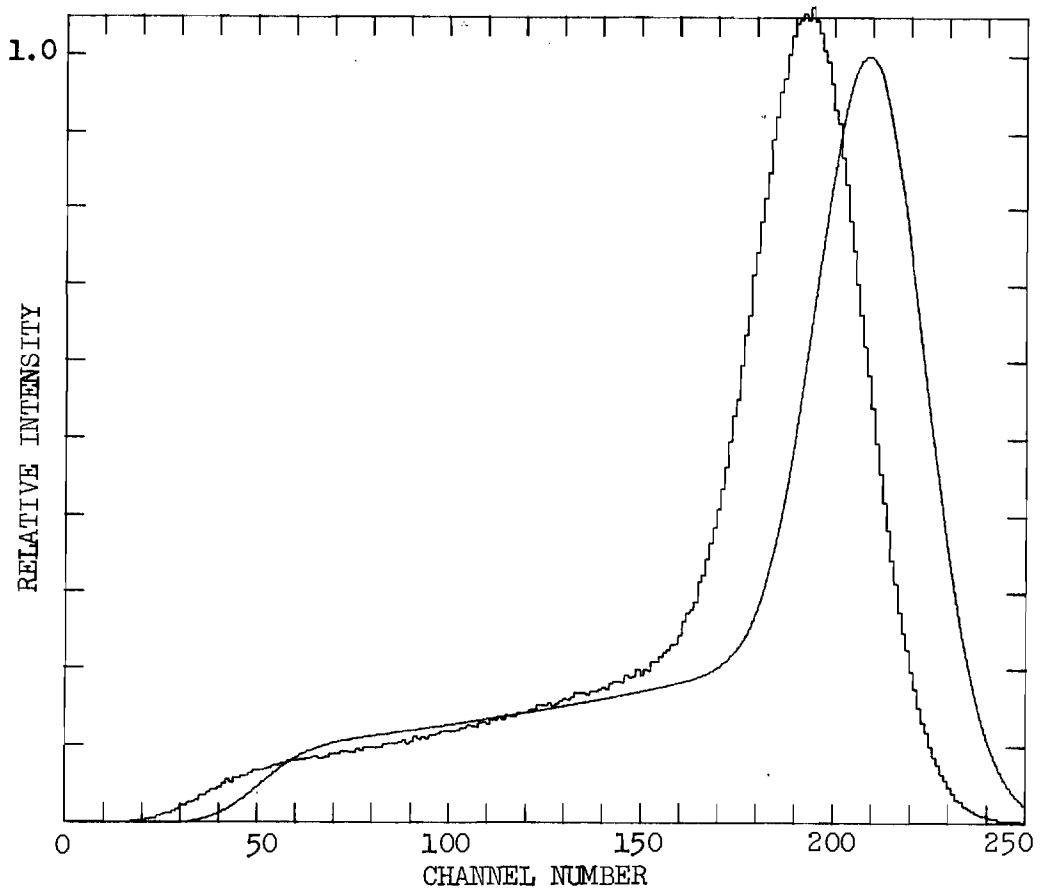

Figure 23. Arrival Time Spectrum for H_3^+ Ions in H_2 Gas at 300°K and Initial Theoretical Fit.

E/N = 25.02 Td	$v_{dA} = 10.40 \times 10^4$ cm/sec	$v_{dB} = 7.54 \times 10^4$ cm/sec
P = 344.5 microns	$D_{LA} = 1271$ cm^2/sec	$D_{LB} = 953$ cm^2/sec
z = 43.775 cm	$D_{TA} = 1227$ cm^2/sec	$D_{TB} = 800$ cm^2/sec
T1 = 385.6 μsec	$\alpha_A = 2 \times 10^3$ sec^{-1}	$\alpha_B = 0.0$ sec^{-1}
c.w. = 1.0 μsec	$\alpha_{BA} = 2 \times 10^3$ sec^{-1}	$\alpha_{AB} = 0.0$ sec^{-1}
N = 11.2×10^{15}cm^{-3}	$f_A = 0.600$	$f_B = 0.400$

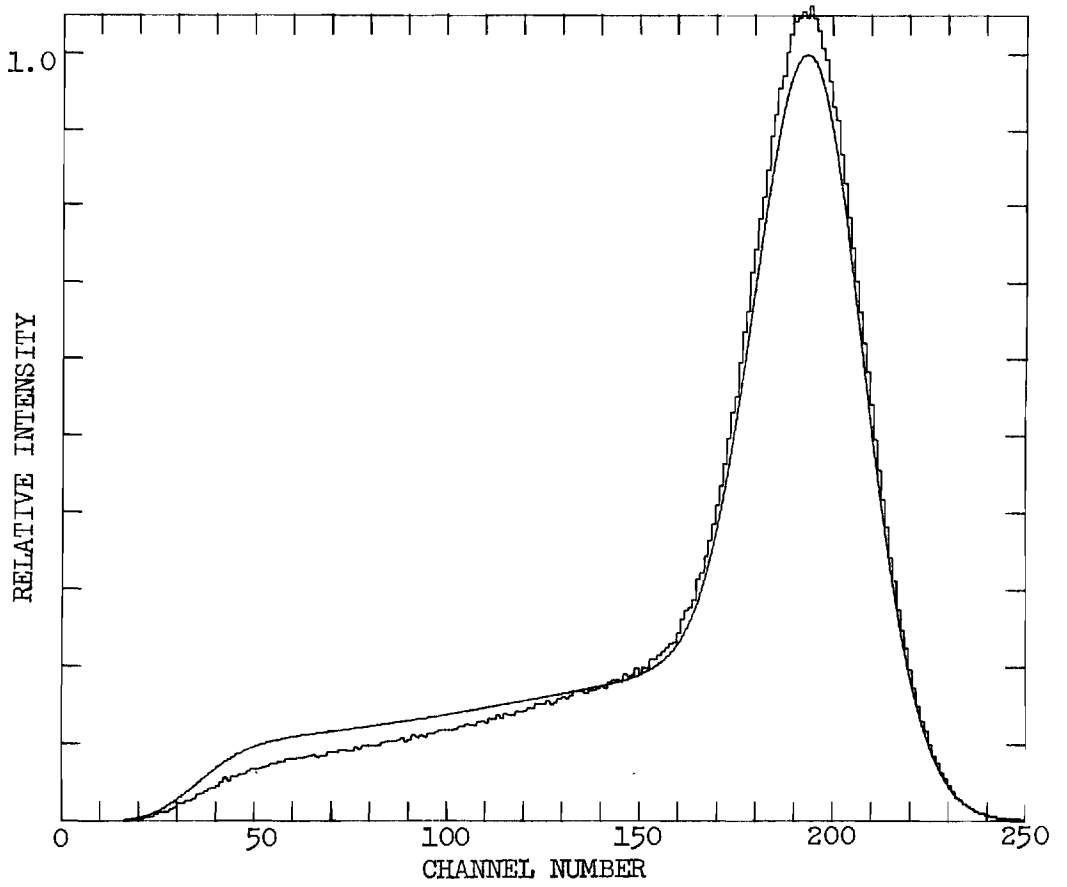

Figure 24. Arrival Time Spectrum for H_3^+ Ions in H_2 Gas at 300°K with the Theoretical Peak Aligned.

E/N = 25.02 Td	$v_{dA} = 10.40 \times 10^4$ cm/sec	$v_{dB} = 7.54 \times 10^4$ cm/sec
P = 344.5 microns	$D_{LA} = 1271$ cm^2/sec	$D_{LB} = 953$ cm^2/sec
z = 43.775 cm	$D_{TA} = 1227$ cm^2/sec	$D_{TB} = 800$ cm^2/sec
T1 = 385.6 μsec	$\alpha_A = 2 \times 10^3$ sec^{-1}	$\alpha_B = 0.0$ sec^{-1}
c.w. = 1.0 μsec	$\alpha_{BA} = 2 \times 10^3$ sec^{-1}	$\alpha_{AB} = 0.0$ sec^{-1}
N = 11.2 x 10^{15}cm^{-3}	$f_A = 0.558$	$f_B = 0.442$

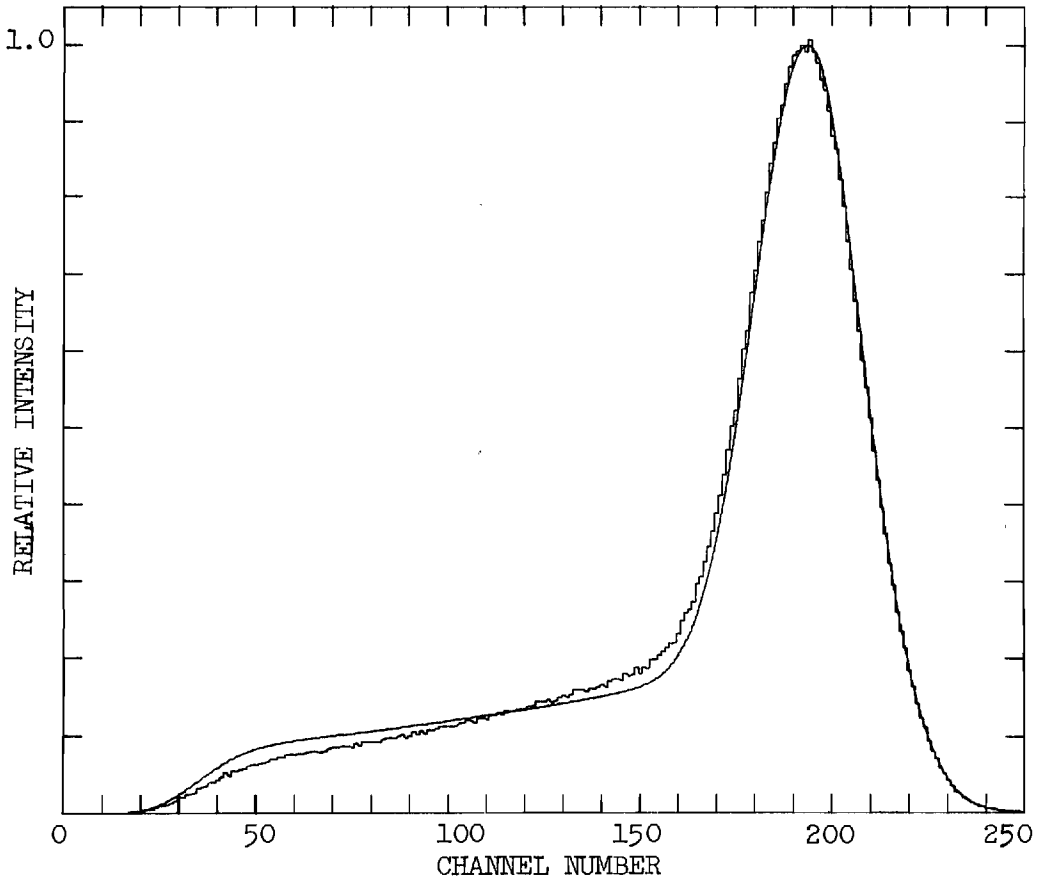

Figure 25. Arrival Time Spectrum for H_3^+ Ions in H_2 Gas at 300°K with Peaks Aligned and Peak Heights Matched.

E/N = 25.02 Td	$v_{dA} = 10.40 \times 10^4$ cm/sec	$v_{dB} = 7.54 \times 10^4$ cm/sec
P = 344.5 microns	$D_{LA} = 1271$ cm^2/sec	$D_{LB} = 953$ cm^2/sec
z = 43.775 cm	$D_{TA} = 1227$ cm^2/sec	$D_{TB} = 800$ cm^2/sec
T1 = 385.6 μsec	$\alpha_A = 3.76 \times 10^3$ sec^{-1}	$\alpha_B = 0.0$ sec^{-1}
c.w. = 1.0 μsec	$\alpha_{BA} = 3.76 \times 10^3$ sec^{-1}	$\alpha_{AB} = 0.0$ sec^{-1}
N = 11.2×10^{15} cm^{-3}	$f_A = 0.504$	$f_B = 0.496$

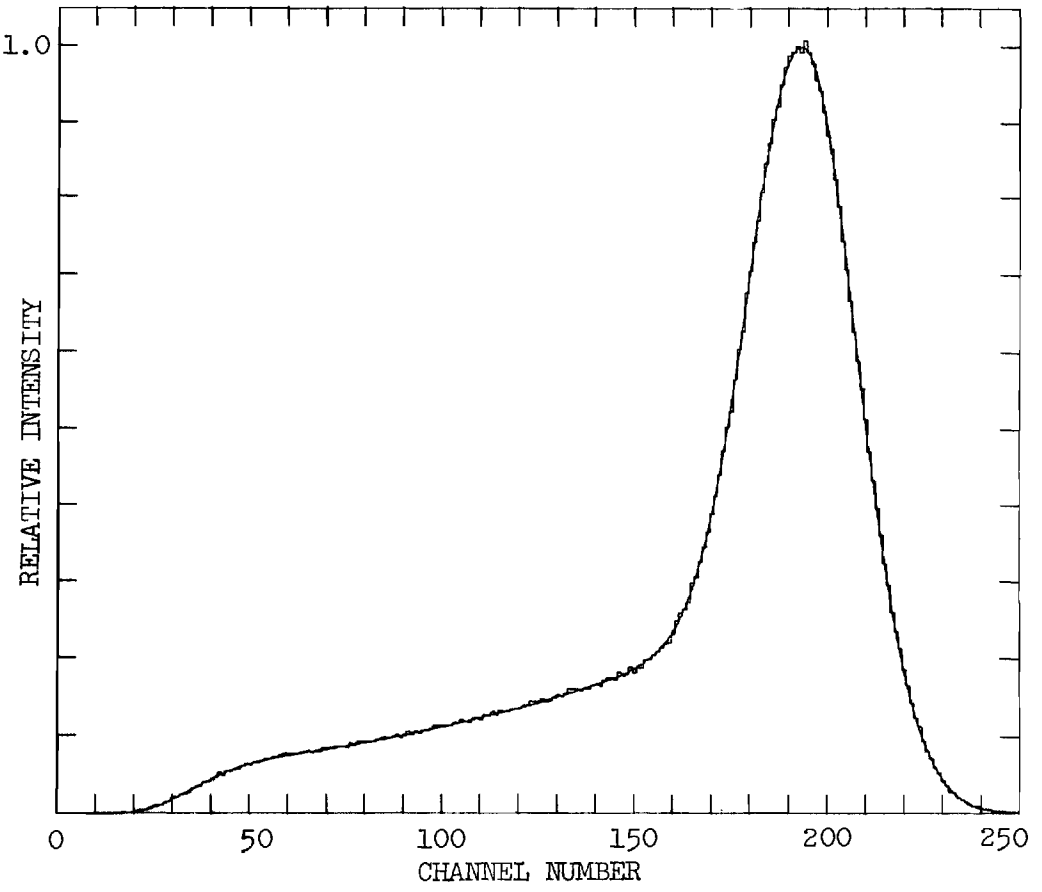

Figure 26. Arrival Time Spectrum for H_3^+ Ions in H_2 Gas at 300°K Showing Reaction Produced Foot and Theoretical Fit.

rates are being determined from the spectra, only the smooth foot part of the experimental spectrum is fitted. In the present example this procedure would correspond to fitting only that part of the spectrum between approximately channels 60 and 150. This method has several advantages. Since the peak of the spectrum is much taller than the foot, a small mismatch of the peak would result in a large least squares error. Also in the foot all of the ions have been reaction-produced and since the areas under the curves are normalized this procedure eliminates both the dependence on s and f_A. Thus the foot matching procedure depends on only one parameter, α_{BA}, and it is adjusted to obtain the best least squares fit of the spectrum to theory.

The foot of the spectrum has been fitted under the assumption that all other parameters except α_{BA} are known. To determine how small variations in the "known" parameters, such as D_{LA}, D_{TA}, v_{dA}, etc., affect the measured reaction rate, these parameters were individually varied and the reaction rate remeasured. It was determined that the reaction rate measurements were insensitive to large variations in D_{TA} and D_{TB}. These coefficients could be varied by ± 10 percent with no appreciable effect on the reaction rate. The coefficients D_{LA} and D_{LB} could also be varied ± 10 percent with no noticeable effect on reaction rate measurements. The fit of the peak of source-produced H_3^+ ions was, however, changed appreciably by varying D_{LB}. Since small changes in D_{LB} had no effect on reaction measurements, the width of the peak was fitted best by varying D_{LB}. This procedure usually resulted in less than 5 percent change in the value of D_{LB}. By successively varying D_{LB} and Tl a very accurate fit of the peak could

be obtained. In the present example this would correspond to fitting the peak in Figure 26 between channels 170 and 250. This procedure has two advantages. It gives a better estimate of D_{LB} for the specific run and a more accurate measurement of Tl. This procedure gives an overall better fit of the complete arrival time spectrum without changing the measured reaction rate.

For a given drift distance z and drift velocity v_{dB}, the peak of the source-produced H_3^+ ions will occur at a known time. By varying Tl the peak is fitted for the given drift velocity v_{dB}. If v_{dB} were to be in error the peak would still be fitted by varying Tl. Using this fitting procedure small errors in v_{dB} are not noticed. On the other hand small variations in v_{dA} cause appreciable change in reaction rate measurements. The length of the foot from the peak is determined by the difference in drift velocities $(v_{dA} - v_{dB})$. Small errors in the difference in drift velocities are apparent from the fit of the end of the foot. In the present example the end of the foot corresponds to the area between channels 20 and 50 of Figure 26. When the spectra exhibit a poor fit in this area, small changes (< 1 percent) are made in v_{dA} to match the experimental and theoretical spectra. In effect this procedure eliminates any errors in the difference of the drift velocities, but any error in v_{dB} remains.

Experimental Results

Reaction rate coefficients were obtained over an E/N range of 25-50 Td and at pressures from 250 to 500 microns. The arrival time spectra of the H_3^+ ions were analyzed by both methods previously

discussed: (1) the matching of the smooth upward sloping part of the foot to Equation (6-6) and (2) the curve fitting of the full expression, Equation (6-4), to the foot.

Using the first method the measured values of k exhibit a slight trend toward smaller values at larger pressures (see Table 18). The value of k determined by this procedure is 3.146×10^{-29} cm^6/sec averaged over 22 values with a standard deviation of $\pm 0.19 \times 10^{-29}$ cm^6/sec or ± 6.04 percent.

The rate coefficient k measured by the second method exhibits no pressure dependent trend and has a smaller deviation between values. The rate coefficient is measured to be 3.049×10^{-29} cm^6/sec over 22 values with a standard deviation of $\pm 0.086 \times 10^{-29}$ cm^6/sec or ± 2.82 percent. The better quality of the results for the second method is attributed to two factors. (1) Small errors in the <u>difference</u> in drift velocities can be eliminated. (2) The curve fitting procedure is not restricted to only the smooth upward sloping part of the foot.

Reaction rate coefficients are in general a function of energy. Ions drifting in a uniform electric field have an approximate average energy given by the Wannier energy Equation (1-9). This equation gives an approximate energy of 0.06 e.V. at an E/N at 25 Td and 0.1 e.V. at an E/N of 50 Td for both H^+ and H_3^+ ions. The rate coefficient k is observed to be constant over this range of E/N and energy.

Miller [2] has previously measured this rate coefficient to be $(3.2 \pm 0.3) \times 10^{-29}$ cm^6/sec for $E/N < 28$ Td. His method involved measuring the attenuation of the parent ionic species, in this case H^+, as a function of drift distance. The agreement between Miller's

measurement and the present measurements is good and within the experimental errors assigned.

The rate coefficient of $D^+ + 2D_2 \rightarrow D_3^+ + D_2$ has also been measured and, within experimental error, is the same as for the corresponding H^+ in H_2 reaction (see Appendix III). Miller has measured this rate to be $(3.0 \pm 0.4) \times 10^{-29}$ cm^6/sec. Again the two results agree within experimental error.

The present procedure of curve fitting the product arrival time spectrum to obtain rate coefficients is restricted to the range of E/N below approximately 50 Td. Above 50 Td the two ionic species do not drift long enough to separate appreciably even at the longest drift distance. Practically this means that the smooth upward sloping part of the foot decreases in width for increasing E/N and finally disappears altogether.

At present there are no theoretical calculations with which to compare the present results.

Error Analysis

Errors in the measurement of the rate coefficient k result from possible errors in the measurement of the reaction frequency α and the gas number density N. The coefficients k and α are related by

$$k = \alpha/N^2 \quad . \tag{6-11}$$

The primary single source of error in k is the error in N. The combined error of P and T result in a possible error in N of ± 1.34

percent (see Table 5). Since $k \sim N^{-2}$, the possible error in k due to error in the number density is ± 2.68 percent.

The possible sources of error in the measurement of α are errors in the dependent variables used in the curve-fitting Equation (6-4) and the random scatter among successively measured values of α. To reduce to a satisfactory level the scatter due to the statistics of the arrival time spectrum, all spectra are taken such that the peak height corresponds to 2^{15} counts. The effect of the larger peak height is apparent when these spectra are compared with the arrival time spectra taken to measure longitudinal diffusion. The latter have a peak height of 2^{12} counts. There is less statistical scatter in the arrival time spectra used to determine reaction rates. There are approximately 2^{12} counts in each channel of the smooth upward sloping part of the foot. A measure of the scatter among the spearate values of k is taken to be the standard deviation of the measured values of ± 2.82 percent.

The effect of errors in the dependent parameters in Equation (6-4) on the measured value of α has already been discussed. The primary source of error is the possible error in v_{dA} and v_{dB}. A 1 percent change in v_{dA} is observed to change the measured value of α by $\sim$ 5 percent. This effect is largely eliminated by adjusting the value of v_{dA} to eliminate mismatches in the end of the theoretical and experimental feet. The possible error remaining due to the difference in the drift velocities is difficult to estimate but is certainly less than ± 2.0 percent. To evaluate the effects of errors in v_{dB} we examine Equation (6-6)

$$\frac{\partial \ln \Phi_B}{\partial t} = \frac{\alpha_{BA} v_{dB}}{v_{dA} - v_{dB}} \quad . \qquad (6\text{-}12)$$

The slope of the foot is a fixed quantity of the arrival time spectrum. As we have already discussed, any errors in the difference of the drift velocities have been removed. Thus, for the moment, we consider the term $(v_{dA} - v_{dB})$ in Equation (6-12) to be a constant, even though v_{dB} may vary. The logarithmic slope of the foot is given by the LHS of Equation (6-12). This slope is a constant for a specific arrival time spectrum. Hence, in Equation (6-12) all the quantities are known except for the product $\alpha_{BA} v_{dB}$. If v_{dB} in the numerator of the RHS of Equation (6-12) is too large, the reaction frequency α_{BA} will be reduced to obtain the same value for the product $\alpha_{BA} v_{dB}$. Thus the effect of an error in v_{dB} is to cause an equal but opposite error in α_{BA}. From Table 5 the error in v_{dB} is considered to be $\pm$ 1.51 percent.

These individual sources of error are considered to be independent and an overall measure of the accuracy of k is determined by the square root of the sum of the squares of the separate errors. This error is evaluated to be $\pm$ 4.7 percent.

CHAPTER VII

CONCLUSIONS

Mobilities

The reduced mobility of H^+ ions in H_2 gas is measured over the range of E/N from 4 to 100 Td and at pressures between 100 and 200 microns. All measurements were made at a gas temperature of approximately 300°K. The reduced mobility exhibits a zero slope below 10 Td and an unambiguous zero-field reduced mobility is measured to be 16.0 $cm^2/V \cdot sec$. Above 10 Td the reduced mobility decreases monotonically, and at 100 Td the reduced mobility has decreased to 13.4 $cm^2/V \cdot sec$.

The reduced mobility of H_3^+ ions in H_2 gas at 300°K is measured over the range of E/N from 4.5 to 85 Td and at pressures from 100 to 300 microns. The reduced mobility exhibits a zero slope below 25 Td and an unambiguous zero-field reduced mobility is measured to be 11.3 $cm^2/V \cdot sec$. Above 25 Td the reduced mobility increases rapidly. At an E/N of 85 Td the reduced mobility has increased to 13.8 $cm^2/V \cdot sec$.

The reduced mobility of H^- ions in H_2 gas have been measured over a range of E/N from 2.5 to 70 Td. These measurements were made at gas pressures between 200 and 750 microns and at a gas temperature of 300°K. Below 15 Td the reduced mobilities have a zero slope and the zero-field reduced mobility is measured to be 43.0 $cm^2/V \cdot sec$. The reduced mobility of H^- in H_2 is approximately 2.7 times as large as the reduced mobility of H^+ in H_2. This discrepancy has not been quantitatively explained at

present. Above an E/N of 15 Td the reduced mobility of H^- in H_2 monotonically decreases and at an E/N of 70 Td the reduced mobility is 37 $cm^2/V \cdot sec$. The overall shape of the reduced mobility vs. E/N curves is the same for both H^+ and H^- in H_2.

The reduced mobility of D^+ in D_2 has been measured over a range of E/N from 6 to 50 Td and at a gas pressure of 200 microns. A zero-field reduced mobility is measured to be 11.7 $cm^2/V \cdot sec$ in the low-field region below 20 Td.

The reduced mobility of D_3^+ in D_2 gas has been measured over a range of E/N from 5 to 50 Td and at gas pressures between 200 and 300 microns. A zero-field reduced mobility is measured to be 8.07 $cm^2/V \cdot sec$ in the low-field region below 20 Td.

The reduced mobility of D^- in D_2 has been measured over a range of E/N from 7.5 to 15 Td at a gas pressure of 300 microns. A zero-field reduced mobility is measured to be 30.1 $cm^2/V \cdot sec$ over this range of E/N.

Longitudinal Diffusion Coefficients

The longitudinal diffusion coefficients have been measured for H^+ ions in H_2 over a range of E/N from 4 to 100 Td. These measurements were made at gas pressures from 100 to 200 microns and at a gas temperature of 300°K. In the low-field region (below 10 Td) the measured values of ND_L agree with the value predicted by the Einstein relation, 11.1×10^{18} $cm^{-1} \cdot sec^{-1}$. As the E/N is increased above the low-field region the values of ND_L increase sharply. At an E/N of 100 Td the value of ND_L has increased to a value of 4162×10^{18} $cm^{-1} \cdot sec^{-1}$. The

measured values of ND_L are in good agreement with the values predicted by the theory of Whealton and Mason.

The longitudinal diffusion coefficients have been measured for H_3^+ ions in H_2 gas over a range of E/N from 4.5 to 85 Td. These measurements were made at gas temperature of 300°K. The values of ND_L measured in the low-field region are in excellent agreement with the value of 7.85×10^{18} $cm^{-1} \cdot sec^{-1}$ predicted by the Einstein equation. The values of ND_L rise rapidly as the E/N is increased above 10 Td. At an E/N of 85 Td the measured value of ND_L is 111×10^{18} $cm^{-1} \cdot sec^{-1}$. There is fair agreement between the measured value of ND_L and the values predicted by the Whealton-Mason equation. The differences between these values is attributed to proton exchange between H_3^+ and H_2.

The longitudinal diffusion coefficients have been measured for H^- ions in H_2 gas over a range of E/N from 2.5 to 70 Td. These measurements were made at gas pressures from 200 to 750 microns and at a gas temperature of 300°K. The agreement between the measured values of ND_L and those predicted by the Whealton-Mason equation is poor and the values of ND_L measured exhibit only the general trend of the theoretical prediction. This discrepancy is attributed to the effects of initial diffusion of the H^- ions.

Reaction Rates

The rate coefficient of the reaction between H^+ ions and H_2 gas that produces H_3^+ ions has been measured over a range of E/N from 20 to 50 Td. These measurements were made at gas pressures between 300 and 500 microns and at a gas temperature of 300°K. The reaction

frequency per ion of this reaction is proportional to the square of the gas number density. This specifies the reaction to be three-body and of the form: $H^+ + 2H_2 \rightarrow H_3^+ + H_2$. The rate coefficient is observed to be constant over the range of E/N from 20 to 50 Td with a measured value of 3.05×10^{-29} cm^6/sec.

APPENDIX I

TABULATION OF MOBILITY RESULTS

The following tables list the experimentally measured mobilities and drift velocities in order of increasing E/N. Mobility measurements are usually made at four different drift distances. The percent deviation is the standard deviation of the experimentally measured mobilities from their least squares fit. E/N is expressed in units of Townsend (Td) where 1 Td = 10^{-17} V·cm^2. The reduced mobility K_o is simply v_d/E reduced to the standard conditions of 0°C and 760 Torr. The drift velocity is expressed in units of 10^4 cm/sec and is the value of the least squares fit of the experimental points. Pressure has been corrected as explained in Chapter I and is expressed in microns (μ), where 1000 μ = 1 Torr.

Table 6. Mobility and Drift Velocity Results for H^+ Ions in Hydrogen Gas

E/N (Td)	Reduced Mobility ($cm^2/V \cdot sec$)	Standard Deviation (Percent)	Drift Velocity (10^4 cm/sec)	Pressure (Microns)
3.99	16.03	0.8	1.72	98.4
4.49	16.14	0.3	1.95	196.9
5.03	16.07	0.6	2.17	196.9
5.03	16.09	0.6	2.17	196.9
5.49	16.04	0.6	2.37	196.9
5.99	16.06	0.5	2.59	196.9
6.00	15.97	0.5	2.58	196.9
6.50	16.06	0.3	2.81	196.9
7.04	16.04	0.6	3.03	98.4
7.51	16.07	0.4	3.24	196.9
7.98	16.07	0.4	3.44	98.4
8.50	15.96	0.3	3.64	196.9
9.53	16.02	0.4	4.10	196.9
9.96	15.98	0.2	4.28	98.4
9.99	15.93	0.4	4.28	196.9
10.0	16.01	0.3	4.32	98.4
11.0	15.90	0.4	4.68	196.9
11.0	15.85	0.5	4.67	196.9
11.0	15.92	0.3	4.71	196.9
12.0	15.92	0.5	5.12	196.9
12.0	15.94	0.3	5.15	196.9
13.0	15.86	0.4	5.52	196.9
13.0	15.81	0.4	5.50	196.9
14.0	15.88	0.3	5.95	196.9
14.0	15.89	0.4	5.96	196.9
15.0	15.94	0.2	6.41	98.4
15.1	15.90	0.6	6.48	98.4
15.9	15.92	0.2	6.82	98.4
16.0	15.88	0.2	6.81	98.4
16.9	15.75	0.2	7.16	196.9
17.2	15.91	0.7	7.34	98.4
17.9	15.78	0.3	7.58	98.4
18.9	15.90	0.2	8.08	98.4
19.9	15.86	0.3	8.49	98.4
19.9	15.85	0.2	8.49	98.4
20.0	15.91	0.5	8.56	98.4

Table 6. (continued)

E/N (Td)	Reduced Mobility ($cm^2/V \cdot sec$)	Standard Deviation (Percent)	Drift Velocity (10^4 cm/sec)	Pressure (Microns)
20.9	15.85	0.2	8.92	98.4
21.9	15.78	0.3	9.29	98.4
22.9	15.78	0.3	9.72	98.4
23.9	15.82	0.4	10.17	98.4
24.9	15.71	0.3	10.50	98.4
25.0	15.70	0.6	10.54	196.9
25.1	15.85	0.6	10.68	98.4
27.0	15.61	0.4	11.33	98.4
29.9	15.45	0.4	12.40	196.9
30.1	15.49	0.7	12.52	196.9
34.9	15.36	0.3	14.40	196.9
35.2	15.37	1.1	14.55	196.9
40.0	15.27	0.3	16.39	98.4
44.8	15.05	0.3	18.13	196.9
50.0	14.98	0.3	20.12	98.4
54.8	14.66	0.1	21.57	196.9
60.1	14.62	0.3	23.60	98.4
64.8	14.36	0.4	25.00	196.9
70.1	14.35	0.2	27.04	98.4
74.6	14.12	0.8	28.31	98.4
79.9	13.91	0.3	29.86	196.9
84.9	13.78	0.2	31.43	196.9
90.0	13.53	0.9	32.73	196.9
91.0	13.97	0.3	33.14	147.6
95.0	13.53	0.1	34.54	196.9
99.6	13.35	0.3	35.73	147.6

Table 7. Mobility and Drift Velocity Results for H_3^+ Ions in Hydrogen Gas

E/N (Td)	Reduced Mobility ($cm^2/V \cdot sec$)	Standard Deviation (Percent)	Drift Velocity (10^4 cm/sec)	Pressure (Microns)
4.49	11.29	0.4	1.36	196.9
4.98	11.37	0.3	1.52	196.9
4.99	11.35	0.5	1.52	196.9
5.01	11.29	0.2	1.52	196.9
5.48	11.32	0.2	1.67	196.9
5.48	11.35	0.3	1.67	196.9
5.50	11.37	0.2	1.68	196.9
6.00	11.27	0.3	1.82	295.3
6.48	11.37	0.3	1.98	196.9
6.49	11.25	0.2	1.96	196.9
6.51	11.35	0.2	1.98	196.9
6.98	11.24	0.3	2.11	196.9
7.01	11.21	0.2	2.11	295.3
7.50	11.27	0.3	2.27	196.9
7.98	11.25	0.4	2.41	196.9
7.98	11.30	0.3	2.42	196.9
8.48	11.29	0.5	2.57	196.9
8.48	11.36	0.3	2.59	196.9
8.51	11.35	0.3	2.59	196.9
8.98	11.28	0.3	2.72	196.9
8.99	11.36	0.5	2.75	196.9
9.50	11.28	0.2	2.88	196.9
9.97	11.25	0.4	3.01	196.9
10.5	11.24	0.3	3.16	196.9
11.0	11.26	0.2	3.32	196.9
11.5	11.27	0.3	3.47	196.9
12.0	11.30	0.3	3.63	196.9
12.5	11.25	0.2	3.77	196.9
13.0	11.31	0.3	3.96	196.9
13.5	11.23	0.2	4.06	196.9
14.0	11.27	0.3	4.23	196.9
14.5	11.24	0.3	4.38	196.9
15.0	11.35	0.2	4.56	98.4
15.0	11.26	0.1	4.53	196.9
15.5	11.28	0.4	4.69	196.9
16.0	11.31	0.3	4.86	196.9

Table 7. (continued)

E/N (Td)	Reduced Mobility ($cm^2/V \cdot sec$)	Standard Deviation (Percent)	Drift Velocity (10^4 cm/sec)	Pressure (Microns)
16.5	11.29	0.3	5.00	196.9
17.0	11.25	0.3	5.13	196.9
17.5	11.27	0.4	5.30	196.9
17.9	11.21	0.1	5.40	196.9
18.5	11.25	0.3	5.60	196.9
18.9	11.14	0.2	5.67	196.9
19.0	11.33	0.2	5.77	196.9
19.5	11.24	0.2	5.88	196.9
20.0	11.41	0.3	6.12	98.4
20.0	11.32	0.4	6.08	196.9
20.0	11.27	0.3	6.06	196.9
21.0	11.17	0.3	6.29	196.9
21.0	11.26	0.1	6.35	196.9
21.0	11.28	0.3	6.37	196.9
21.9	11.15	0.1	6.56	196.9
22.0	11.26	0.1	6.65	196.9
22.0	11.24	0.2	6.64	196.9
22.9	11.22	0.2	6.91	196.9
23.0	11.28	0.2	6.97	196.9
23.0	11.26	0.3	6.96	196.9
24.0	11.34	0.6	7.29	196.9
24.0	11.25	0.2	7.25	196.9
24.0	11.29	0.1	7.28	196.9
24.9	11.29	0.2	7.55	196.9
24.9	11.35	0.1	7.59	98.4
25.0	11.37	0.7	7.65	196.9
26.0	11.25	0.3	7.84	196.9
26.9	11.23	0.4	8.11	196.9
27.0	11.24	0.3	8.16	196.9
27.9	11.33	0.2	8.49	196.9
27.9	11.12	0.3	8.35	196.9
28.0	11.29	0.4	8.48	196.9
28.9	11.24	0.2	8.73	196.9
29.8	11.26	0.2	9.03	196.9
29.9	11.29	0.3	9.08	196.9
30.0	11.42	0.3	9.20	98.4

Table 7. (continued)

E/N (Td)	Reduced Mobility ($cm^2/V \cdot sec$)	Standard Deviation (Percent)	Drift Velocity (10^4 cm/sec)	Pressure (Microns)
31.0	11.33	0.5	9.43	196.9
34.9	11.40	0.4	10.71	196.9
37.3	11.33	0.2	11.35	196.9
39.9	11.47	0.3	12.30	147.6
42.3	11.39	1.2	12.96	196.9
44.9	11.51	0.2	13.88	196.9
50.0	11.68	0.4	15.70	147.6
54.9	11.88	0.2	17.52	196.9
60.1	12.14	0.3	19.61	147.6
64.9	12.30	0.3	21.47	196.9
69.9	12.58	0.1	23.63	196.9
74.8	12.93	0.1	25.99	196.9
79.9	13.35	0.2	28.65	196.9
85.0	13.76	0.4	31.43	196.9

Table 8. Mobility and Drift Velocity Results for H^- Ions in Hydrogen Gas

E/N (Td)	Reduced Mobility ($cm^2/V \cdot sec$)	Standard Deviation (Percent)	Drift Velocity (10^4 cm/sec)	Pressure (Microns)
2.51	42.45	0.7	2.86	738.2
3.00	42.96	2.2	3.47	295.3
4.78	43.34	0.7	5.57	196.9
4.98	42.75	0.4	5.72	295.3
5.45	42.58	0.6	6.24	295.3
5.98	43.14	0.5	6.92	295.3
6.46	42.66	0.2	7.41	295.3
6.96	42.88	0.3	8.02	295.3
7.46	42.86	0.3	8.59	295.3
7.94	42.91	0.3	9.15	295.3
8.46	43.17	0.3	9.81	295.3
8.96	43.00	0.4	10.36	295.3
9.47	43.31	0.3	11.02	295.3
10.0	43.43	0.4	11.69	196.9
10.5	43.02	0.2	12.08	295.3
11.0	43.61	0.5	12.89	196.9
11.5	43.12	0.2	13.28	295.3
12.0	42.97	0.3	13.80	196.9
12.4	42.86	0.1	14.31	295.3
13.0	43.20	0.3	15.04	196.9
13.5	43.05	0.2	15.56	295.3
14.0	42.92	0.4	16.09	196.9
14.5	43.24	0.4	16.90	196.9
15.0	43.06	0.4	17.37	196.9
15.4	42.57	0.2	17.63	295.3
15.9	42.74	0.1	18.27	295.3
16.0	42.67	0.2	18.28	196.9
16.4	42.75	0.3	18.86	295.3
16.9	42.46	0.2	19.27	295.3
16.9	42.63	0.2	19.39	196.9
17.4	42.45	0.1	19.85	295.3
17.9	42.37	0.3	20.42	295.3
19.0	42.29	0.3	21.55	295.3
20.0	42.56	0.5	22.91	196.9
25.0	41.70	0.4	27.97	196.9
30.0	40.64	0.3	32.71	196.9

Table 8. (continued)

E/N (Td)	Reduced Mobility ($cm^2/V.sec$)	Standard Deviation (Percent)	Drift Velocity (10^4 cm/sec)	Pressure (Microns)
34.9	39.78	0.3	37.29	295.3
39.9	39.43	0.7	42.31	295.3
44.7	38.13	0.5	45.84	295.3
50.1	38.78	0.5	52.14	196.9
59.7	37.96	0.5	60.86	196.9
69.6	37.09	0.3	69.39	196.9

Table 9. Mobility and Drift Velocity Results for D^+ Ions in Deuterium Gas

E/N (Td)	Reduced Mobility ($cm^2/V \cdot sec$)	Standard Deviation (Percent)	Drift Velocity (10^4 cm/sec)	Pressure (Microns)
6.01	11.76	0.5	1.90	196.9
7.01	11.77	0.6	2.22	196.9
8.03	11.69	0.5	2.52	196.9
9.00	11.77	0.4	2.84	196.9
10.1	11.49	0.9	3.11	196.9
11.0	11.66	0.3	3.44	196.9
12.5	11.75	0.5	3.94	196.9
14.0	11.51	0.4	4.32	196.9
15.0	11.91	0.6	4.80	196.9
16.0	11.61	0.4	4.99	196.9
17.5	11.90	0.2	5.59	196.9
20.0	11.68	0.3	6.26	196.9
25.0	11.65	0.3	7.82	196.9
29.9	11.38	0.3	9.15	196.9
39.9	11.13	0.2	11.93	196.9
49.9	10.87	0.3	14.59	196.9

Table 10. Mobility and Drift Velocity Results for D_3^+ Ions in Deuterium Gas

E/N (Td)	Reduced Mobility ($cm^2/V \cdot sec$)	Standard Deviation (Percent)	Drift Velocity (10^4 cm/sec)	Pressure (Microns)
5.01	8.16	0.4	1.10	295.3
6.00	8.18	0.7	1.32	196.9
7.01	8.07	0.3	1.52	295.3
7.98	7.98	0.7	1.71	196.9
9.02	8.08	0.3	1.96	295.3
10.1	8.03	0.3	2.17	196.9
12.5	8.03	0.3	2.70	196.9
15.0	7.99	0.2	3.22	196.9
17.5	8.11	0.2	3.82	196.9
20.0	8.01	0.3	4.31	196.9
25.0	8.04	0.3	5.41	196.9
30.0	8.09	0.3	6.52	196.9
40.0	8.16	0.4	8.78	196.9
50.1	8.39	0.4	11.29	196.9

Table 11. Mobility and Drift Velocity Results for D^- Ions in Deuterium Gas

E/N (Td)	Reduced Mobility ($cm^2/V \cdot sec$)	Standard Deviation (Percent)	Drift Velocity (10^4 cm/sec)	Pressure (Microns)
7.47	30.2	0.5	6.08	295.3
9.97	30.0	0.3	8.02	295.3
15.0	30.1	0.3	12.08	295.3

APPENDIX II

TABULATION OF LONGITUDINAL DIFFUSION RESULTS

The following tables list the experimentally measured diffusion coefficients as a function of increasing E/N. D_L is measured at each drift distance. The Mean Deviation is the average deviation of these individual measurements from their mean value. The value of D_L actually tabulated is that measured at the longest drift distance. Theory predicts that for a specific E/N the quantity ND_L is a constant. Thus both D_L and ND_L are tabulated. The units of E/N are Townsend (Td), where 1 Td = 10^{-17} V·cm^2. The units of D_L are cm^2/sec and those of ND_L are 10^{17} cm^{-1}·sec^{-1}. Pressure is in units of microns (μ).

Table 12. Longitudinal Diffusion Results for H^+ Ions in Hydrogen Gas

E/N (Td)	ND_L (10^{17} $cm^{-1} \cdot sec^{-1}$)	Mean Deviation (Percent)	D_L (cm^2/sec)	Pressure (Microns)
3.99	106.6	2.8	3355	98.4
4.49	101.3	0.9	1596	196.9
5.03	105.1	1.0	1651	196.9
5.03	114.5	2.5	1816	196.9
5.49	102.7	1.9	1617	196.9
5.99	105.8	6.1	1667	196.9
6.00	107.3	9.6	1694	196.9
6.50	109.4	1.2	1726	196.9
7.04	113.2	2.3	3595	98.4
7.51	110.5	3.3	1746	196.9
7.98	108.0	6.3	3400	98.4
8.50	109.1	1.6	1721	196.9
9.53	113.5	1.6	1795	196.9
9.96	112.3	3.5	3533	98.4
9.99	111.6	5.6	1760	196.9
10.0	113.1	2.5	3585	98.4
11.0	116.4	1.5	1830	196.9
11.0	116.8	2.3	1838	196.9
11.0	118.2	0.4	1866	196.9
12.0	119.7	2.7	1885	196.9
12.0	121.6	1.4	1923	196.9
13.0	120.8	3.8	1898	196.9
13.0	121.8	1.8	1914	196.9
14.0	125.4	1.9	1971	196.9
14.0	118.3	1.5	1861	196.9
15.0	121.2	1.7	3815	98.4
15.1	118.4	5.0	3777	98.4
15.9	116.4	1.6	3661	98.4
16.0	119.7	2.1	3764	98.4
16.9	117.7	2.2	1849	196.9
17.2	105.7	6.9	3367	98.4
17.9	123.5	1.9	3873	98.4
18.9	129.5	1.2	4066	98.4
19.9	131.8	4.7	4140	98.4
19.9	131.3	1.5	4131	98.4
20.0	132.5	2.3	4183	98.4

Table 12. (continued)

E/N (Td)	ND_L (10^{17} $cm^{-1} \cdot sec^{-1}$)	Mean Deviation (Percent)	D_L (cm^2/sec)	Pressure (Microns)
20.9	136.7	1.3	4300	98.4
21.9	133.3	1.5	4192	98.4
22.9	137.6	0.6	4327	98.4
23.9	144.0	0.3	4533	98.4
24.9	135.0	3.7	4242	98.4
25.0	140.1	3.7	2209	196.9
25.1	142.5	4.3	4509	98.4
27.0	142.4	0.6	4468	98.4
29.9	162.8	1.3	2559	196.9
30.1	156.7	1.8	2479	196.9
34.9	176.0	3.7	2769	196.9
35.2	167.7	2.0	2664	196.9
40.0	186.6	1.5	5884	98.4
44.8	203.1	1.5	3193	196.9
50.0	237.4	1.4	7490	98.4
54.8	249.3	3.2	3916	196.9
60.1	277.4	4.7	8768	98.4
64.8	305.3	3.7	4802	196.9
70.1	320.1	2.6	10121	98.4
74.6	331.0	2.7	10395	98.4
79.9	352.9	4.6	5561	196.9
84.9	373.8	3.7	5889	196.9
90.0	352.2	5.5	5557	196.9
91.0	426.8	6.0	8987	147.6
95.0	517.1	10.4	8158	196.9
99.6	416.2	3.3	8725	147.6

Table 13. Longitudinal Diffusion Results for H_3^+ Ions in Hydrogen Gas

E/N (Td)	ND_L (10^{17} $cm^{-1} \cdot sec^{-1}$)	Mean Deviation (Percent)	D_L (cm^2/sec)	Pressure (Microns)
4.49	76.8	8.8	1209	196.9
4.98	74.8	2.0	1175	196.9
4.99	75.8	1.6	1194	196.9
5.01	79.1	0.1	1239	196.9
5.48	78.2	1.3	1229	196.9
5.48	78.3	5.5	1230	196.9
5.50	80.3	5.5	1267	196.9
6.00	77.9	2.1	819	295.3
6.48	75.9	4.8	1193	196.9
6.49	73.2	1.9	1153	196.9
6.51	73.3	1.9	1157	196.9
6.98	76.9	6.9	1210	196.9
7.01	80.2	5.6	845	295.3
7.50	76.6	1.3	1208	196.9
7.98	76.1	2.1	1199	196.9
7.98	76.6	2.3	1207	196.9
8.48	81.1	2.6	1277	196.9
8.48	76.3	1.2	1202	196.9
8.51	80.4	2.4	1270	196.9
8.98	79.4	2.0	1250	196.9
8.99	83.1	2.1	1310	196.9
9.50	77.4	1.1	1222	196.9
9.97	79.1	1.2	1245	196.9
10.5	76.7	2.7	1205	196.9
11.0	84.1	1.4	1323	196.9
11.5	79.6	0.9	1252	196.9
12.0	84.0	2.3	1322	196.9
12.5	78.1	1.3	1230	196.9
13.0	85.2	1.1	1346	196.9
13.5	81.1	2.3	1276	196.9
14.0	85.1	0.9	1342	196.9
14.5	85.6	1.7	1349	196.9
15.0	84.0	0.9	2646	98.4
15.0	87.0	0.9	1369	196.9
15.5	85.0	1.8	1340	196.9
16.0	88.0	1.9	1387	196.9

Table 13. (continued)

E/N (Td)	ND_L (10^{17} $cm^{-1} \cdot sec^{-1}$)	Mean Deviation (Percent)	D_L (cm^2/sec)	Pressure (Microns)
16.5	88.9	2.3	1400	196.9
17.0	82.1	1.2	1293	196.9
17.5	94.6	0.3	1334	196.9
17.9	91.9	1.1	1444	196.9
18.5	88.7	1.8	1400	196.9
18.9	87.1	0.8	1369	196.9
19.0	92.8	1.0	1462	196.9
19.5	89.2	0.4	1406	196.9
20.0	88.5	0.7	2787	98.4
20.0	94.0	2.7	1484	196.9
20.0	89.8	1.1	1418	196.9
21.0	91.4	0.6	1440	196.9
21.0	93.9	2.2	1479	196.9
21.0	90.7	1.7	1432	196.9
21.9	89.4	0.7	1405	196.9
22.0	93.8	0.8	1479	196.9
22.0	98.7	1.1	1556	196.9
22.9	92.5	0.8	1454	196.9
23.0	93.4	1.4	1473	196.9
23.0	98.2	1.4	1549	196.9
24.0	96.5	3.5	1519	196.9
24.0	96.2	1.2	1516	196.9
24.0	95.4	0.6	1506	196.9
24.9	100.1	1.4	1572	196.9
24.9	97.4	2.2	3059	98.4
25.0	101.5	2.1	1603	196.9
26.0	102.9	2.4	1621	196.9
26.9	114.9	3.0	1806	196.9
27.0	105.1	3.2	1661	196.9
27.9	102.6	2.3	1611	196.9
27.9	121.5	2.2	1913	196.9
28.0	121.9	4.3	1921	196.9
28.9	112.8	1.4	1775	196.9
29.8	115.7	3.9	1816	196.9
29.9	118.5	1.7	1866	196.9
30.0	110.1	1.0	3470	98.4

Table 13. (continued)

E/N (Td)	ND_L (10^{17} $cm^{-1} \cdot sec^{-1}$)	Mean Deviation (Percent)	D_L (cm^2/sec)	Pressure (Microns)
31.0	121.2	3.1	1912	196.9
34.9	127.2	3.0	2003	196.9
37.3	147.1	3.8	2309	196.9
39.9	153.5	1.1	3223	147.6
42.3	183.0	3.6	2878	196.9
44.9	183.1	1.7	2881	196.9
50.0	234.0	0.6	4923	147.6
54.9	303.7	1.4	4782	196.9
60.1	373.9	1.3	7880	147.6
64.9	489.7	3.8	7723	196.9
69.9	617.4	3.1	9731	196.9
74.8	709.5	2.7	11169	196.9
79.9	909.5	2.1	14330	196.9
85.0	1110.6	3.1	17519	196.9

Table 14. Longitudinal Diffusion Results for H^- Ions in Hydrogen Gas

E/N (Td)	ND_L (10^{17} $cm^{-1} \cdot sec^{-1}$)	Mean Deviation (Percent)	D_L (cm^2/sec)	Pressure (Microns)
2.51	318.1	7.6	1344	738.2
3.00	387.7	5.1	2692	295.3
4.78	414.2	6.8	6559	196.9
4.98	406.6	14.1	4263	295.3
5.45	399.9	6.9	4173	295.3
5.98	533.9	7.9	5601	295.3
6.46	401.5	6.9	4197	295.3
6.96	508.0	6.0	5312	295.3
7.46	433.0	8.9	4529	295.3
7.94	421.4	3.5	4403	295.3
8.46	484.2	2.9	5069	295.3
8.96	494.2	5.2	5178	295.3
9.47	537.3	4.0	5635	295.3
10.0	485.6	4.0	7676	196.9
10.5	534.3	5.2	5596	295.3
11.0	583.4	5.2	9206	196.9
11.5	568.3	4.5	5955	295.3
12.0	551.7	4.3	8672	196.9
12.4	560.8	4.1	5869	295.3
13.0	603.6	5.2	9494	196.9
13.5	632.6	9.7	6629	295.3
14.0	613.4	4.8	10474	196.9
14.5	680.3	5.9	10770	196.9
15.0	685.2	5.6	10818	196.9
15.4	751.0	6.0	7858	295.3
15.9	734.0	6.8	7681	295.3
16.0	769.7	5.3	12105	196.9
16.4	755.2	11.2	7908	295.3
16.9	796.0	7.6	8322	295.3
16.9	737.5	4.2	10591	196.9
17.4	784.9	7.3	8209	295.3
17.9	829.5	8.6	8696	295.3
19.0	949.5	6.9	9969	295.3
20.0	906.8	6.6	14335	196.9
25.0	1047.9	8.6	16517	196.9
30.0	1477.1	8.5	23280	196.9

Table 14. (continued)

E/N (Td)	ND_L (10^{17} $cm^{-1} \cdot sec^{-1}$)	Mean Deviation (Percent)	D_L (cm^2/sec)	Pressure (Microns)
34.9	3065.3	14.9	32152	295.3
39.9	4259.4	17.4	44743	295.3
44.7	7575.8	14.7	74479	295.3
50.1	6763.0	21.4	106823	196.9
59.7	5552.6	12.2	87181	196.9
69.6	6330.0	12.0	99489	196.9

Table 15. Longitudinal Diffusion Results for D^+ Ions in Deuterium Gas

E/N (Td)	ND_L (10^{17} $cm^{-1} \cdot sec^{-1}$)	Mean Deviation (Percent)	D_L (cm^2/sec)	Pressure (Microns)
6.01	70.3	6.0	1109	196.9
7.01	80.2	1.1	1267	196.9
8.03	76.2	3.3	1207	196.9
9.00	83.3	1.5	1314	196.9
10.1	77.1	5.6	1226	196.9
11.0	83.0	2.7	1310	196.9
12.5	80.7	3.8	1271	196.9
14.0	83.3	2.2	1311	196.9
15.0	90.7	0.8	1431	196.9
16.0	90.3	0.8	1425	196.9
17.5	97.1	1.6	1530	196.9
20.0	98.2	1.4	1546	196.9
25.0	112.8	2.7	1780	196.9
29.9	118.9	1.7	1872	196.9
39.9	138.2	2.2	2118	196.9
49.9	168.8	2.2	2660	196.9

Table 16. Longitudinal Diffusion Results for D_3^+ Ions in Deuterium Gas

E/N (Td)	ND_L (10^{17} $cm^{-1} \cdot sec^{-1}$)	Mean Deviation (Percent)	D_L (cm^2/sec)	Pressure (Microns)
5.01	50.7	5.3	534	295.3
6.00	57.4	2.8	905	196.9
7.01	53.0	3.3	558	295.3
7.98	50.6	1.6	797	196.9
9.02	56.7	1.6	598	295.3
10.1	57.7	3.1	916	196.9
12.5	56.3	2.2	888	196.9
15.0	61.3	1.6	968	196.9
17.5	64.6	1.3	1020	196.9
20.0	68.7	2.8	1085	196.9
25.0	81.4	2.3	1287	196.9
30.0	84.9	1.7	1339	196.9
40.0	115.8	2.5	1829	196.9
50.1	184.0	3.0	2909	196.9

Table 17. Longitudinal Diffusion Results for D^- Ions in Deuterium Gas

E/N (Td)	ND_L (10^{17} $cm^{-1} \cdot sec^{-1}$)	Mean Deviation (Percent)	D_L (cm^2/sec)	Pressure (Microns)
7.49	306.2	16.7	3213	295.3
9.97	338.9	6.8	3553	295.3
15.0	468.8	5.0	4916	295.3

APPENDIX III

TABULATION OF ION-MOLECULE REACTION RATES

The following tables list the results of the ion-molecule reaction rate determination discussed in Chapter VI. The results appear in order of increasing E/N and pressure. The Rate Coefficient is the coefficient k, in units of 10^{-29} cm^6/sec, for H^+ reacting to form H_3^+. The pressure is listed in microns and the E/N is listed in Td. The coefficient k_1 is the rate coefficient determined from the slope of the reaction produced foot, and the coefficient k_2 is the rate coefficient measured by curve fitting.

Table 18. Reaction Rate Coefficients for the Reaction $H^+ + 2H_2 \rightarrow H_3^+ + H_2$.

E/N (Td)	P (microns)	Rate Coefficients (10^{-29} cm^6/sec)	
		k_1	k_2
20	300	3.357	3.064
25	350	3.208	3.016
25	350	3.145	3.025
25	400	3.129	3.161
25	450	3.094	3.013
30	300	3.146	3.159
30	300	3.204	3.171
30	350	3.115	3.025
30	400	3.152	3.128
30	450	3.028	3.108
30	500	3.097	3.096
35	300	3.402	2.993
35	350	3.235	3.042
35	400	2.956	2.888
35	400	2.905	3.135
35	400	2.890	3.115
35	400	2.932	2.875
35	450	2.990	3.113
40	300	3.714	2.922
40	350	3.362	2.999
40	400	2.998	2.975
50	300	3.130	3.066

Table 19. Reaction Rate Coefficients for the Reaction $D^+ + 2D_2 \rightarrow D_3^+ + D_2$.

E/N (Td)	P (microns)	Rate Coefficients (10^{-29} cm^6/sec)	
		k_1	k_2
25	300	------	3.054
25	350	------	3.151
25	400	------	2.936

APPENDIX IV

DERIVATION OF MATHEMATICAL FORMULAS

This appendix contains derivations of various formulas used in the thesis. These derivations are included here instead of the main part of the text to preserve the continuity of the text and not cloud the central issue with detailed calculations. This appendix is dedicated to all those authors who have used the time honored phrase "it may easily be shown that".

A. It may easily be shown that

$$\int_0^{\omega} dy \int_0^{y} dx\, g(y-x)\, \frac{x^n}{n!} \cdot \frac{(y-x)^m}{m!} = \int_0^{\omega} du\, g(u)\, \frac{u^m}{m!} \cdot \frac{(\omega-u)^{n+1}}{(n+1)!} \qquad \text{(IV-1)}$$

where $u = y-x$.

Letting $u = y-x$, we have $du = -dx$ and the limits of integration of u go from y to zero. Therefore the lefthand side of (IV-1) is

$$\int_0^{\omega} dy \int_0^{y} dx\, g(y-x)\, \frac{x^n}{n!} \cdot \frac{(y-x)^m}{m!} = \int_0^{\omega} dy \int_0^{y} du\, g(u)\, \frac{(y-u)^n}{n!} \cdot \frac{u^m}{m!} \qquad \text{(IV-2)}$$

Now let

$$f(y) = \int_0^{y} du\, g(u)\, \frac{(y-u)^{n+1}}{(n+1)!} \cdot \frac{u^m}{m!} \qquad \text{(IV-3)}$$

Then

$$\frac{df}{dy} = f'(y) = g(y)\,\frac{(y-y)^{n+1}}{(n+1)!}\cdot\frac{y^m}{m!} - g(0)\,\frac{(y-0)^{n+1}}{(n+1)!}\cdot\frac{0^m}{m!} \qquad \text{(IV-4)}$$

$$+\int_0^y du\; g(u)\,\frac{(y-u)^n}{n!}\cdot\frac{u^m}{m!}$$

$$=\int_0^y du\; g(u)\,\frac{(y-u)^n}{n!}\cdot\frac{u^m}{m!}$$

Then

$$\int_0^\omega f'(y)\,dy = f(\omega) - f(0) = \int_0^\omega du\; g(u)\,\frac{(\omega-u)^{n+1}}{(n+1)!}\cdot\frac{u^m}{m!} \qquad \text{(IV-5)}$$

B. We want to show that

$$1 - \sum_{m=0}^{\infty}\sum_{i=0}^{m}\frac{b^m}{m!}\frac{a^i}{i!}e^{-a}e^{-b} = \sum_{m=0}^{\infty}\frac{a^{m+1}}{(m+1)!}\sum_{k=0}^{m}\frac{b^k}{k!}e^{-a}e^{-b} \qquad \text{(IV-6)}$$

Expanding the double sum on the LHS of (IV-6) we have

$$\sum_{m=0}^{\infty}\sum_{i=0}^{m}\frac{b^m}{m!}\frac{a^i}{i!} = 1 + b(1+a) + \frac{b^2}{2!}\left(1 + a + \frac{a^2}{2!}\right) \qquad \text{(IV-7)}$$

$$+\frac{b^3}{3!}\left(1 + a + \frac{a^2}{2!} + \frac{a^3}{3!}\right) + \cdots$$

$$= \left(1 + b + \frac{b^2}{2!} + \frac{b^3}{3!} + \ldots\right) + a\left(b + \frac{b^2}{2!} + \frac{b^3}{3!} + \ldots\right)$$

$$+ \frac{a^2}{2}\left(\frac{b^2}{2!} + \frac{b^3}{3!} + \frac{b^4}{4!} + \ldots\right) + \ldots$$

Adding and subtracting the same terms so to make each term in the parentheses equal yields

$$\left(1 + b + \frac{b^2}{2!} + \ldots\right) + a\left(1 + b + \frac{b^2}{2!} + \ldots\right) \qquad \text{(IV-8)}$$

$$+ \frac{a^2}{2!}\left(1 + b + \frac{b^2}{2!} + \ldots\right) + \ldots - a - \frac{a^2}{2!}\left(1 + b\right) - \frac{a^3}{3!}\left(1 + b + \frac{b^2}{2!}\right) - \ldots$$

$$= \left(1 + b + \frac{b^2}{2!} + \ldots\right)\left(1 + a + \frac{a^2}{2!} + \ldots\right) - \sum_{m=0}^{\infty} \frac{a^{m+1}}{(m+1)!} \sum_{k=0}^{m} \frac{b^k}{k!}$$

$$= e^a e^b - \sum_{m=0}^{\infty} \frac{a^{m+1}}{(m+1)!} \sum_{k=0}^{m} \frac{b^k}{k!}$$

Multiplying by $e^{-a}e^{-b}$ yields the desired result.

C. Using identity (IV-1) we want to derive equation (3-57) for n_5. In this case the time spent as ionic species B is $u = t_4 - t_3 + t_2 - t_1$.

$$n_5 = s \prod_{j=1}^{4} \left(\alpha_{j+1,j} \int_0^{t_{j+1}} dt_j \right) \exp\left[-\gamma - \frac{(z-r_d)^2}{r_L^2} \right] \qquad \text{(IV-9)}$$

$$\times \left[1 - \exp\left(- \frac{r_s^2}{r_T^2} \right) \right]$$

Here γ, r_d, r_L^2, and r_T^2 all involve $t_1 \rightarrow t_4$ only through the same linear combination involved in u. We may thus write

$$n_5 = s\, \alpha_{AB} \int_0^{t} dt_4\, \alpha_{BA} \int_0^{t_4} dt_3\, \alpha_{AB} \int_0^{t_3} dt_2\, \alpha_{BA} \int_0^{t_2} dt_1 \qquad \text{(IV-10)}$$

$$\times\, f(\lambda, t_4 - t_3 + t_2 - t_1)$$

where all extraneous dependence is absorbed in λ and f contains all the time dependence. Let $w = t_2 - t_1$, and use (IV-1) to obtain:

$$\int_0^{t_3} dt_2 \int_0^{t_2} dt_1\, f(\lambda, t_4 - t_3 + t_2 - t_1) = \int_0^{t_3} dw\; f(\lambda, t_4 - t_3 + w)\; (t_3 - w) \qquad \text{(IV-11)}$$

Now, letting $v = t_3 - w = t_3 - t_2 + t_1$ we may perform

$$\int_0^{t_4} dt_3 \int_0^{t_3} dw\, f(\lambda, t_4 - t_3 + w)\; (t_3 - w) = \int_0^{t_4} dv\, f(\lambda, t_4 - v)\; v(t_4 - v) \qquad \text{(IV-12)}$$

Now, letting $u = t_4 - v = t_4 - t_3 + t_2 - t_1$, we may perform

$$\int_0^t dt_4 \int_0^{t_4} dv\, f(\lambda, t_4 - v)\, v(t_4 - v) = \int_0^t du\, f(\lambda, u)\, u\, \frac{(t-u)^2}{2!} \qquad \text{(IV-13)}$$

$$= s\, (\alpha_{AB}\alpha_{BA})^2 \int_0^t du\, u\, \frac{(t-u)^2}{2!} \exp\left[-\gamma - \frac{(z-r_d)^2}{r_L^2}\right]$$

$$\times \left[1 - \exp\left(-\frac{r_s^2}{r_T^2}\right)\right]$$

BIBLIOGRAPHY

1. D. L. Albritton, T. M. Miller, D. W. Martin, and E. W. McDaniel, Phys. Rev. 171, 94 (1968).

2. T. M. Miller, J. T. Moseley, D. W. Martin, and E. W. McDaniel, Phys. Rev. 173, 115 (1968).

3. F. Reif, Fundamentals of Statistical and Thermal Physics (McGraw-Hill, New York, 1965), Chap. 15.

4. D. L. Albritton, D. W. Martin, E. W. McDaniel, T. M. Miller, and J. T. Moseley, Technical Report, Georgia Institute of Technology, Atlanta, Georgia (1967).

5. T. M. Miller, D. W. Martin, E. W. McDaniel, J. T. Moseley, and R. M. Snuggs, Technical Report, Georgia Institute of Technology, Atlanta, Georgia (1968).

6. R. N. Varney, Phys. Rev. Letters 5, 559 (1960).

7. G. Sinnott, Phys. Rev. 136, A370 (1964).

8. W. S. Barnes, D. W. Martin, and E. W. McDaniel, Phys. Rev. Letters 6, 110 (1961).

9. G. H. Wannier, Bell System Technical Journal 32, 170 (1953); Phys. Rev. 83, 281 (1951); 87, 795 (1952).

10. E. A. Mason and H. W. Schamp, Jr., Ann. Phys. 4, 233 (1958).

11. T. Kihara, Rev. Mod. Phys. 25, 844 (1953).

12. E. A. Mason and J. T. Vanderslice, Phys. Rev. 114, A497 (1959).

13. M. Saporoschenko, J. Chem. Phys. 42, 2760 (1965).

14. M. Saporoschenko, Phys. Rev. 139, A349 (1965).

15. I. A. Fleming, R. J. Tunnicliffe, and J. A. Rees, J. Phys. B2, 780 (1969).

16. D. L. Albritton, et al., op. cit., Chap. II, pp. 41.

17. Ibid., Appendix IV, pp. 230.

18. E. W. McDaniel and D. W. Martin, Rev. Sci. Inst. 42, 157 (Jan. 1971).

BIBLIOGRAPHY (Continued)

19. J. H. Schummers, G. M. Thomson, D. R. James, E. Graham IV, I. R. Gatland, D. W. Martin, and E. W. McDaniel, Technical Report, Georgia Institute of Technology, Atlanta, Georgia (1972), Chap. II, pp. 18.

20. I. R. Gatland, Analysis for Ion Drift Tube Experiments, to be published in Case Studies in Atomic Physics.

21. M. Abramowitz and I. A. Stegun, Handbook of Mathematical Functions, (U. S. Government Printing Office), pp. 375-376.

22. J. T. Moseley, D. W. Martin, E. W. McDaniel, R. M. Snuggs, and T. M. Miller, Technical Report, Georgia Institute of Technology, Atlanta, Georgia (1968), Chap. IV.

23. E. W. McDaniel, Collision Phenomena in Ionized Gases, (John Wiley, New York, 1964), pp. 432, 448-451.

24. G. M. Thomson, J. H. Schummers, D. R. James, E. Graham, I. R. Gatland, M. R. Flannery, and E. W. McDaniel, J. Chem. Phys. 58, 2402 (1973).

25. M. T. Elford, Aust. J. Phys. 24, 705 (1971).

26. E. W. McDaniel, Aust. J. Phys. 25, 465 (1972).

27. J. T. Moseley, et al., op. cit., Chap. IV, pp. 97.

28. J. H. Schummers, et al., op. cit., Chap III, pp. 54.

29. R. M. Snuggs, D. J. Volz, J. H. Schummers, R. D. Laser, I. R. Gatland, D. W. Martin, and E. W. McDaniel, Technical Report, Georgia Institute of Technology, Atlanta, Georgia (1970), Appendix V.

30. E. W. McDaniel and E. A. Mason, The Mobility and Diffusion of Ions in Gases (Wiley, New York, 1973), Chap. 5.

31. T. M. Miller, et al., op. cit., Chap. IV.

32. J. H. Schummers, et al., op. cit., Chap. IV.

33. A. Papoulis, The Fourier Integral and Its Application (McGraw-Hill, New York 1962), pp. 279.

34. D. L. Albritton, et al., op. cit., pp. 180.

BIBLIOGRAPHY (Concluded)

35. E. W. McDaniel, V. Čermák, A. Dalgarno, E. E. Ferguson, L. Friedman, Ion Molecule Reactions (John Wiley, New York, 1970), pp. 324.

36. E. W. Thomas, Excitation in Heavy Particle Collisions (Wiley-Interscience, New York, 1972), pp. 217.

37. K. Kawaoka and R. F. Borkman, J. Chem. Phys. 54, 4234 (1971).

38. G. J. Schulz, Rev. of Mod. Phys. 45, 378 (1973).

39. J. B. Hasted, Physics of Atomic Collisions (Butterworth, London, Second Edition, 1972), pp. 453.

40. B. Steiner, Case Studies in Atomic Collision Physics II, (North-Holland, Amsterdam, 1972).

41. D. L. Albritton, et al., op. cit., pp. 144.

42. V. I. Khvostenko and V. M. Dukel'skii, Soviet Phys. JETP 34, 1026 (1958).

43. E. E. Muschlitz, Jr., J. of App. Phys. 28, 1414 (1957).

44. H. S. Taylor, Advances in Chemical Physics Vol. 18 (Wiley-Interscience, New York, 1970), pp. 91.

45. J. H. Schummers, et al., op. cit., Appendix IV.

46. J. Kaufman, (Private Communication, 1973).

47. E. W. McDaniel, Collision Phenomena in Ionized Gases (John Wiley, New York, 1964), Chap. 9.

48. E. A. Mason and J. T. Vanderslice, J. Chem. Phys. 28, 1070 (1958).

49. J. H. Whealton and E. A. Mason (Private Communication, 1973).

50. D. L. Albritton, (Private Communication, 1973).

51. M. McFarland, D. L. Albritton, F. C. Fehsenfeld, E. E. Ferguson, and A. L. Schmeltekopf, J. Chem. Phys. 59, 6610 (1973).

52. J. H. Whealton and E. A. Mason (To be Published).

53. R. E. Robson, Aust. J. Phys. 25, 685 (1972).

VITA

Edward Graham IV was born in Lebanon, Tennessee, on 5 October 1944. He is the first of four children of Mr. and Mrs. Edward Graham, Jr. He was married to Diane Edith Booth on 4 January 1969.

Mr. Graham was graduated from Athens High School in Athens, Georgia, in 1962. He entered the Georgia Institute of Technology in that year. As an undergraduate student, he was employed part time by WAGA-TV. He received the degree of Bachelor of Science in Physics in March 1967. Through the NROTC, he was commissioned an Ensign in the United States Navy and entered active duty. He served three years on active duty aboard the U.S.S. Taussig (DD-746) stationed in San Diego, California. In December 1969, he was released from active duty to enter graduate school at the Georgia Institute of Technology. He received the degree of Master of Science in Physics in 1971. He held an NDEA Fellowship for three years.